

Abstract

BHATTACHARYA, SUPRIYO. Molecular Models for Templated Mesoporous Materials: Mimetic Simulation and Gas Adsorption. (Under the direction of Keith E. Gubbins)

The complex structures of the Templated Mesoporous Materials (TMMs) are difficult to capture using experiments. On the other hand, detailed structural information is required in order to study the confinement effects and predict material properties. We therefore present a methodology to prepare realistic molecular models of the TMMs using molecular simulations. Mimetic simulations are used to simulate the synthesis of the TMMs resulting in mesoscale models of the materials. Using this technique, we have developed models for SBA-15 and the Mesostructured Cellular Foams (MCF). The mimetic simulations also allow us to study the phase diagrams of the surfactants involved in the synthesis. We have investigated the ternary phase diagrams (surfactant-oil-water and surfactant-silica-water) of model triblock surfactants and have highlighted the effects of oil on the ordered structures. The simulation results for the effect of oil are in partial agreement with the experiments. Next, we devise a technique to convert the mesoscale TMM models into atomistic ones. The method has been demonstrated by preparing atomistic models for SBA-15. The physical properties of the models (pore size distribution, surface area, TEM and AFM images) are compared to the experimental ones. The porosities and the surface areas of the models are in quantitative agreement with those of the experimental SBA-15, whereas the pore size distribution and TEM

results agree qualitatively with the experiments. We also present new methods for characterizing model structures including a fast technique for computing pore size distributions. The results from our new technique show speed increases of several orders of magnitude compared to the existing method. Finally we simulate the adsorption of Argon inside the model SBA-15 using Grand canonical Monte Carlo simulations. The adsorption isotherm from the model is in semi-quantitative agreement with that of an experimental SBA-15. The adsorption behavior of several different pore models are investigated, which provides new light on the roles of surface roughness and micropores in determining adsorption properties. We conclude by saying that the pore models developed in this work may be used in studying phase transitions, adsorption, diffusion and reactions inside nanopores, and in preparing new mesoporous material models such as the CMK carbons.

**MOLECULAR MODELS FOR TEMPLATED MESOPOROUS
MATERIALS: MIMETIC SIMULATION AND GAS ADSORPTION**

by

SUPRIYO BHATTACHARYA

A dissertation submitted to the Graduate Faculty of
North Carolina State University
in partial fulfillment of the requirements for the
Degree of Doctor of Philosophy

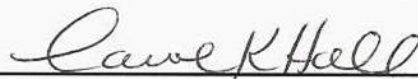
CHEMICAL ENGINEERING

Raleigh
2006

APPROVED BY:



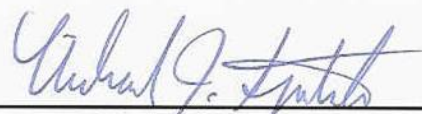
Keith E. Gubbins, Chair



Carol K. Hall



Orlin D. Velev



Richard J. Spontak

মা, বাবা ও ঠাকুমাকে

To my parents and grandmother

Biography

Supriyo Bhattacharya is originally from India. He was born on the 2nd of June, 1977 to his parents, Rina and Sanjoy Bhattacharya. After spending his boyhood in the city of Calcutta (Kolkata), he joined the Indian Institute of Technology (IIT), Kharagpur in 1996, for pursuing Bachelor of Technology (B. Tech.) in Chemical Engineering. At IIT Supriyo received the opportunity to interact with some of the leading scientific minds in India, which motivated him to undertake independent research. As part of his senior year project, he studied the effects of viscosity and diffusivity variations in laminar cross-flow ultrafiltration under the guidance of Prof. Shirshendu De and Prof. Sunando Dasgupta. After finishing his undergraduate education, Supriyo decided to pursue doctoral studies in Chemical Engineering and joined Prof. Keith Gubbins' group at NC State University in 2000. He has been engaged in developing molecular models for nanoporous materials and understanding the thermodynamics of surfactant self assembly.

Acknowledgements

During the course of my graduate studies at NC State, I have come across many kind hearted, nice people. Without their support, my work would have been incomplete. My advisor, Keith Gubbins has introduced me to the world of scientific research and supported me throughout my academic career so far. I have always relied upon him for the right amount of advice. At the same time I was allowed to think on my own and take decisions independently, which boosted my confidence level and prepared me for the next step in my career. I would like to thank the thesis committee members for taking time to review my work and provide their valuable suggestions. I am also grateful to the faculty members of the Chemical & Biomolecular Engineering Department and especially to Prof. Carol Hall and Prof. Orlin Velev for their personal advice and support.

I have had the privilege to work with a wonderful group of coworkers. Besides giving me valuable research advice, they have also been precious friends. Thanks to Flor Siperstein and Lauriane Scanu for introducing me to the topic of surfactant self assembly, and to Benoit Coasne and Francisco Hung for helping me with atomistic modeling and adsorption. Benoit and Francisco have also been my collaborators and I have learned a lot from them. I am grateful to Henry Bock for his guidance at various points in my research. His careful criticisms have helped me to improve the quality of my scientific writing. I acknowledge Naresh Chennamsetty, Erik Santiso, Surendra Jain, Joshua Moore, Milen Kostov, Coray Colina, Alberto Striolo, Jorge Pikunic, Heath Turner, Martin Lisal, and

also to Prof. Hall's group members for their support and friendship. Thanks to Sandra Bailey, Sheila Hayes, Gwen Johnson, Nora Tolar and last but not the least, June McKoy for taking care of so many things and keeping my academic life simple and stress-less. I would like to express my gratitude towards my roommates, Prashant Iyer, Dipankar Ghosh and Naresh Chennamsetty for their precious friendship and support at every step. Also thanks to Hung, Bock, Scanu, Castaño-Colina and Kostov families as well as to my old roommates and friends, Avinash, Chirag, Saurav, Sarikha and Yogitha.

This work was funded by Department of Energy (DOE) under grant no. DE-FG02-98ER14847. Supercomputing time was provided by San Diego Supercomputer Center under grant NSF/MRAC CHE050047S. CERIIUSII® software package and other computing resources were provided by Research Computing Services, UNC-Chapel Hill. Special thanks to Jorge Pikunic for helpful discussions regarding the pore size distributions and to Franz Kappel and Alexei Kuntsevich for providing the program SOLVOPT.

I am deeply endowed to my parents and grandparents for giving me relentless love and support from the very beginning. I am very grateful to my aunt in Montreal for her enduring love and care. I am also indebted to all my relatives at home and abroad for their encouragement and support.

Table of Contents

List of Tables	xii
List of Figures	xiii
Chapter 1. Introduction	1
1.1. Previous Studies in Mesoporous Materials Modeling	4
1.1.1. Surfactant Self Assembly	4
1.1.2. Modeling Nanoporous Materials	7
1.2. Overview of this Work	15
1.3. References	19
Chapter 2. Modeling Triblock Surfactant Templated Mesostructured Cellular Foams	22
2.1. Introduction	23
2.2. Simulation Method	27
2.3. Results and Discussion	31
2.3.1. Surfactant-water mixtures	31

2.3.2. Effect of head and tail lengths	33
2.3.3. Surfactant-oil-water mixtures	35
2.3.4. Surfactant-water-silica and oil mixtures	36
2.3.5. Pore size distributions	42
2.4. Conclusion	45
2.5. References	46
Chapter 3. A Realistic Molecular Model for SBA-15: Mimetic Simulations and Gas Adsorption	48
3.1. Introduction	49
3.2. Procedures	54
3.2.1. Mimetic Simulation	54
3.2.2. Atomistic Modeling	56
3.2.3. Characterization Methods	60
3.2.3.1. Pore Size Distribution	60
3.2.3.2. Pore Surface Area	61
3.2.3.3. Simulated Transmission Electron Micrograph	62
3.2.3.4. Simulated Atomic Force Micrograph	63
3.2.4. Simulation of Argon Adsorption at 77K	64
3.3. Results and Discussion	66
3.3.1. Mimetic Simulations	66

3.3.2. Characterization of model SBA-15	71
3.3.2.1. Pore Size Distribution	71
3.3.2.2. Surface Area	73
3.3.2.3. Simulated TEM	78
3.3.2.4. Simulated AFM	84
3.3.3. Simulation of Argon Adsorption at 77K	87
3.4. Conclusion	98
3.5. References	99
Chapter 4. Fast Method for Computing Pore Size Distributions of Model	102
Materials	
4.1. Introduction	103
4.2. The Problem	107
4.3. Results and Discussion	111
4.3.1. Test Model	111
4.3.2. Mimetic Models	113
4.3.3. Performance Analysis	117
4.4. Conclusion	120
4.5. References	121
Chapter 5. Conclusions and Future Directions	123

List of Tables

2.1	Intermolecular interactions used in the Lattice Monte Carlo simulations. (a) Exchange energies, (b) Interaction potentials. H: head, T: tail, O: oil, W: water, S: silica	29
2.2	Compositions of different components in the quaternary surfactant-oil-water-silica system. Letters denote the structures observed in the surfactant rich phase. C: cylindrical; L: lamellar; M: mesocellular	40
3.1	Accessible surface area of the model SBA-15 as a function of adsorbate size	75
3.2	Parameters for the model and the experimental SBA-15. Results correspond to Argon adsorption	76

List of Figures

1.1	Schematics of TMMs. (a) MCM-41. The cylinders represent the pores, (b) SBA-15. The dark curves represent the micropores within the pore walls	9
1.2	Pore morphologies studied by Coasne <i>et al</i> (a) regular cylinder; (b) cylinder with surface roughness; (c) cylinder with constrictions; (d) non-cylindrical cross-sections	13
2.1	(a) TEM of MCF. Reprinted in part with permission from Schmidt-Winkel <i>et al.</i> © 2000 American Chemical Society, (b) Graphical schematic of MCF	24
2.2	Surfactant-water binary phase diagrams. (a) H ₃ T ₅ H ₃ , (b) H ₂ T ₇ H ₂ . Symbols are used to represent the various ordered phases. Phase boundaries are marked using grey lines. (◆) spherical micelles, (■) elongated micelles, (▲) hexagonal phase, (△) perforated lamellae, (▲) lamellar phase, (■) disordered, (●) phase boundary	34
2.3	Aggregate size distributions at different surfactant concentrations	35
2.4	(a) Surfactant-oil-water phase diagram; (b) Surfactant-silica-water phase diagram; simulation points are shown as follows: (▲) spherical micelles, (▲) elongated micelles, (●) cylindrical micelles, (●) bicontinuous phase, (■) lamellar phase. Phase boundary lines are provided as a guide to the eye	37
2.5	1. Simulation : Change in pore structure with increasing oil concentration. (a) 2%, (b) 9%, (c) 23% 2. Experiment : Change in pore structure with increasing oil / surfactant mass ratios as reported by Lettow <i>et al.</i> (a) 0.00, (b) 0.21, (c) 0.50	40
2.6	1. Simulation : Pore size distributions of two different structures. (a) cylindrical, (b) mesocellular. 2. Experiment : Pore size distribution of MCF material obtained by nitrogen adsorption	43
2.7	Average pore size with oil / surfactant ratio. (a) Simulation, (b) Experiment	45

3.1	Schematics of TMMs. (a) MCM-41. The cylinders represent the pores, (b) SBA-15. The dark curves represent the micropores within the pore walls	50
3.2	Schematic of the simulation box. The color codes are the follows: Yellow-head, sea green-tail, red-oil, blue-water, green-silica	56
3.3	(a) mesoscale structure; (b) single pore with surface points shown in red; (c) pore surface modeled as b-spline with surface points shown in red	57
3.4	(a) Structure obtained by carving out the mesopores; (b) Structure after carving out the micropores; (c) The final structure after removing the unbonded atoms, saturating the dangling bonds with hydrogen and randomizing; (d) The repetitive structure obtained by replicating the unit cell. Color code: Yellow-Silicon, Red-Oxygen, Blue-Hydrogen, Violet-Pore surface	59
3.5	Definitions of molecular surface. The continuous curve represents the Connolly surface while the dotted curve represents the solvent accessible surface	62
3.6	Schematic for the simulation of AFM. The AFM probe is shown inside the pore touching the pore surface. r_p is the AFM tip radius, θ is the angle between the tip and the vertical, d is the perpendicular distance of the tip end from the pore axis	64
3.7	Aqueous phase diagram of the surfactant $H_3T_5H_3$. The symbols represent the different ordered phases and the phase boundaries are marked by the continuous curves. (◆) spherical micelles, (■) elongated micelles, (▲) hexagonal phase, (▲) lamellar phase, (■) disordered, (●) phase boundary	67
3.8	Surfactant-water-silica phase diagram at $T^*=7.0$; simulation points are shown as follows: (▲) spherical micelles, (▲) elongated micelles, (●) cylindrical micelles, (●) bicontinuous phase, (■) lamellar phase. Phase boundary lines are provided as a guide to the eye. The tie line marked in red represents the equilibrium between a surfactant rich and a water rich phase, where the surfactant rich phase forms the SBA-15 structures. The SBA-15 structures can be obtained at all points in the region marked by the red star	69
3.9	Pore size distributions; (a) Model SBA-15, (b) Experimental SBA-15	73

3.10	(a) Variation of internal surface area per unit mass with test particle radius for the model SBA-15. The significances of the three zones are marked in the figure. (b) Comparison between the surface areas per unit volume of the model SBA-15 and the model removing the micropores. ● - Model with micropores; ○ - Model without micropores; ▼ - Contribution of the micropores towards the surface area	77
3.11	Simulated TEMs of model structures. Model A represents the microporous structure and model B the non-microporous structure. (a) Axial view of model A; (b) Transverse view of model A; (c) Axial view of model B; (d) Transverse view of model B. The axial and the transverse views have been explained in the schematic. The defocus values for the individual images are tabulated	82
3.12	Effect of defocus on the image contrast in the simulated TEMs of SBA-15. The defocus values are listed below the individual images	83
3.13	Comparison between experimental and model TEMs. (a) model SBA-15 (axial direction); (b) model SBA-15 (transverse direction); (c) experimental SBA-15 (axial direction); (d) experimental SBA-15 (transverse direction); (e) model without the micropores (axial direction). The white boxes represent regions showing similar contrast patterns	83
3.14	Simulated AFMs for (a) Model A (with micropores; (b) Model B (without micropores). The x axis measures the radial inclination of the AFM tip with the vertical (degrees). The y axis measures the distance along the pore axis (nm). The z axis represents the mean deviation of the AFM tip (nm). In both figures, a positive deviation indicates a hole or a depression, while a negative deviation indicates an elevated region on the surface. The grey shades are proportional to the deviations according to the color-bars on the right	86
3.15	Cross sections of the different models used in studying adsorption. Silicon and Oxygen are represented in grey while Hydrogen is represented in black. Model A incorporates both surface roughness and micropores. Model B incorporates surface roughness without any micropores. Model C is the regular cylindrical model with the same pore diameter as models A and B	91

3.16	Adsorption isotherms for (a) Model A -○-: Adsorption, -●-: Desorption; (b) Comparison among the various pore models. -○-: Model A, -△-: Model B, -□-: Model C, -●-: Experimental SBA-15 (Galarnau <i>et al</i>). The x axis represents the relative pressure and y axis the adsorbed amount in cc/gm	91
3.17	Snapshots of simulation box with increasing pressure for model A. The values below the snapshots indicate the relative pressures. In the snapshots, grey represents silica and red argon. The low and high pressure sections of the isotherm are shown as reference. The isotherm points corresponding to the individual snapshots are circled	94
3.18	Distribution of adsorbate with pore size for (a) $P/P_0=10^{-10}$ and (b) $P/P_0=0.1$. The dark curves represent the adsorbate distribution. The PSD is shown by the histogram. The simulation box snapshots are displayed on the right	94
3.19	Adsorption isotherm for model A at low pressures showing the micropore and the mesopore contributions. The x axis is plotted in logarithmic scale.	95
3.20	Isothermic heats of adsorption for the different pore models. Figures (a), (b) and (c) represent the isothermic heats for models A, B and C respectively. Figure (d) compares the heats of adsorption from the three pore models and an experimental MCM-41 (Neimark <i>et al</i>). -○-: Model A, -△-: Model B, -□-: Model C, -●-: Experimental MCM-41. The x axis represents the relative surface loading, while the y axis represents the heat of adsorption in kJ/mole. The mean pore diameter of the models is 5.4 nm, whereas that of the experimental MCM-41 is 4.5 nm.	97
4.1	Definition of pore size used in this paper. The middle channel is the pore cavity and the grey spheres are the wall atoms. P represents the point at which the pore size is measured. D is the diameter of the circle in bold	104
4.2	Variation of computational time with grid size (on a 3 GHz Pentium IV processor)	105
4.3	Largest sphere enclosed by n atoms; r: radius of the enclosing atoms; R: radius of the largest enclosed sphere; C: center of the enclosed sphere; P: the point at which, the pore size is measured; s_i : distance from C to the center of the i^{th} atom; d_p : distance between C and P	110

4.4	Flow chart for PSD calculation	110
4.5	The test model structure. (a) Cross sectional view. Dark regions represent the void spaces and the light regions represent the pore walls; (b) Pore size distribution	112
4.6	The SBA-15 structure. (a) Simulation box snapshot; (b) Pore size distribution	114
4.7	The MCF structure. (a) Schematic of MCF pores; (b) Simulation box snapshot; (c) Pore size distribution	115
4.8	The atomistic SBA-15 structure. (a) Schematic showing the meso and the micropores; (b) Simulation box snapshot. yellow- silicon, red- oxygen, white- hydrogen; (c) Pore size distribution	116
4.9	Average error with computation time. The insets depict the evolution of the PSD over time. Each snapshot corresponds to a different time interval	118
4.10	Comparison between our method and the existing method discussed in section 1. Resolution is defined as number of points per unit length, where the pore sizes are calculated	120

Chapter 1

Introduction

The purpose of this work is to provide a comprehensive methodology for preparing realistic molecular models of templated mesoporous materials (TMM). In modeling the pores of the TMMs, simple geometrical shapes such as cylinders and spheres are unable to capture many of the important characteristics of the pore structure, for example: pore wall roughness and inter-pore connectivity. Using molecular simulations, we have mimicked the synthesis process of the TMMs, which allows us to incorporate the above mentioned characteristics in a thermodynamically consistent way in our pore models. These molecular models may be used to study confinement phenomena such as adsorption, freezing and chemical reaction rates inside nanopores and will eventually help in designing adsorbents and catalysts.

Templated mesoporous materials are synthesized by polymerizing an inorganic species (mainly silica) around ordered surfactant mesophases. A typical laboratory synthesis involves preparing an aqueous surfactant solution, where the surfactant chains self-assemble to form micelles. Then, a silica source (e.g. tetraethyl orthosilicate, TEOS) is added to the system, forming a surfactant-silica hybrid mesophase. It should be noted here that the formation of the surfactant-silica mesophase follows one of two alternative pathways depending on the surfactant concentration. In “cooperative self assembly”, the

surfactant concentration is low enough not to form any ordered phase in the absence of silica. Introduction of silica leads to a phase separation and the surfactant, silica rich phase produces the ordered mesophase. In the second route, which is also termed the “true liquid crystal templating” route, the surfactant concentration is high enough to form an ordered mesophase before the addition of silica. Once the silica is added, either the entire mesophase gets restructured, or the silica simply impregnates the micellar coronas. Finally, the solidification of silica takes place through a sol-gel reaction. The surfactants and the solvents are then removed by drying and subsequent calcination, which results in the final substance. In the above mentioned generalized synthesis recipe, different parameters may be modified in order to control the properties of the resulting material. These parameters include temperature, pH, surfactant architecture, chain length, introduction of additional solvents etc. and the material properties which may be controlled are the pore size, pore geometry and the wall thickness. Materials prepared in this way may be used in a series of industrial applications ranging from sensors, energy storage devices [1], controlled drug release [2], microcircuits [3], as photonic crystals [4] and lasers [5], and as templates to grow nanostructures such as nanowires [6] and ordered mesoporous carbons [7-9].

Most of the applications mentioned in the previous paragraph are based on the fact that the periodic arrangement of the pores and the potential energy of the pore surface are able to impart special optical and chemical properties to the mesoporous substance. Periodic variation of the refractive index in a mesoporous material leads to a photonic band gap

opening the possibility for optical semiconductors. Interactions of the pore surface with the adsorbate molecules can significantly modify the phase behavior of the adsorbate in comparison to the bulk. The same holds true for chemical reactions, where the reactant molecules being confined inside the pore may lose their rotational degrees of freedom and lead to improved reaction rates. In most cases, experiments are not sufficient to give a detailed overview of the various confinement effects that are associated with the porous substrate. Although experiments provide valuable information regarding the phase transitions, such as melting and freezing temperatures and the capillary condensation pressures, most of the experimental techniques are based on indirect evidences. Simulations, on the other hand allow direct observation of the nano-phases inside the pores and are able to provide information that are beyond the scope of experiments. However, studying the confinement phenomena using simulations necessitates realistic molecular models for the mesoporous materials. Moreover, the pore morphology in these materials is entirely dependent on the synthesis mechanism. Therefore in this work, we propose a methodology for developing molecular models for surfactant templated mesoporous materials by simulating the synthesis process. We also stress the importance of understanding the thermodynamics of surfactant self assembly in simulating the synthesis of mesoporous substances. Other alternative approaches for modeling mesoporous materials have been proposed in the literature and these will be discussed in the following section. Then we will give a brief overview of the current work.

1.1. Previous Studies in Mesoporous Materials Modeling

1.1.1. Surfactant Self Assembly

The formation of the ordered pore structure in a mesoporous material is directly related to the phenomenon of surfactant self assembly. The driving force behind surfactant self assembly is the hydrophobic effect [10], which forces the surfactant tail-groups to move away from the water molecules and assemble into clusters known as micelles. Most of the surfactant chains are large macromolecules made up of several polymer units and the timescales of micelle formation are in the range of microseconds or even milliseconds. Therefore simulating surfactant self assembly with all the atomistic details preserved is highly difficult even with the state of the art computing facilities. There have been studies in modeling micelle formation using atomistic simulations. Salaniwal *et al* [11,12] demonstrated the formation of reverse micelles in surfactant-CO₂-water systems using near-atomistic Molecular Dynamics (MD) simulations. However, the surfactant tail was modeled as a chain of spherical beads, with each bead representing either a methyl or a methylene group. Moreover, the system was studied at low surfactant concentrations, where the simulation box contained several (4-5) spherical micelles. Simulations of ordered mesophases such as cylinders and lamellae at high surfactant concentrations are beyond the reach of atomistic simulations. Therefore, the alternative approach is to coarse grain the surfactants and/or the solvents so that several monomer groups in the surfactant chain represent one unit. The potential between the coarse-grained units can be selected

in a way that the thermodynamic properties of the atomistic system are reproduced in the mesoscale system [13,14]. Similarly several solvent molecules can be combined into a single unit or completely removed from the system by incorporating their effects in the coarse-grained potential. Such coarse-grained systems can be equilibrated using methods such as Brownian Dynamics (BD) [15] and Dissipative Particle Dynamics (DPD) [16]. Using coarse-grained models, it is now possible to explore longer length and timescales in simulations, enabling the formation of spherical / elongated micelles and ordered mesophases [15,16].

One of the coarse-grained models which has been widely used in studying surfactant self assembly is the lattice model. In a lattice based system, the surfactants are modeled as chains of beads and the solvents are modeled as single beads. The model space is divided into a finite grid with each monomer unit or solvent molecule occupying one of the grid points. The system is then equilibrated using a Monte Carlo algorithm (known as Lattice Monte Carlo), where instead of the continuum, the surfactants and the solvent molecules are only allowed to move to the neighboring grid points. A computer implementation of the Lattice Monte Carlo is fast enough to reproduce complete ternary phase diagrams of polymer-solvent systems. The Lattice Monte Carlo scheme was originally proposed by Larson *et al* [17-19] for simulating self assembly in surfactant-oil-water systems. The scheme was initially developed for two dimensional systems [17] and later extended to three dimensional models [18]. In the simulation scheme proposed by Larson *et al*, several kinds of moves were designed to equilibrate the system. These included reptation

and twist for the surfactant chains and switching between the solvent units. However, the Lattice Monte Carlo scheme may be further refined by introducing the complete or partial chain regrowth using configurational bias [20-22]. In a configurationally biased move, the surfactant chain is deleted from the original location and grown in a different position in the simulation box. In partial regrowth, only a part of the chain is deleted and locally regrown while maintaining its connection with the rest of the chain. These types of moves introduce a bias in the sampling process, which needs to be corrected by introducing additional terms in the acceptance criterion. In our simulations, we have observed that, configurationally biased moves are essential for the efficient equilibration of the system.

Now we will discuss some of the studies done in aqueous surfactant systems using Lattice Monte Carlo simulations. Bernardes *et al* [23] reported the micellization of short chain surfactants in a canonical (NVT) ensemble. Mackie *et al* [24] studied the phase equilibrium in ternary surfactant-oil-water systems using interfacial NVT simulations. Comparisons were drawn among the ternary phase diagrams of several surfactants with varying chain lengths. In a related study [25], micellization of model diblock surfactants were analyzed in terms of aggregate size distributions and micellar radii of gyration. Later on, micelle formation was studied using histogram reweighted Grand Canonical Monte Carlo simulations [26], as this technique helped to distinguish between micellization and phase separation. Micellization behavior is influenced by the arrangement of hydrophilic (head-H) and hydrophobic (tail-T) units on the surfactant

chain. In spite of having the same overall chain length and identical ratios between the lengths of the head and the tail units, a diblock and a triblock surfactant can have completely different phase diagrams. The aggregation behaviors of several diblock and triblock surfactants were studied by Panagiotopoulos *et al* [27], where it was shown that the sequence of arrangement of the H and the T blocks plays a major role in determining whether a surfactant will phase separate or micellize in aqueous solution. For example, if the sequence is $H_xT_yH_x$, the surfactant will aggregate into micelles for a wider range of values of x and y compared to the sequence, $T_xH_yT_x$. Surfactant self assembly is also strongly influenced by the interaction of the solvents with the head and the tail groups. In surfactant-oil-water systems, phase separation takes place mainly due to the difference in solubility of the surfactant in the two solvents, where one of the solvents (water) is hydrophilic and the other hydrophobic (oil). Siperstein and Gubbins [28,29] showed that, phase separation is also possible when both the solvents are hydrophilic. In that case, the size of the miscibility gap is determined by the interaction between the two solvents. If both of them repel each other, the miscibility gap is wider, whereas in the other case the miscibility gap is smaller.

1.1.2. Modeling Nanoporous Materials

Depending on the modeling scheme, nanoporous materials may be classified into two broad categories. In the first case, when the detailed atomistic structure of the material is completely known from the experiments, there is almost no necessity for modeling. An

example of such material is zeolite, which is composed of silicon, aluminum and oxygen atoms bonded together in a crystalline arrangement. In other cases, the detailed atomistic structure of the material may not be available through experiments, although the gross nanometer-scale structure has been visualized using techniques such as Transmission Electron Microscopy (TEM), Scanning Electron Microscopy (SEM) and X-ray diffraction. Molecular models of such materials may be prepared using a combination of simulations, theoretical methods and information available through experimental characterization. Experiments can also provide valuable insight into the synthesis mechanism of many nanoporous substances. Therefore, simulations can be used to mimic the synthesis process [29,30], where the porous structure evolves inside the simulation box in the same way as in real experiments. However, when the synthesis mechanism is not entirely understood, reconstruction techniques [31-35] may be used to deduce the structure from experimental information. For example, activated carbon structures have been modeled using Reverse Monte Carlo, where the input information is the structure factor data from X-ray diffraction experiments [33-35].

In this review, our main focus will be on the previous modeling studies of the surfactant templated mesoporous materials. The two most common TMMs that are frequently addressed in the literature are MCM-41 [36,37] and SBA-15 [38]. Both of them are composed of hexagonally ordered cylindrical pores with amorphous siliceous pore walls. However, the pore walls of SBA-15 contain small micropores which are about an order of magnitude smaller compared to the main mesopores. In contrast, the pore walls of

MCM-41 are believed to be non-microporous. Figure 1.1 shows the schematics of both materials.

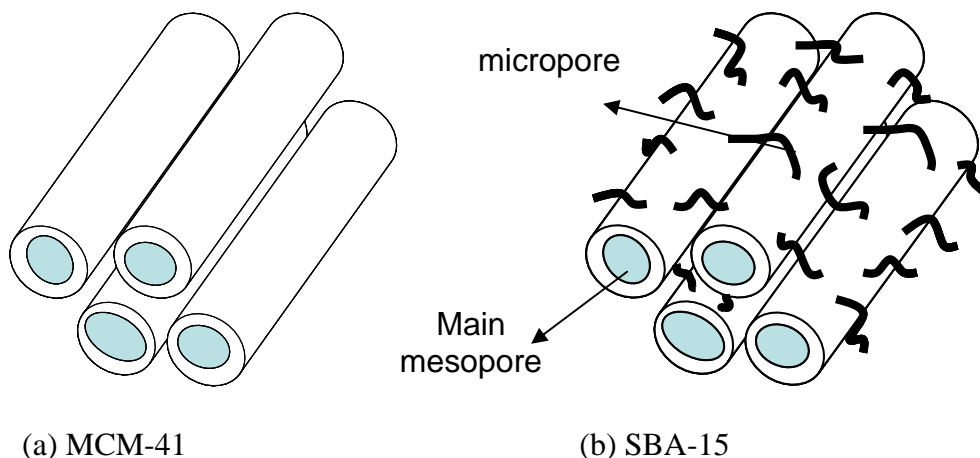


Fig. 1.1. Schematics of TMMs. (a) MCM-41. The cylinders represent the pores, (b) SBA-15. The dark curves represent the micropores within the pore walls.

Several models have been proposed in the literature in order to represent TMMs such as MCM-41 and SBA-15. In a recent study, Sonwane *et al* [39] provided an elaborate review of the various models for MCM-41. The models available in the literature may be categorized into two groups, (a) molecular models, where locations of all the atoms in the porous structure are specified, (b) potential models, where instead of atomic locations, fluid-wall potentials are specified at each location inside the simulation box. In potential models, the pore walls are represented by the regions (in the simulation box) having an infinite potential. Inside the pore cavity, the fluid-wall potential is attractive in nature with the intensity of attraction decreasing radially from the pore wall. Neimark *et al* [40-43] used potential models to study adsorption of Argon, Nitrogen and CO₂ inside

nanoporous solids. Ref. [43] reports a theoretical analysis of the adsorption of Argon and Nitrogen inside regular cylindrical nano-pores. The fluid-wall interaction was obtained from experimental adsorption on reference non-porous silica surfaces while the fluid-fluid interaction was modeled as a Lennard-jones potential. Results were compared between Non Local Density Functional Theory (NLDFT) and MC simulations. The authors reported the capillary condensation pressure as a function of pore diameter, which was found to be in quantitative agreement with the experimental results. In the above study, the pore surface was assumed to be perfectly cylindrical. However, the real experimental pore surface contains local deformations and undulations which can lead to a large deviation from the cylindrical geometry. In other words, besides the fluid-wall potential, geometrical undulations also affect the adsorption behavior, especially when the pore diameter is not very large compared to the amplitude of these undulations. In a recent study, Puibasset [44] demonstrated the effect of geometrical vs chemical heterogeneity in a cylindrical pore. Three different models were considered, (1) a regular cylindrical pore, (2) a regular cylindrical pore, where the fluid-wall potential shows local intensity variations (chemical heterogeneity), (3) a cylindrical pore with undulations in the pore wall, but with a uniform fluid-wall potential (geometrical heterogeneity). The author did not find any significant variation in adsorption properties by simply introducing geometrical undulations in the pore model. However, intensity variations in the fluid-wall potential gave rise to significant changes in the adsorption behavior. For example, the hysteresis loop in the adsorption isotherm appeared at a lower temperature in the chemically heterogeneous pore compared to the regular cylindrical model. Also,

intermediate bridge phases appeared at the onset of capillary condensation. As argued by the author, geometrical undulations lead to local variations in the fluid-wall potential, so that these two effects cannot be separated. Therefore in a real system, adsorption behavior can be strongly influenced by the geometrical undulations in the pore surface since these undulations cause distortions in the fluid-wall potential.

Besides potential models, molecular models of porous materials are widely used in the literature for studying adsorption phenomena. Molecular models may be prepared in two ways, (1) by carving out the pores in a non-porous silica matrix, (2) by growing silica walls around a predefined template. The simplest models are regular cylinders for representing cylindrical pores and regular spheres to represent spherical pores. For instance, researchers have used regular cylindrical pores for modeling MCM-41 materials [45-49] and their works have been reviewed in ref. [39]. Henceforth, attempts have been made to improve upon the smooth cylindrical models by introducing surface roughness. In a molecular pore model, surface roughness may be introduced in two different ways, (1) by randomly removing wall atoms at the pore surface creating defects and blemishes, (2) by introducing undulations in the pore walls leading to constrictions in the pore cavity. Feuston and Higgins [50] developed a molecular model for MCM-41 by introducing silicon and oxygen atoms around cylindrical templates in a way that the adjacent atoms are separated by a distance equal to the Si-O bond length. The structures were then heated to high temperatures and subsequently relaxed using MD simulations. The calculated X-ray diffraction patterns of the model structures were in agreement with

the experiments. However, no simulated adsorption data were reported for these models. Feuston and Higgins' model was further improved by Sonwane *et al* [39]. In Feuston and Higgins' model, the pore surface roughness was generated by the relaxation process, which rearranged the wall atoms and resulted in a somewhat rough surface. In Sonwane *et al*'s model, surface roughness was introduced by creating spherical voids at random locations inside the pore walls, until the skeletal silica density was equal to 2.2 gm/cc (the value reported in the literature). The diameters of these voids were selected from a Gaussian distribution. In spite of the presence of the spherical voids representing surface roughness, a snapshot of the structure resembled an array of regular cylinders, without significant surface deformations. This is probably due to the reason that the micellar template used in creating the structure was a regular cylinder. In the real world however, the micellar diameter fluctuates along the cylinder axis creating undulations on the pore surface that are not evident in Sonwane *et al*'s model.

An extensive study of the effect of pore morphology on adsorption behavior was reported by Coasne *et al* [51-53]. Several different pore models were considered, (1) a regular cylindrical pore, (2) a cylindrical pore with surface roughness, (3) a cylindrical pore with constrictions, (4) pores with non-cylindrical cross-sections, e.g. ellipse and hexagon. Fig. 1.2 summarizes the various pore geometries. It was found that the surface roughness produces attractive sites on the pore surface leading to an increase in the adsorption amount compared to the regular cylindrical model. On the other hand, constrictions in the pore cavity lead to lower capillary condensation pressures. Interestingly, a real pore from

an experimental MCM-41 material is believed to exhibit a combination of all the pore morphologies studied here. For example, surfactant chains protruding from the silica matrix lead to surface roughness, whereas fluctuations in the micellar diameter may lead to constrictions in the pore tunnel as well as non-cylindrical cross-sections.

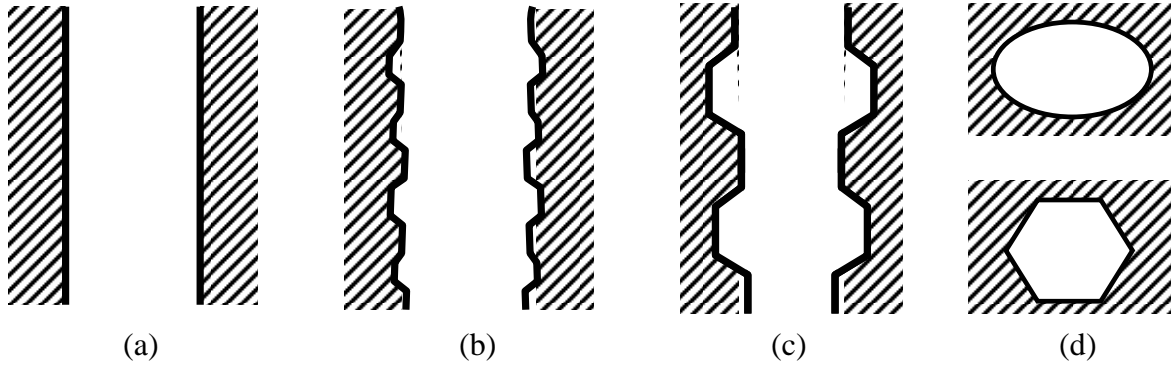


Fig. 1.2. Pore morphologies studied by Coasne *et al* (a) regular cylinder; (b) cylinder with surface roughness; (c) cylinder with constrictions; (d) non-cylindrical cross-sections

Mimetic models for MCM-41 were developed by Siperstein, Coasne and coworkers [54,55], where the surface roughness was incorporated from the mimetic simulations. First, a mesoscale model was created by mimicking the synthesis of MCM-41 using Lattice Monte Carlo simulations [29]. Next, the atomistic model was prepared by carving out of a cristobalite block the pore morphology generated by the mesoscale simulations. Then the unbonded Silicon and Oxygen atoms were removed and the remaining dangling Si-O- bonds were saturated by Hydrogen. The final pore structure was obtained by relaxing the crystalline model using MC simulations which resulted in an amorphous structure. The simulated small angle neutron scattering spectra when compared to that of

the experimental MCM-41 showed somewhat higher roughness at molecular length-scale. However, the roughness at larger length-scales was in agreement with MCM-41. The authors also reported simulation results for the adsorption of Argon, Xenon [54] and Krypton [55] inside the model pores.

Although a considerable amount of effort has been spent in developing pore models with non-microporous pore walls resembling MCM-41, relatively few studies exist which incorporate the effect of micropores in the pore model. These micropores appear in the mesoporous substances prepared using nonionic surfactants as templates. Recently, Ravikovitch and Neimark [56] have incorporated the effect of micropores in their pore model by decreasing the silica density in the pore walls, the details of which are yet to be published. Kuchta *et al* [57] reported the results for Krypton adsorption in a cylindrical pore model with microporous pore walls using GCMC simulations. In their model, the micropores were introduced by placing Krypton atoms close to the pore surface. These Kr atoms did not move during the simulations and acted as highly attractive sites for adsorption in a way similar to the real material. In this work, the effect of the micropores was interpreted to be an enhancement of the surface roughness. However, there are other kinds of micropores, for example nanochannels inside the pore walls which act as interconnections between the adjacent pores. These nanochannels may have significant effect on the adsorption behavior, an area that is yet to be explored.

1.2. Overview of this Work

In the previous section, we gave a description of the different methodologies existing in the literature for modeling the mesoporous materials. It is now time to describe our own work so that the reader can judge its importance in comparison to the other scientific studies in the related areas. This work is dedicated to the modeling of three different mesoporous materials; the Mesostructured Cellular Foams (MCF) [58], the MCM-41 [36,37] and SBA-15 [38]. Although the structures of these materials are different from one another, the basic modeling strategy remains the same; i.e. mimicking the experimental synthesis by simulating surfactant self-assembly. The procedure leads to mesoscale models which are then converted into atomistic models in order to study the various confinement phenomena such as adsorption. We also characterize the model structures and compare the results with the experiments. We will now discuss in detail the contents of each chapter and try to show the inter-relationship that exists among them.

Chapter 2 describes the modeling of the Mesostructured Cellular Foams. Due to the presence of large interconnected pores, these materials are promising candidates in the fields of catalysis and adsorption related to large macromolecules. However, the synthesis mechanism of these materials is not clearly understood. Therefore we have carried out mimetic simulations of the synthesis of MCF with two fold objectives; to understand the synthesis mechanism, and to develop a molecular model for the material. Lattice models are used to represent the simulation systems consisting of surfactants and

solvents (oil, water and silica). We have used a chain of lattice beads to model the experimental surfactant with appropriate potentials to incorporate the hydrophilic and hydrophobic properties of the individual beads. The other solvents are modeled as single lattice sites with attractive or repulsive interactions with the different parts of the surfactant chains. The system is then equilibrated at a constant temperature using Lattice Monte Carlo. The justification for using a lattice system in modeling surfactant self-assembly has been discussed in the previous sections. The current procedure allows us to explore the entire phase diagram and identify the region responsible for the formation of the MCF structures. We are also able to study the transitions between the different mesoporous structures by varying the component concentrations. The work presented in chapter 2 also forms the foundation for the subsequent chapters where we discuss the modeling of SBA-15 and MCM-41.

In chapter 3, we discuss the modeling of SBA-15 and MCM-41. MCM-41[37] was one of the first TMMs to be discovered and is widely studied in the literature for the past ten years. However the upper limit to the pore sizes of MCM-41 is only 6 nm, which makes them unsuitable for handling large molecules such as proteins and polymers. A new material called SBA-15[38] was discovered recently, which have larger pore sizes compared to MCM-41 (5-20 nm) and are relatively stable due to thicker pore walls. One interesting feature of these materials is the presence of micropores in the pore walls (pore sizes 0.5-1.5 nm), which influence the adsorption properties and may help to improve the catalytic activity. SBA-15 is synthesized using the same ingredients as MCF, but at

different component concentrations. During synthesis, the surfactant chains penetrating the silica matrix give rise to the micropores. Our modeling strategy is composed of two different steps. In the first step, a mesoscale model of the material is prepared using the same lattice system employed in modeling the MCFs. The component concentrations required to form the SBA-15 are however different from those of the MCF. Next, an atomistic model is prepared from the mesoscale model where the surface roughness and the micropores are incorporated from the mimetic lattice simulations. Coasne *et al* [55] developed models for MCM-41 in a similar way and the methodology employed here (for surface roughness) has been borrowed from their work. We have also developed a new scheme for incorporating the micropores in the atomistic model by carving out the surfactant chains in the silica walls. This is one of the first attempts in incorporating micropores in a molecular model. The resulting model resembles the real SBA-15 in many of its physical properties such as the pore size distribution and the internal surface area. We discuss the different characterization methods that can be used to study molecular models and apply them in characterizing the model SBA-15. These methods include the pore size distribution, surface area, TEM, AFM etc.

Finally, Argon adsorption is simulated inside the model SBA-15 pores using Grand Canonical Monte Carlo simulations. The aim of this work is to highlight the role of the surface roughness and micropores in determining the adsorption characteristics of a material. Three different pore models have been considered; a rough pore with micropores (model A representing SBA-15), a rough pore without micropores (model B

representing MCM-41) and a regular cylindrical pore (model C). Pore surface roughness has been studied in the past by several researchers by simulating adsorption inside artificially generated pore models. The results from our models are in agreement with their works. However, since our models are prepared using mimetic simulations, they stand out to be realistic replicas of the real materials such as MCM-41 and SBA-15. Therefore, these models can be used to study the properties of the real materials. It should be noted that, the adsorption studies by Coasne *et al* [55] is the predecessor of the current work, since many of the methodologies have been adopted from their work. We however propose an improvement over their modeling method resulting in better prediction of the experimental results.

Besides modeling the pore structures, we have also developed new characterization techniques including a fast method for computing pore size distributions (PSD) of model materials. Calculating pore size distribution is an important technique for comparing model structures with their experimental counterparts. However, high computational costs prevent efficient calculation of PSDs, particularly for the larger structures. In chapter 4, we describe a new technique for calculating the PSDs, which provide orders of magnitude reduction in computation times compared to the existing schemes. Our method is based on the theory of non-linear optimization, which allows efficient searching of the non-linear functions for extremas. The PSD calculation technique has been successfully applied in studying the pore size distributions of our model structures and saved us many hours of computation time. Finally in chapter 5, we summarize the results obtained in the

different chapters and describe some of the future works. The current work may be extended to cover some of the recent materials, such as the mesoporous carbons. We propose a possible scheme for modeling these materials starting from the existing SBA-15 model.

1.3. References

-
- [1] A. Vaseashta and D. Dimova-Malinovska, *Science and Technology of Advanced Materials* **6**, 312 (2005).
- [2] G. Cavallaro, P. Pierro, F. S. Palumbo, F. Testa, L. Pasqua and R. Aiello, *Drug Delivery* **11**, 41 (2004).
- [3] S. H. Tolbert, A. Firouzi, G. D. Stucky and B. F. Chmelka, *Science* **278**, 264 (1997); A. Mitra, T. Cao, H. Wang, Z. Wang, L. Huang, S. Li, Z. Li and Y. Yan, *Ind. Eng. Chem. Res.* **43**, 2946 (2004).
- [4] K. Yano and Y. Fukushima, *J Mat. Chem.* **13**, 2577 (2003); P. V. Braun and P. Wiltzius, *Nature (London)* **402**, 603 (1999).
- [5] G. Wirnsberger, P. Yang, B. J. Scott, B. F. Chmelka and G. D. Stucky, *Spectrochimica Acta, Part A: Molecular and Biomolecular Spectroscopy* **57A**, 2049 (2001).
- [6] A. Fukuoka, Y. Sakamoto, H. Araki, S. Inagaki, N. Sugimoto, Y. Fukushima and M. Ichikawa, *Stud. Surf. Sci. Catal.* **145**, 173 (2003).
- [7] S. Han, M. Kim and T. Hyeon, *Carbon* **41**, 1525 (2003).
- [8] Z. Li and M. Jaroniec, *J. Phys. Chem. B* **108**, 824 (2004).
- [9] R. Ryoo, S. H. Joo, M. Kruk and M. Jaroniec, *Adv. Mater.* **13**, 677 (2001).
- [10] J. Israelachvili, *Intermolecular and Surface Forces*, Academic Press 2nd edition.
- [11] S. Salaniwal, S. Cui, P. T. Cummings and H. D. Cochran, *Langmuir* **17**, 1773 (2001).
- [12] S. Salaniwal, S. Cui, P. T. Cummings and H. D. Cochran, *Langmuir* **17**, 1784 (2001).
- [13] N. Chennamsetty, H. Bock and K. E. Gubbins, *Mol. Phys.* **103**, 3185 (2005).
- [14] J. R. Silbermann, S. H. L. Klapp, M. Schoen, N. Chennamsetty, H. Bock and K. E. Gubbins, *J. Chem. Phys.* in press.
- [15] C. R. Iacovella, M. A. Horsch, Z. Zhang and S. C. Glotzer, *Langmuir* **21**, 9488 (2005).
- [16] S. Jury, P. Bladon, M. Cates, S. Krishna, M. Hagen, N. Ruddock and P. Warren, *Phys. Chem. Chem. Phys.* **1**, 2051 (1999).
- [17] R. G. Larson, L. E. Scriven and H. T. Davis, *J. Chem. Phys.* **83**, 2411 (1985).
- [18] R. G. Larson, *J. Chem. Phys.* **89**, 1642 (1988).

-
- [19] R. G. Larson, *J. Phys. II France* **6**, 1441 (1996).
- [20] D. Frenkel and B. Smit, *Understanding Molecular Simulation*, Academic Press 2nd edition (2002).
- [21] J. I. Siepmann and D. Frenkel, *Mol. Phys.* **75**, 59 (1992).
- [22] M. N. Rosenbluth and A. W. Rosenbluth, *J. Chem. Phys.* **23**, 356 (1955).
- [23] A. T. Bernardes, V. B. Henriques and P. M. Bisch, *J. Chem. Phys.* **101**, 645 (1994).
- [24] A. D. Mackie, K. Onur and A. Z. Panagiotopoulos, *J. Chem. Phys.* **104**, 3718 (1996).
- [25] A. D. Mackie, A. Z. Panagiotopoulos and I. Szleifer, *Langmuir* **13**, 5022 (1997).
- [26] M. A. Floriano, E. Caponetti and A. Z. Panagiotopoulos, *Langmuir* **15**, 3143 (1998).
- [27] A. Z. Panagiotopoulos, M. A. Floriano and S. K. Kumar, *Langmuir* **18**, 2940 (2002).
- [28] F. R. Siperstein and K. E. Gubbins, *Mol. Simul.* **27**, 339 (2001).
- [29] F. R. Siperstein and K. E. Gubbins, *Langmuir* **19**, 2049 (2003).
- [30] L. D. Gelb and K. E. Gubbins, *Langmuir* **14**, 2097 (1998).
- [31] G. C. Rutledge, *Phys. Rev. E* **63**, 021111 (2001).
- [32] F. L. Colhoun, R. C. Armstrong and G. C. Rutledge, *Macromolecules* **35**, 6032 (2002).
- [33] K. T. Thomson and K. E. Gubbins, *Langmuir* **16**, 5761 (2000).
- [34] J. Pikunic, C. Clinard, N. Cohaut, K. E. Gubbins, J.-M. Guet, R. J.-M. Pellenq, I. Rannou and J.-N. Rouzaud, *Langmuir* **19**, 8565 (2003).
- [35] S. K. Jain and K. E. Gubbins, *Langmuir* submitted.
- [36] C. T. Kresge, W. J. Roth, J. C. Vartuli, J. S. Beck and M. E. Leonowicz, *Nature* **359**, 710 (1992).
- [37] J. S. Beck, J. C. Vartuli, W. J. Roth, M. E. Leonowicz, C. T. Kresge, K. D. Schmitt, C. T.-W. Chu, D. H. Olsen, E. W. Sheppard, S. B. McCullen, J. B. Higgins, J. L. Schlenker, *J. Am. Chem. Soc.* **114**, 835 (1992).
- [38] D. Zhao, J. Feng, Q. Huo, N. Melosh, G. H. Fredrickson, B. F. Chmelka and G. D. Stucky, *Science* **279**, 548 (1998).
- [39] C. G. Sonwane, C. W. Jones and P. J. Ludovice, *J. Phys. Chem. B* **109**, ASAP (2005).
- [40] A. V. Neimark and P. I. Ravikovitch, *Langmuir* **13**, 5148 (1997).
- [41] P. I. Ravikovitch, D. Wei, W. T. Chueh, G. L. Haller and A. V. Neimark, *J. Phys. Chem. B* **101**, 3671 (1997).
- [42] P. I. Ravikovitch, A. Vishnyakov, R. Russo and A. V. Neimark, *Langmuir* **16**, 2311 (2000).
- [43] A. V. Neimark, P. I. Ravikovitch and A. Vishnyakov, *J. Phys. Condens. Matter* **15**, 347 (2003).
- [44] J. Puibasset, *J. Phys. Chem. B* **109**, 480 (2005).
- [45] Y. He and N. A. Seaton, *Langmuir* **19**, 132 (2003).
- [46] J.-H. Yun, T. Duren, F. J. Keil and N. A. Seaton, *Langmuir* **18**, 2693 (2003).
- [47] B. Kuchta, P. Llewellyn, R. Denoyel and L. Firlej, *Colloids Surf. A* **241**, 137 (2004).
- [48] D. Cao, Z. Shen, J. Chen and X. Zhang, *Microporous Mesoporous Mater.* **67**, 159 (2004).
- [49] C. G. Sonwane and S. K. Bhatia, *Chem. Eng. Sci.* **53**, 3143 (1998).

-
- [50] B. P. Feuston and J. B. Higgins, *J. Phys. Chem.* **98**, 4459 (1994).
- [51] B. Coasne, A. Grosman, C. Ortega and R. J. M. Pellenq, *Stud. Surf. Sci. Catal.* **144**, 35 (2002).
- [52] B. Coasne and R. J. M. Pellenq, *J. Chem. Phys.* **88**, 2913 (2004).
- [53] B. Coasne, K. E. Gubbins and R. J. M. Pellenq, *Part. Part. Syst. Char.* **21**, 149 (2004).
- [54] F. R. Hung, B. Coasne, K. E. Gubbins, F. R. Siperstein and M. Sliwiska-Bartkowiak, *Stud. Surf. Sci. Catal.* in press (2005).
- [55] B. Coasne, F. R. Hung, R. J. M. Pellenq, F. R. Siperstein and K. E. Gubbins, *Langmuir* in press (2005).
- [56] P. I. Ravikovitch and A. V. Neimark, *AIChE Annual Meeting*, Cincinnati, U.S.A. 2005.
- [57] B. Kuchta, L. Firlej and G. Maurin, *J. Chem. Phys.* **123**, 174711 (2005).
- [58] J. S. Lettow, Y. J. Han, P. Schmidt-Winkel, P. Yang, D. Zhao, G. D. Stucky and J. Y. Ying, *Langmuir* **16**, 8291 (2000).

Chapter 2

Modeling Triblock Surfactant Templated Mesostructured Cellular Foams

In this chapter, we describe the molecular modeling of the mesostructured cellular foams (MCF). This work presented here has been published elsewhere*. Lattice Monte Carlo simulations are used to understand the role of surfactant self assembly in the synthesis of templated mesoporous materials with ultra-large pores. Our system consists of model triblock surfactants in the presence of oil, water and inorganic oxide. Depending on the temperature and component concentrations, these systems phase separate, and the surfactant-rich phase forms structures such as cylinders, lamellae and spheres ordered in repetitive arrangements. In the absence of oil, the structures are cylindrical with diameters of 100 Å, but increasing oil concentration produces ultra-large spheres with diameters above 500 Å. Our results closely resemble the cylinder to sphere transition associated with the synthesis of the Mesostructured Cellular Foams (MCF). Pore size distributions of our model structures are qualitatively comparable with the pore size distributions of MCFs obtained from adsorption experiments. We also observe an increase in average pore size with oil concentration, which is consistent with the experimental reportings.

* S. Bhattacharya and K. E. Gubbins *J. Chem. Phys.* 123, 134907 (2005).

2.1. Introduction

Templated mesoporous materials have been reported in the literature for more than three decades and patents were filed in this area as early as 1969 [1]. In the early 1990s', different research groups independently discovered two similar structured mesoporous silicas. One was FSM-16 [2] (Folded Silica Material-16), synthesized by Yanagisawa *et al*, and the other was MCM-41 [3,4] (Mobile Crystalline Material-41), synthesized by Beck *et al*. Today, variations in methodologies and ingredients are continuously leading to the discovery of new materials. Leaving aside subtle differences, the generalized synthesis starts with the preparation of a surfactant/oil/water solution at a controlled temperature. An inorganic oxide (usually silica) source is then added to this solution, producing a surfactant-silica liquid crystal phase which serves as a template. Polymerization of silica takes place via the sol-gel process, producing a solid framework around the liquid crystals. The solution is then dried and the polymerized residues calcined to produce the final mesoporous material. The process is sensitive to parameters such as the chain architecture and length, temperature and pH of the solution, and the different component concentrations.

Here, we present a molecular simulation strategy that mimics the synthesis of mesostructured cellular foam (MCF), whose pore structure consists of large spherical cells with diameters between 100 Å and 500 Å. The cells are connected to each other via windows having a relatively smaller diameter, around 100 Å (fig. 2.1). MCFs have

exceptionally large pores compared to most other mesoporous materials, whose pore diameters are usually below 200 Å. Well defined ordered structures are obtained even at the highest pore sizes, whereas attempts to increase the pore size in MCM materials beyond a certain limit have resulted in poorly ordered or disordered materials [5]. The large pore sizes of MCFs make them suitable candidates for separation applications involving macromolecules.

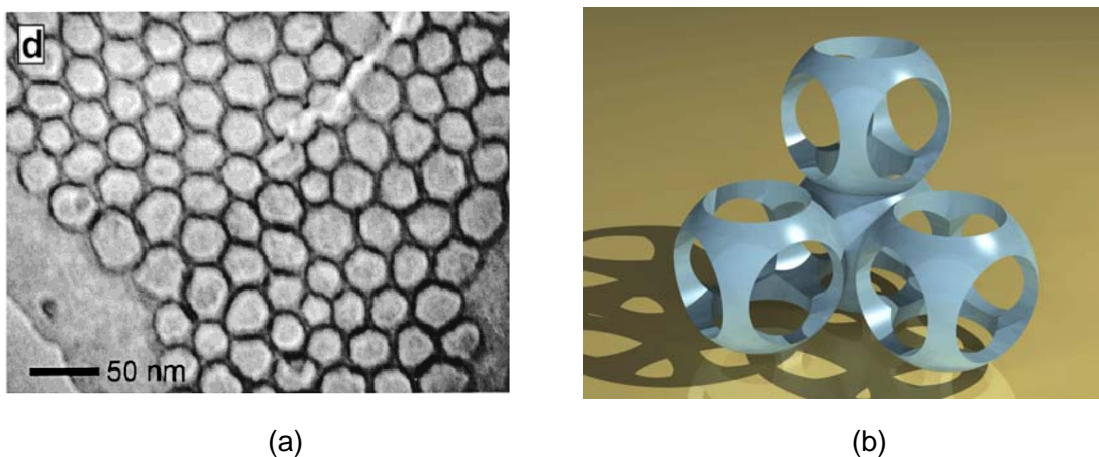


Fig. 2.1. (a) TEM of MCF. Reprinted in part with permission from Schmidt-Winkel *et al.* [7]. © 2000 American Chemical Society, (b) Graphical schematic of MCF

MCFs can be synthesized using pluronic triblock surfactants as templates, but they require the presence of a hydrophobic solvent in the surfactant solution. The detailed synthesis may be obtained from Lettow *et al* [6]. Usually, the surfactant used in the synthesis is pluronic P123, and the hydrophobic solvent is trimethyl benzene or TMB, which is frequently referred to as “oil” in the literature. Pluronics have the general formula $(\text{PEO})_x(\text{PPO})_y(\text{PEO})_x$, where PEO denotes polyethylene and PPO denotes

polypropylene. For P123, x is 20 and y is 70. In pluronic surfactants, PEO acts as the hydrophilic group and PPO acts as the hydrophobic group. In the absence of oil, the pore geometry obtained by polymerizing silica around P123 micelles is cylindrical in nature with pore diameters of around 100 Å. This cylindrical shape is maintained even when a small amount of oil is added during synthesis. The interesting transition occurs when the oil concentration is increased beyond a certain threshold. This causes the pores to become spherical, and the pore size increases rapidly as the oil concentration is increased. This transition from cylindrical SBA-15 to spherical MCF is the topic of discussion in several recent publications [6-9]. Change in pore geometry with concentration is a phenomenon known to be associated with the synthesis of mesoporous material [10]. For example, while synthesizing MCM materials, it is observed that increasing the surfactant concentration leads to the formation of lamellar instead of cylindrical pores. However, such transitions do not accompany any significant change in pore size. On the other hand, the transition from SBA-15 to MCF brought about by TMB is accompanied by a threefold increase in pore size, while maintaining a strong stability of the porous structure.

In order to understand the thermodynamic reasons that eventually lead to the ultra-large pores in MCF, we need to investigate the phenomena of surfactant self assembly. The two major opposing forces which generate the ordered structures in a surfactant solution are (1) the hydrophobic effect, that tends to bring all the surfactant tails together, and (2) the ionic / steric repulsion of the head groups, that restricts the number of chains in a

micelle to a maximum limit. In a real system, there can be numerous other factors which fine-tune the geometry of the final structure. These include the temperature, hydrogen bonding, pH and the solvent interactions. Many of these effects are not clearly understood, and including all of these in a computer simulation poses a difficult task. In the following section, we discuss the methodology we have used for modeling the self-assembling surfactant system.

Atomistic simulations (Monte Carlo and Molecular Dynamics) cannot access the large system sizes (hundreds of nanometers) needed to represent MCF and its synthesis. In this work, we employ Lattice Monte Carlo simulation methods, which enable the use of mesoscopic models of polymeric chains. Lattice Monte Carlo models have been used extensively to study the properties of surfactant solutions [11,12] and mesoporous materials synthesis [9,13,14]. Larson [15,16] was the first to use lattice models for studying surfactant self assembly. Siperstein and Gubbins [13] developed models for MCM materials that showed qualitative agreement with experimental results for heat of adsorption. In this chapter, we focus on the fundamental features of the surfactant system which we believe are responsible for the formation of the cellular cavities in MCFs; namely, the triblock architecture, relative strengths of the hydrophobic and hydrophilic potentials and component concentrations. From our simulation results using elongated boxes, we are able to construct ternary and quaternary phase diagrams of surfactant-oil-water-silica systems, and observe the formation of the different liquid crystal phases.

2.2. Simulation Method

In order to simulate the synthesis of mesoporous silicas, we modeled the surfactants and solvents as coarse-grained models, and sampled the system using Lattice Monte Carlo simulations. The simulation box consists of a cubic lattice, where one lattice unit is equivalent to 36 Å. We obtained this lattice length as follows. The fully extended chain length of a P123 molecule was estimated by optimizing the molecular geometry using the mean field approximation. The length was found to be 400 Å. This was equated to the length of a model surfactant chain, which is 11 lattice units. Therefore, one lattice unit can be calculated as $400/11 \approx 36$ Å. Comparing the surfactant chain lengths in the simulation and experimental systems is a logical way of mapping the two systems, because the diameter of a liquid crystal is mainly governed by the length of the surfactant. The solvents (water, oil) are modeled as spherical beads occupying one lattice unit each. The surfactant is modeled as a string of beads with each bead occupying one lattice unit along with an additional criterion that these beads will occupy adjacent lattice sites. In the model surfactant, several monomer units are represented by a single lattice bead. After carrying out simulations with different numbers of monomers per bead, we found that, 6.67 polyethylene units for a head bead and 14 polypropylene units for a tail bead are sufficient to give cylindrical structures in the absence of oil. This ensured that our model is realistic enough to follow the experimental trends [6]. We therefore selected our model surfactant to be $H_3T_5H_3$ (H: head, T: tail) by scaling down the surfactant P123 used in the synthesis of MCF. Interactions between the different components are modeled

as square well potentials. Two beads, i and j interact with a potential ϵ_{ij} , if they are adjacent to one another, and zero if farther away. Using the fact that the number of molecules in a NVT ensemble does not change over the course of a simulation, it can be proved that the energy change associated with any configuration rearrangement depends only on the exchange energies. An exchange energy, w_{ij} can be derived from the individual interaction potentials using the equation,

$$w_{ij} = \epsilon_{ij} - \frac{1}{2}(\epsilon_{ii} + \epsilon_{jj})$$

The derivation of this equation is given in ref. 14. We selected the exchange energies such that the surfactant head groups attract water and tail groups attract oil, analogous to the experimental situation. The silica species is designed to be more attractive towards the heads compared to water. In reality, the silica-head attraction depends on the system pH, which changes as silica polymerizes around the templates. Siperstein and Gubbins [14] studied the influence of different silica interactions on the surfactant-water-silica phase diagram. In our work, we are interested in the equilibrium properties of the surfactant-water-silica system, which do not depend on the dynamical changes the system undergoes in reaching the final state. We have therefore assumed the silica interaction to be constant throughout the simulations. The first part of Table 2.1 gives the exchange energies, which are determined based on the criteria previously discussed. On the basis of the exchange energies, we then calculate the interaction potentials given in the second part of table 2.1.

Table 2.1. Intermolecular interactions used in the Lattice Monte Carlo simulations. (a) Exchange energies, (b) Interaction potentials. H: head, T: tail, O: oil, W: water, S: silica

w_{ij}	H	T	O	W	S
H	0	1	1	0	-2
T	1	0	0	1	1
O	1	0	0	1	1
W	0	1	1	0	0
S	-2	1	1	0	0

(a)

ε_{ij}	H	T	O	W	S
H	0	0	0	0	-2
T	0	-2	-2	0	0
O	0	-2	-2	0	0
W	0	0	0	0	0
S	-2	0	0	0	0

(b)

The dimensionless temperature is defined as $T^* = k_B T / w_{HT}$, where w_{HT} is the coarse-grained interaction potential between a head and a tail bead. We selected $T^* = 7.0$, which provides an appropriate balance between the tail-tail attraction and entropic forces leading to the formation of the liquid crystal phases.

We carried out Lattice Monte Carlo simulations in an NVT ensemble, following the pathway of Larson *et al* [15]. Three different types of moves were employed, which include the reptation, twist and chain regrowth by configurational bias [17]. Similar to Kim *et al* [12], we find the configurationally biased moves essential for fast equilibration of the system. Most of these simulations were carried out in elongated boxes with one side much longer (8 times) than the other two sides. This minimizes the formation of curved interfaces, facilitating the measurement of phase properties like component

concentrations. The box sizes and simulation times depend on the length scales of the structures produced. We have carefully chosen the simulation box dimensions so that we see at least three unit cells in the final configuration. Some of the simulations were carried out in larger boxes to verify that the configurations are independent of the box sizes. For a given surfactant concentration, we carried out the simulations using two different box sizes, where the larger box was two times the length of the smaller box. In both cases, we found the same equilibrium structure with similar pore sizes irrespective of the box lengths. Cylindrical and lamellar structures required a box size of $30 \times 30 \times 240$, whereas the mesocellular structures required larger boxes, typically $60 \times 60 \times 480$, because these structures are 2-3 times larger than the cylindrical structures. The equilibration times varied also, depending on the structures and box sizes used. Smaller boxes and cylindrical structures needed 10^{10} Monte Carlo moves to equilibrate. For larger boxes and mesocellular structures, this number was about 5×10^{10} moves.

Once the system was equilibrated, we calculated the component concentrations, micellar size distribution and the pore size distribution. Phase compositions were calculated by developing concentration profiles along the longest edge of the simulation box. The phase concentrations were then obtained by averaging over the local concentrations away from the phase boundaries. Micellar size distribution was measured using the cluster labeling algorithm by Hoshen and Kopelman [18]. The pore size distribution was obtained by rolling spheres of variable sizes along the surface of the pores. The cumulative pore size distribution is obtained by plotting the diameter of the largest sphere

that can be fitted at a certain point inside the pore [19,20] against the cumulative pore volume. We then calculated the pore size distribution from the slope of the cumulative pore size distribution.

2.3. Results and Discussion

We first present the results for the simplest system, followed by the more complex ones. We start by describing the thermodynamic behavior of the surfactant $H_3T_5H_3$ dissolved in water. Then, we add oil to the system and discuss the ternary phase diagram. Finally, we study the quaternary system, comprising surfactant, oil, water and silica, where we see the appearance of the MCF structures. We conclude by analyzing the properties of the model MCF structure and comparing them with those of the experimental material.

2.3.1. Surfactant-water mixtures

The surfactant-water phase diagrams are obtained from NVT simulations carried out at different concentrations and temperatures. Fig. 2.2a represents the aqueous phase diagram of the surfactant $H_3T_5H_3$, whereas fig. 2.2b represents the phase diagram for $H_2T_7H_2$, having a different architecture. Fig. 2.2b will be discussed in the section titled “Effect of head and tail lengths”, where we compare the two phase diagrams. In Fig. 2.2a, we see the concentration and temperature dependence of the various self assembled structures starting from spherical micelles at low concentrations and evolving into

cylindrical and lamellar structures at higher concentrations. As the temperature is increased, there is a transition from ordered self-assembled structures to a completely homogeneous phase. The approximate zone of this transition is between $T^*=7.0$ and 8.0 , which is marked by the solid curves with an error bar on T^* equal to 0.5 . The features are similar to those found in the experimental phase diagrams for nonionic surfactants [21] as well as simulation results for diblock surfactants [15,13].

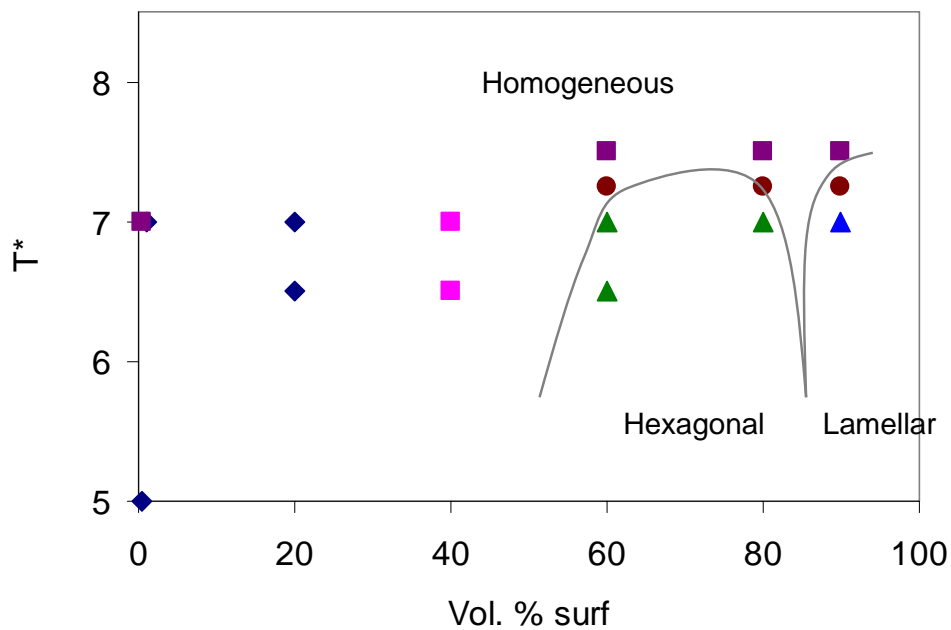
Micellization is observed at low surfactant concentrations. We can distinguish between the spherical and the elongated micelles by viewing the simulation box snapshots. Initially these micelles are spherical, but they become elongated at higher concentrations. Around 60% surfactant concentration, they transform into hexagonally ordered infinite cylinders. Fig. 2.3 shows the aggregation number distributions at different concentrations. At 5% concentration, the micelles are just starting to appear, as indicated by the plateau in the distribution curve. At 20%, the curve shows a sharp peak with the median around 25 chains. At the same time, there is an extended plateau at higher cluster sizes indicating the presence of elongated micelles. At 40% surfactant concentration, the distribution becomes wider and the plateau becomes more prominent as the micelles become increasingly ellipsoidal.

We observe the existence of hexagonally ordered cylindrical structures between 60% and 80% concentrations. Above 80%, lamellar structures are observed. Between 80% and 90% concentrations, there is likely to be a transition region where cubic structures exist.

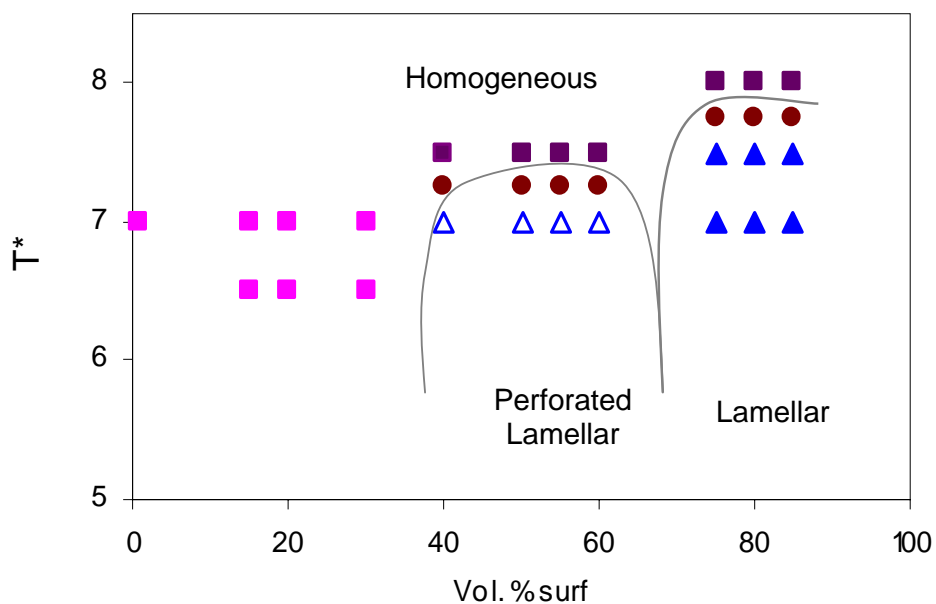
However, observing such structures requires careful selection of the box dimensions and longer simulation times.

2.3.2. Effect of head and tail lengths

In order to study the effect of surfactant architecture on self assembly, we studied the aqueous phase diagrams of two different triblock surfactants with the same overall length but different head and tail lengths (fig. 2.2). One was $H_2T_7H_2$, which has seven tail units with two head units on both sides and $H_3T_5H_3$ which has five tail units with three head units on either side. At low surfactant concentrations, both $H_2T_7H_2$ and $H_3T_5H_3$ form spherical micelles, which become ellipsoidal with increase in surfactant concentration. Both surfactants create ordered self-assembled structures at higher concentrations. While $H_2T_7H_2$ forms only lamellar structures, $H_3T_5H_3$ forms both cylindrical and lamellar structures. In the $H_2T_7H_2$ -water phase diagram, perforated lamellae are observed at medium surfactant concentrations, whereas regular lamellae are observed at high surfactant concentrations. A comparison between the structures formed by the two surfactants indicates that $H_2T_7H_2$ has more affinity towards lamellar structures compared to $H_3T_5H_3$. This is in direct agreement with the experimental data published by Wanka and Ulbricht [21], which suggests that surfactants with longer head groups favor the formation of curved interfaces, e.g. cylinders, whereas surfactants with small head groups favor structures having flat interfaces, e.g. lamellae.



(a)



(b)

Fig. 2.2. Surfactant-water binary phase diagrams. (a) H₃T₅H₃, (b) H₂T₇H₂. Symbols are used to represent the various ordered phases. Phase boundaries are marked using grey lines. (◆) spherical micelles, (■) elongated micelles, (▲) hexagonal phase, (△) perforated lamellae, (▲) lamellar phase, (■) disordered, (●) phase boundary.

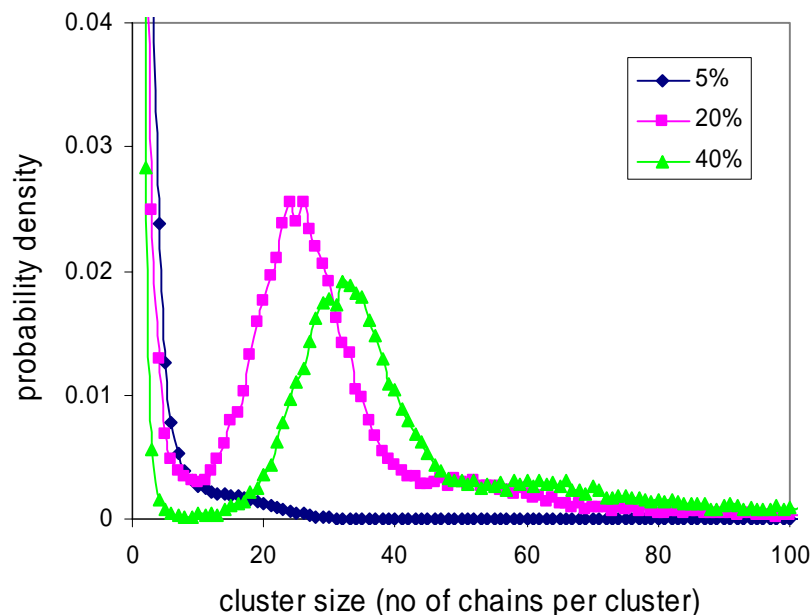


Fig. 2.3. Aggregate size distributions at different surfactant concentrations

2.3.3. Surfactant-oil-water mixtures

The ternary phase diagram for the $H_3T_5H_3$ -oil-water system is shown in fig. 2.4a. Spherical micelles are observed at low oil and surfactant concentrations. Elongated micelles and hexagonal arrangements of cylindrical micelles are observed at medium surfactant concentrations near the surfactant-water side of the phase diagram. Starting from the hexagonal phase on the surfactant-water side, as we move towards high oil concentrations, we find the emergence of a lamellar phase. In our simulations, bicontinuous structures appeared only in one point on the phase diagram, although we believe that extensive simulations should be able to find additional points. It must be noted that, the transitions between the different self-assembled structures cannot be called

true thermodynamic phase transitions because they are not first order in nature. Phase separation is observed on the surfactant-oil side between a dilute surfactant solution and a surfactant rich phase. The characteristics of the phase diagram are highly dependent on the interactions of the ‘oil’ with the other components in the system.

2.3.4. Surfactant-water-silica and oil mixtures

Silica is added to the system as a fourth component. In our simulations, silica is more attractive towards the surfactant headgroups than is water ($\epsilon_{HS}=-2$, $\epsilon_{HW}=0$). The surfactant-water-silica phase diagram is shown in fig. 2.4b. Due to the higher head-silica attraction as compared to head-water, we observe phase separation between a surfactant-rich, silica-rich phase and a water-rich phase. Ordered phases that are observed at different regions of the phase diagram depend on the component concentrations. Spherical micelles are found at low to medium surfactant concentrations, bicontinuous structures are observed at high surfactant, high silica concentrations, whereas cylindrical structures are seen at high surfactant, high water concentrations. When the number of system components increases to four, it is no longer possible to represent the phase diagram in two dimensions. A tetrahedron needs to be constructed with each corner representing one component. In this phase diagram, we limit ourselves to the region which is favorable for the formation of the mesocellular structures. We mimicked the experimental pathway [6] by starting from zero oil concentration on the surfactant-water-silica phase diagram. We selected this initial point in the region of the hexagonal phase

because experimentalists have reported the silica structure to be hexagonal in absence of oil. The oil concentration is now increased in small increments, keeping the proportion of the other components constant. The structures which we observe are depicted in fig. 2.5 along with the experimental findings.

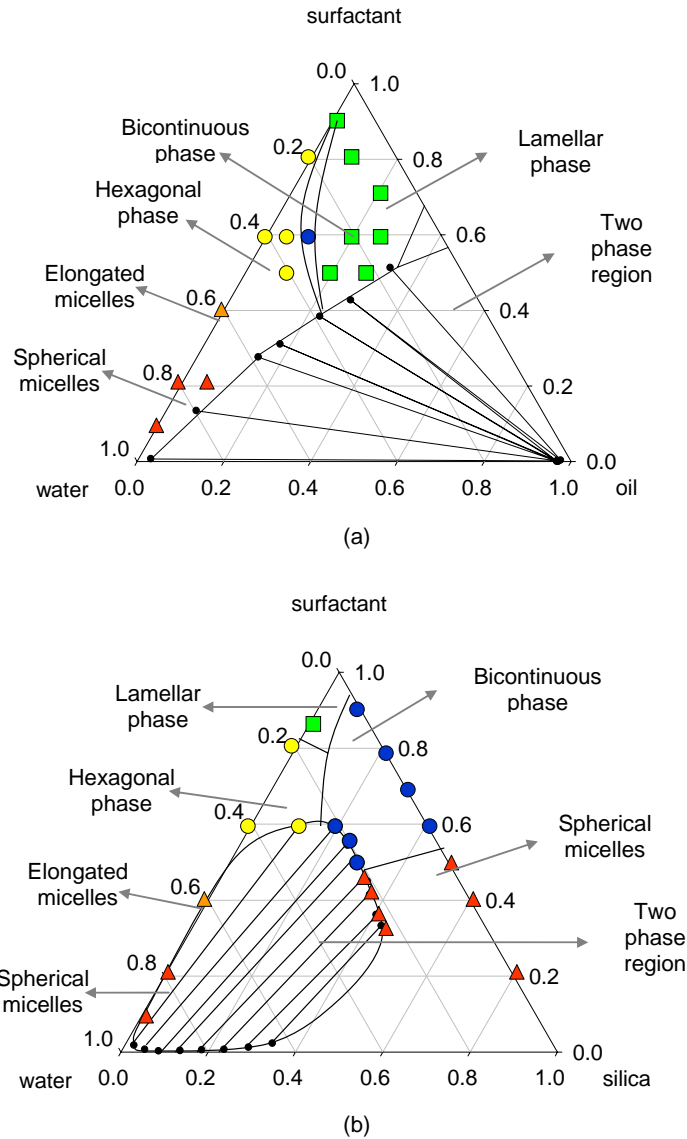


Fig. 2.4. (a) Surfactant-oil-water phase diagram; (b) Surfactant-silica-water phase diagram; simulation points are shown as follows: (\blacktriangle) spherical micelles, (\blacktriangle) elongated micelles, (\bullet) cylindrical micelles, (\bullet) bicontinuous phase, (\blacksquare) lamellar phase. Phase boundary lines are provided as a guide to the eye.

Fig. 2.5.1 shows the simulation box snapshots at different oil concentrations. Below 10% concentration, the structures are cylindrical, whereas between 10% and 16%, they are lamellar. Both the cylindrical and lamellar structures have pore sizes of the same order of magnitude. Around 16% oil concentration by volume, the structure becomes mesocellular. Fig. 2.5.1a is the view of a cross-section of the simulation box showing the pore walls of the model MCF. For better visualization, the box has been extended to include two adjacent periodic images. All three snapshots are of the same scale. The mesocellular pores are 2.5 times larger compared to the cylinders and the lamellae. Fig. 2.5.2 shows the experimental results from Lettow *et al* [6]. In both the simulations and the experiments, cylindrical structures are observed at low oil levels and these structures transform into mesocellular foams once the oil concentration is increased. However, the transition from cylinders to mesocells follows separate pathways in the simulations and the experiments. According to the experimental results reported by Lettow and coworkers, undulations occur in the walls of the cylinders prior to the transformation to MCF similar to fig. 2.5.2b. These undulations appear at medium oil concentrations, becoming more prominent as the oil concentration is increased. Finally the cylinders get pinched off at regular intervals producing isolated spheres. In the simulations, we did not observe the undulating cylinders at medium oil concentrations, but found a lamellar phase in that region. While it is difficult to explain the transition observed in the experiments, the simulation system shows predictable behavior. The geometrical shapes adopted by surfactant phases depend on the head-tail interfacial curvature and is discussed in detail by Israelachvili [22]. The cylinders are formed at low oil

concentrations, where the surfactant tails prefer to stay together, whereas the heads are solvated by water molecules. This leads to a very strong head-tail interfacial curvature leading to the formation of the cylinders. As oil is introduced into the system, the tails become solvated by the oil molecules, which increases the volume of the hydrophobic part of the micelles. This decreases the head-tail curvature favoring the formation of geometric shapes with low interfacial curvatures, such as the lamellae. The transition from the lamellae to the mesocells is however more complicated and requires further investigation. The exact mechanism for the formation of the mesocellular structures is not fully clear. Until now, what we have understood may be summarized as follows. As the amount of oil is increased in the system, due to reasons explained in the later sections, the surfactant rich phase is forced to maintain high oil concentrations. The mesocells are a result of the surfactant chains trying to shield the hydrophilic heads from being in contact with the oil molecules at such high oil concentrations. At low oil concentrations, the surfactants can orient themselves in cylindrical or lamellar structures and thus protect the heads from coming into contact with oil. In those structures, the hydrophobic parts of the micelles remain solvated by the oil molecules. However, at high oil concentrations, the amount of oil in the system exceeds the capacity of the tails to dissolve oil. Therefore, the surfactants form structures with pure oil cores surrounded by coronas of oil saturated tails, similar to the mesocells.

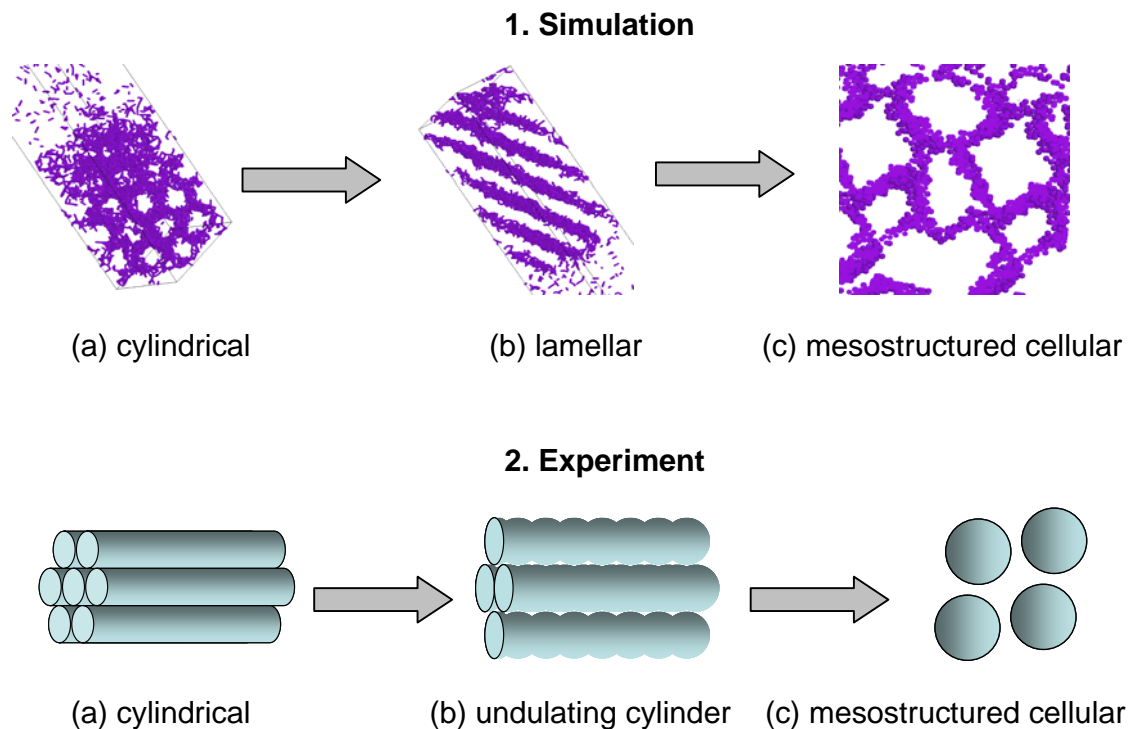


Fig. 2.5.

1. **Simulation:** Change in pore structure with increasing oil concentration. (a) 2%, (b) 9%, (c) 23%

2. **Experiment:** Change in pore structure with increasing oil / surfactant mass ratios as reported in ref. 6. (a) 0.00, (b) 0.21, (c) 0.50.

Table 2.2. Compositions of different components in the quaternary surfactant-oil-water-silica system. Letters denote the structures observed in the surfactant rich phase. C: cylindrical; L: lamellar; M: mesocellular.

Initial composition (vol %)				Phase 1 (vol %)				Phase 2 (vol %)			
surfactant	oil	water	silica	Surfactant-structure	oil	water	silica	surfactant	oil	water	silica
20.0	0.0	75.0	5.0	61.0-C	0.0	28.0	11.0	1.5	0.0	96.5	2.0
19.6	1.96	73.53	4.9	56.0-C	3.5	30.0	10.5	0.6	1.0	96.0	2.3
18.18	9.09	68.18	4.55	51.0-L	22.0	18.0	9.0	0.5	3.0	94.0	2.5
17.39	13.04	65.22	4.35	43.0-L	28.0	20.0	9.0	0.5	2.8	94.2	2.5
16.67	16.67	62.5	4.17	40.0-M	33.0	20.0	7.0	0.5	3.0	94.3	2.2
15.38	23.08	57.69	3.85	34.0-M	43.0	17.0	6.0	0.6	3.2	94.0	2.2

In order to understand the formation of the self-assembled structures in the presence of oil, we need to examine the compositions of each phase in the two phase separated quaternary system. Table 2.2 lists the phase compositions along with the starting concentrations. Phase 1 denotes the surfactant-oil-rich phase and phase 2 denotes the water-rich phase. When both silica and oil are present in the system, we observe phase separation between a surfactant-rich phase and a water-rich phase. However, in the absence of silica, phase separation leads to an oil-rich phase instead of the water-rich phase. If we compare the above two situations, we notice the difference in behavior that is brought about by the introduction of silica into the system. In the surfactant-oil-water system, the surfactant is clearly water soluble, but when silica is added, the surfactant phase becomes oil soluble. Even a very small amount of silica (less than 5% by volume) is able to increase the oil solubility of the surfactant to significant levels. Interestingly, the mesocellular structures are a result of the high oil concentration in the surfactant-rich phase. An important question arises here. Why is the mesocellular phase not observed in the surfactant-oil-water system? The answer is that, in the absence of silica, the surfactant phase is unable to maintain the high oil concentrations necessary for the formation of the mesocells. In the surfactant-oil-water phase diagram, increasing the amount of oil leads to a transition from the hexagonal phase to the lamellar phase. Any further increase in oil concentration leads to a phase separation and the additional oil goes to the dilute phase. Now, consider the four component system. Silica helps to maintain high oil levels in the surfactant phase. At a very high oil concentration, the lamellar phase becomes unstable because the amount of oil exceeds the saturation point of the tails. At this stage, the

system is expected to form reverse micelles in oil with heads inwards and tails outwards. However, in this arrangement, the head segments of surfactants in adjacent micelles are free to overlap, thus decreasing the translational entropy of the system. As a result, the reverse micellar configuration is energetically less favorable compared to the mesocellular phase. This also suggests that it may not be possible to synthesize MCFs using diblock surfactants. For the diblock surfactants, the entropic constraint for the reverse micellar phase does not exist. Therefore, at high oil concentrations, diblock surfactants are able to form reverse micelles instead of the mesocellular phase.

2.3.5. Pore size distributions

In order to determine how realistic our model is, we compare the pore size distributions (PSD) of the model structures with those of the real materials. In fig. 2.6.1, we present the PSDs of two different structures: (a) the cylindrical structure produced at an oil concentration of 2% by volume, and (b) mesocellular structures produced at an oil concentration of 23% by volume. The cylindrical structures have a pore diameter of about 200 Å, while the mesocells have a pore diameter of 700 Å. Figure 2.6.1b shows the PSD for the MCF. Due to the presence of the smaller windows and the relatively larger cell cavities, we find two distinct peaks in the pore size distribution. The one at 300 Å corresponds to the window diameter, whereas the one at 700 Å represents the cell diameter. Fig. 2.6.2 is the pore size distribution of an experimental MCF structure obtained from the literature [7]. The experimental structure also shows two peaks, one at

194 Å and the other at 410 Å. On analyzing the pore size distributions (PSD) of the model silica structures, we find qualitative agreement with the experimental results. Both the model and the real MCF structures show bimodal pore size distributions with sharp peaks. In the model PSD, the peaks are wider than those from the experiment. Also, besides the two larger peaks, the model PSDs show small peaks all over the distribution. These peaks arise because, in a lattice model, the silica particles are allowed to occupy only discrete positions in space.

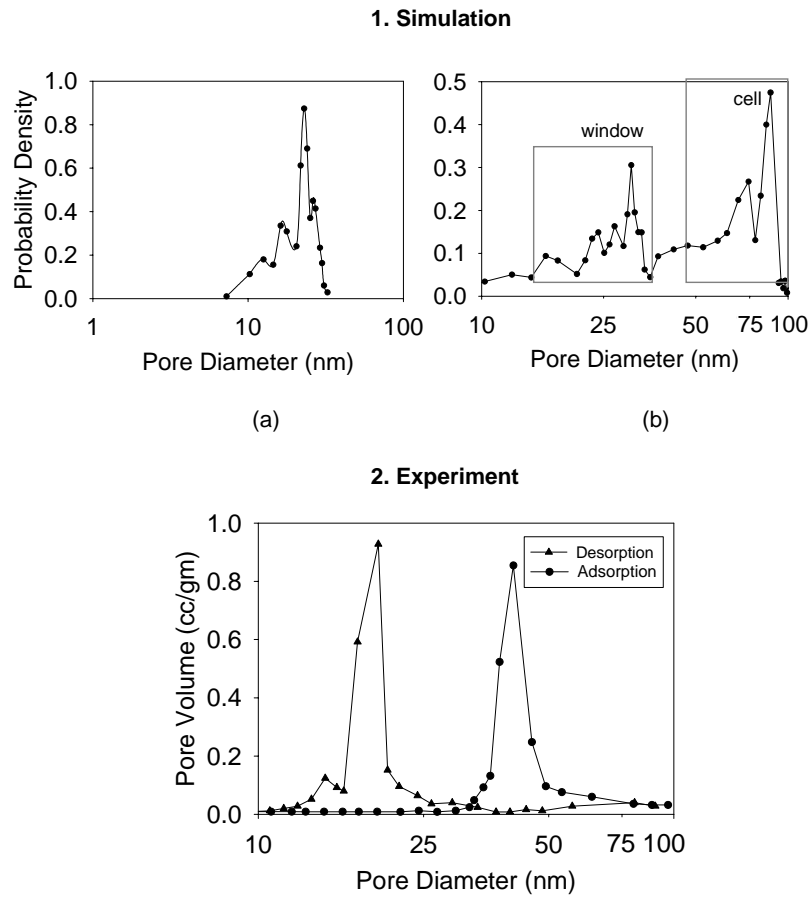


Fig. 2.6.

1. **Simulation:** Pore size distributions of two different structures. (a) cylindrical, (b) mesocellular.

2. **Experiment** [7]: Pore size distribution of MCF material obtained by nitrogen adsorption.

In fig. 2.7 we show how the average pore size changes with oil concentration, both in the simulations and in the experiment. In both situations, the pore size increases monotonically as the oil concentration is increased. Fig 2.7a represents the simulation results. At low oil/polymer ratios, we observe cylindrical pores with diameters 200-250 Å. The pore size increases to 300 Å as we move to the lamellar region. Finally, in the mesocellular region, we find very large pores with diameters around 400-700 Å. Comparing with the experimental results (fig. 2.7b), cylindrical pores have diameters between 75-100 Å. In the transition region, the pores have a diameter around 250 Å, whereas the MCF structures have diameters between 250-350 Å. We find the pore sizes in the simulations to be over-predicted compared to the experiments. This can be due to inaccuracies in mapping the lattice parameters with the experimental dimensions. However, the relative increase in pore diameter from cylinders to mesocells is the same in both simulation and experiment. In simulation, the average mesocell diameter is 650 Å, which is 2.6 times that of the cylinders (250 Å). In experiment, the average mesocell diameter is 300 Å, which is 3 times that of the cylinders (100 Å).

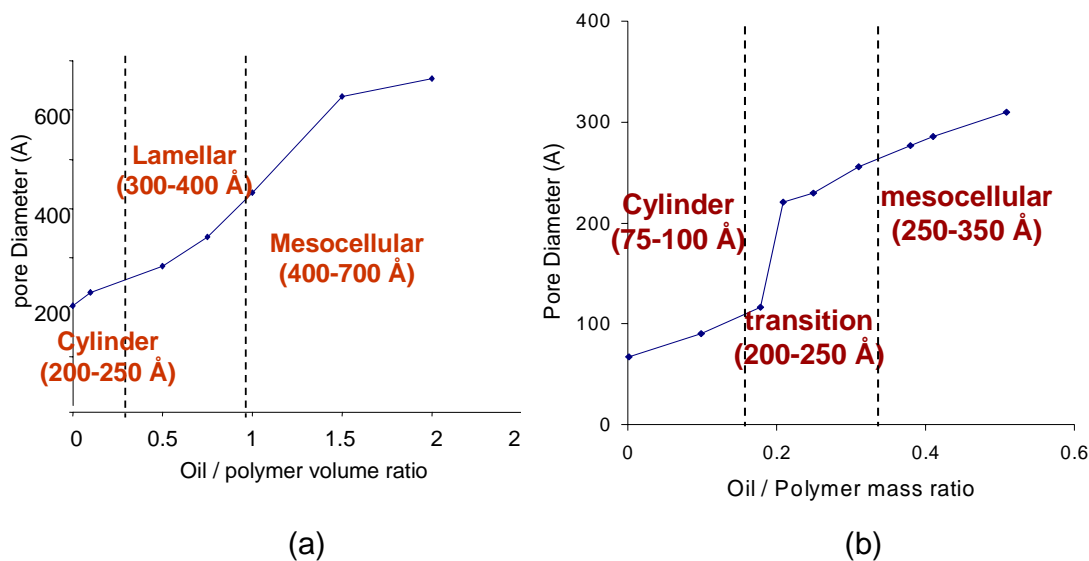


Fig. 2.7. Average pore size with oil / surfactant ratio. (a) Simulation, (b) Experiment⁶

2.4. Conclusion

We have developed a molecular model for the synthesis of mesoporous silicas and specifically for the mesostructured cellular foams. Our model is based on fundamental aspects of statistical thermodynamics, and is free from any prior assumption. Using Lattice Monte Carlo simulations, we are able to elucidate the basic features of the surfactant-oil-water-silica systems without the need of rigorous atomistic simulations. We find that adding a strongly hydrophilic substance such as silica to the surfactant-oil-water system can significantly enhance the oil solubility of the surfactant. The MCF model obtained through lattice simulations shows qualitative agreement with the experimental results, and reproduces the following aspects: (1) pore diameter increases with increasing oil concentration, (2) the statistical distribution of the pore sizes. Correct statistical pore

size distributions are difficult to obtain using geometric mean-field models, which are at the same time essential for obtaining characteristics such as adsorption and other physico-chemical characteristics of the pore system. In future, we plan to explore the entire quaternary phase diagram to locate the exact region of formation of the various silica structures, and to throw more light on the synthesis mechanism of the MCF materials.

2.5. References

-
- [1] V. Chiola, J. E. Ritsko and C. D. Vanderpool, *US Patent* **3**, 556, 725 (1971).
[2] T. Yanagisawa, T. Shimizu, K. Kuroda and C. Kato, *Bull. Chem. Soc. Jpn.* **62**, 1535 (1990).
[3] C. T. Kresge, M. E. Leonowicz, W. J. Roth, J. C. Vartuli and J. S. Beck, *Nature* **359**, 710 (1992).
[4] J. S. Beck, J. C. Vartuli, W. J. Roth, M. E. Leonowicz, C. T. Kresge, K. D. Schmitt, C.T-W. Chu, D. H. Olson, E. W. Sheppard, S. B. McCullen, J. B. Higgins and J. L. Schlenker, *J. Am. Chem. Soc.* **114**, 10834 (1992).
[5] Q. Huo, D. I. Margolese and G. D. Stucky, *Chem. Mater.* **8**, 1147 (1996).
[6] J. S. Lettow, Y. J. Han, P. Schmidt-Winkel, P. Yang, D. Zhao, G. D. Stucky G. D. and J. Y. Ying, *Langmuir* **16**, 8291 (2000).
[7] P. Schmidt-Winkel, W. W. Lukens Jr, P. Yang, D. I. Margolese, J. S. Lettow, J. Y. Ying and G. D. Stucky, *Chem. Mater.* **12**, 686 (2000).
[8] P. Schimdt-Winkel, W. W. Lukens Jr, D. Zhao, P. Yang, B. F. Chmelka and G. D. Stucky, *J. Am. Chem. Soc.* **121**, 254 (1999).
[9] S. Bhattacharya and K. E. Gubbins, *Stud. Surf. Sci. Catal.* in press.
[10] D. Zhao, Q. Huo, J. Feng, B. F. Chmelka and G. D. Stucky, *J. Am. Chem. Soc.* **120**, 6024 (1998).
[11] A. Z. Panagiotopoulos, M. A. Floriano and S. K. Kumar, *Langmuir* **18**, 2940 (2002).
[12] S. Y. Kim, A. Z. Panagiotopoulos and M. A. Floriano, *Mol. Phys.* **100**, 14 (2002).
[13] F. R. Siperstein and K. E. Gubbins, *Mol. Simul.* **27**, 339 (2001).
[14] F. R. Siperstein and K. E. Gubbins, *Langmuir* **19**, 2049 (2003).
[15] R. G. Larson, L. E. Scriven and H. T. Davis, *J. Chem. Phys.* **83**, 2411 (1985).
[16] R. G. Larson, *J. Phys. II France* **6**, 1441 (1996).
[17] D. Frenkel and B. Smit, *Understanding Molecular Simulation*, Academic Press 2nd edition, (2002).
[18] J. Hoshen and R. Kopelman, *Phys. Rev. B* **14**, 3438 (1976).
[19] L. D. Gelb and K. E. Gubbins, *Langmuir* **14**, 2097 (1998).
[20] L. D. Gelb and K. E. Gubbins, *Langmuir* **15**, 305 (1999).

-
- [21] G. Wanka and W. Ulbricht, *Macromolecules* **27**, 4145 (1994).
[22] J. Israelachvili, *Intermolecular and Surface Forces*, Academic Press 2nd edition.

Chapter 3

A Realistic Molecular Model for SBA-15: Mimetic Simulations and Gas Adsorption

We have developed a molecular model for the SBA-15 mesoporous silica. The structure of SBA-15 consists of large cylindrical mesopores with relatively smaller micropores in the pore walls. We have modeled this structure using a combination of molecular simulations and geometrical interpolation techniques. First, a mesoscale model is prepared by mimicking the synthesis process using Lattice Monte Carlo simulations. Next, the mesoscale model is converted into an atomistic model via geometrical interpolation. In the atomistic model, both the mesopores and the micropores are incorporated from the mimetic simulations. We then characterize the model structure by calculating the pore size distribution, surface area and simulated TEM and AFM images and compare these results to the experiments. Finally, Argon adsorption is simulated inside the model pores using Grand Canonical Monte Carlo (GCMC) simulations. The simulated isotherm is in quantitative agreement with the experimental isotherm from a similar pore size SBA-15. We also discuss the effect of the micropores on the adsorption characteristics by comparing the simulation results from models with and without the

micropores. The work presented in this chapter has been done in collaboration with Benoit Coasne¹ and Francisco Hung².

3.1. Introduction

Templated Mesoporous Materials (TMM) were first reported in 1969 [1], and later became the focus of much attention in the 1990s, following the synthesis of FSM-16 [2] and MCM-41 [3,4]. The applications of these materials range from catalysis [5] and adsorption [6] to sensors [7], drug delivery devices [8], low k dielectric materials, photonic crystals [9] and templates for mesoporous carbon [10]. TMMs are synthesized by polymerizing silica around ordered surfactant micelles (templates) and then removing the templates. The details of the synthesis procedure have been discussed elsewhere [11-13].

In 1998, a new kind of mesoporous material was synthesized by the researchers from UC Santa Barbara [14]. The material was SBA-15. Similar to MCM-41, SBA-15 contains hexagonally arranged cylindrical mesopores. However these mesopores are much larger than those of MCM-41, with sizes ranging between 4 and 12 nm. Also SBA-15 offers better hydrothermal stability compared to MCM-41, as a result of increased pore wall thickness. Another interesting aspect of the SBA-15 structure is the presence of

¹ Laboratoire de Physicochimie de la Matière Condensée (UMR CNRS 5617), Université de Montpellier II, Montpellier, France.

² University of Wisconsin-Madison, Madison, WI 53706, U.S.A.

micropores in the pore walls. Fig. 3.1 shows a schematic of the SBA-15 structure and also compares it to that of MCM-41. In fig. 3.1b, the dark curves in the pores walls represent the micropores that connect between the mesopores. These micropores are much smaller (0.5-1.5 nm) than the main mesopores and are believed to be produced by surfactant chains penetrating the silica matrix during synthesis. The micropores affect the adsorption characteristics of SBA-15 by increasing the roughness of the mesopore surface. Moreover, the inner walls of the micropores act as additional adsorption surfaces for the smaller molecules such as hydrogen and argon. The result is an increase in the adsorbed amount per unit volume of the mesoporous substance.

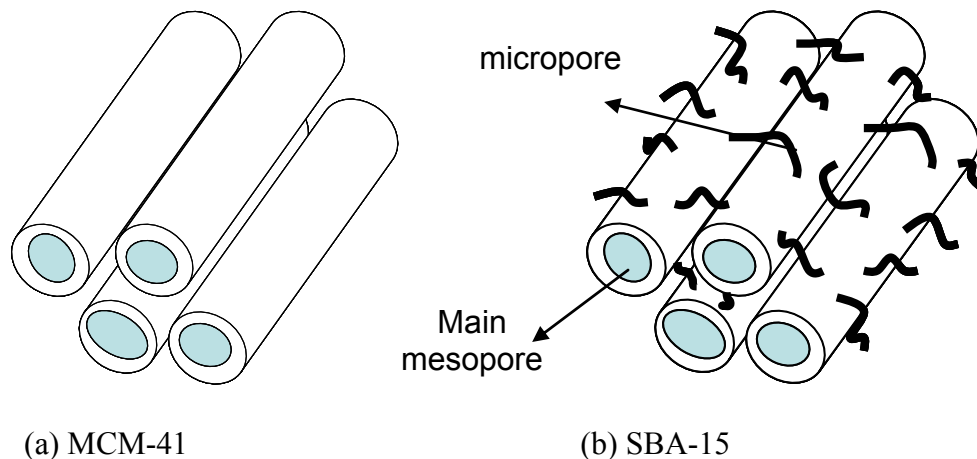


Fig. 3.1. Schematics of TMMs. (a) MCM-41. The cylinders represent the pores, (b) SBA-15. The dark curves represent the micropores within the pore walls.

The existence of microporosity in SBA-15 has been indirectly inferred from gas adsorption and Small Angle X-Ray Scattering (SAXS) [15-17]. Properties of the micropores, such as the size distribution and the percentage porosity, can be calculated

from adsorption data. On the other hand, a direct observation of the micropores is difficult even in the highest resolution TEM images of the SBA-15 structure. Liu *et al* [18] have reported observing the micropores in their High Resolution TEMs (HRTEM) of SBA-15. Alternatively, TEMs of the inverse platinum or carbon replicas of SBA-15 show the micropores as nanowires connecting the mesopores. However, since the micropore sizes are very close to the atomic length-scale, it is difficult to separate in a high resolution micrograph the mass thickness contrast contributed by the micropores and the phase contrast due to the wall atoms. Therefore from experiments, we know the following; (1) the percentage of total porosity contributed by the micropores, (2) the size distribution of the micropores. What we do not know is what the micropores actually look like, for example whether they are straight cylindrical channels or irregularly shaped tortuous cavities. As a result, simulations are needed to complement the information provided by the experiments in creating a detailed atomistic model.

Here we present a molecular model for SBA-15 incorporating both the surface roughness and the microporosity. Such molecular models are useful in studying the various confinement phenomena, for example, adsorption, phase transitions, diffusion and chemical reactions inside nanopores. These confinement phenomena are influenced by the irregularities and roughness of the mesopore surface. Therefore mesoporous materials such as SBA-15 and MCM-41 cannot be modeled in terms of simple geometries such as regular cylinders, which are unable to capture these irregularities. One possible approach would be to modify the regular cylindrical model by artificially introducing the surface

roughness and the microporosity. However, such models may not represent the structure of the real SBA-15 because we do not have detailed geometrical information regarding the surface roughness or the micropores from the experiments. It is therefore preferable to use mimetic simulations, where the structure evolves inside the simulation box in the same way as in the real world. In developing our model, we mimicked the synthesis of SBA-15 by simulating surfactant self-assembly. Thus in our model, the pore surface undulations originate from the fluctuations in the size of the surfactant micelles, similar to the experiments. Also the micropores are incorporated using the locations of the surfactant chains in the mimetic simulations. Therefore the micropores in our model follow the orientations adopted by surfactant chains in thermodynamically equilibrated self-assembled structures. These are some of the features which make our model representative of the real structure. We have already developed a model for MCM-41 following a similar procedure [19,20]. The present work applies this technique in developing an SBA-15 model and also incorporates the improvement suggestions prescribed in the previous papers [19,20].

Besides mimetic simulations, other alternative strategies exist in the literature for modeling mesoporous materials. The models proposed for MCM-41 have been reviewed by Sonwane *et al* [21]. In some of the models, silica walls are grown on the sides of hexagonally ordered regular cylinders which act as the template [21-24]. The model parameters such as the pore diameter, wall thickness and the wall silica density are taken from the experimental results. The pore surface roughness in such models is contributed

by the removal of wall atoms based on certain predefined criteria. In our model too, unbonded and unsaturated wall atoms were removed, which contributed to a part of the surface roughness. Coasne *et al* [19,20] developed models for MCM-41 by carving out the pore morphology in a silica block. In their model, the pore morphology was obtained from Lattice Monte Carlo (mimetic) simulations. Using simulated neutron scattering results, the authors concluded that the model was too rough compared to MCM-41 at atomic length-scales. However the correct surface roughness was preserved at higher length-scales. The effects of pore surface irregularities on adsorption behavior have been studied by Puibasset [25]. Several different models were considered, one of them having geometrical undulations in the pore surface, the other showing fluctuations in the fluid-wall potential while having a regular cylindrical pore surface. Fluctuations in the fluid-wall potential were found to influence the adsorption characteristics more strongly than simple geometric undulations. In a related study, Coasne *et al* [26-28] considered several different pore morphologies including rough cylinders, pores with constrictions and non-cylindrical cross-sections. The authors pointed out that surface roughness increased the overall adsorption, while constrictions in the pore cavity shifted the capillary condensation pressures to lower values. Neimark *et al* [29] modeled the fluid-wall potential in MCM-41 based on adsorption data on reference nonporous silica surfaces. Although efforts have been spent in studying the effect of surface roughness, relatively fewer studies exist in modeling microporosity. Recently Kuchta *et al* [30] have introduced microporosity in their MCM-41 models by placing stationary adsorbate

molecules close to the pore surface. However in their models, microporosity is manifested as a form of surface roughness rather than as channels in the pore walls.

3.2. Procedures

In this section, we will discuss the techniques used in simulating the synthesis of SBA-15 and characterizing the model structure. We have used Lattice Monte Carlo in order to simulate the material synthesis and a variety of methods for characterization, such as simulated TEM (transmission Electron Microscopy), AFM (Atomic Force Microscopy) and calculation of the pore size distribution, surface area and finally argon adsorption.

3.2.1. Mimetic Simulation

Lattice Monte Carlo has been used to simulate the synthesis of SBA-15. The method was used previously to develop models for MCM-41 [11,12] and Mesoporous Cellular Foams (MCF) [13]. In order to simulate the synthesis of TMMs, we need to simulate surfactant self assembly, which involves systems consisting of thousands of surfactant chains. Given the speeds of today's computers, atomistic simulations prove insufficient in handling such large systems. Therefore, mesoscale simulation methods such as Lattice Monte Carlo [31-33] need to be used, where the surfactants and the solvents are coarse-grained in order to reduce the effective number of particles in the simulation box. The details of the system used in this work have been described previously [13]. Our system

consists of model triblock surfactants ($H_3T_3H_3$, where H: head, T: tail), water, oil and silica, where the surfactants are modeled as chains of beads on adjacent lattice sites and the solvent molecules occupy single lattice sites. Fig. 3.2 shows a schematic of the simulation box, where the surfactants and the solvents are denoted by the different colored beads. The interactions between the adjacent lattice sites are modeled as square well potentials and the effective interaction parameters are given in table 2.1. The interaction parameters are selected so that the surfactant head-groups attract water while the tail-groups attract oil, similar to the experiments. The silica species is more attractive towards the head-groups compared to water. The system is equilibrated using a variety of moves including reptation, twist and chain regrowth by configurational bias [34]. The size of the simulation box is selected to be sufficiently large so as to avoid system size effects on the ordered structures. In our simulations, we have observed phase equilibrium between two or three phases. In order to calculate the phase concentrations, we have employed elongated simulation boxes which help to minimize curved interfaces. Once the system is equilibrated, the surfactants, water and oil are removed from the system and the remaining silica particles represent the mesoscale SBA-15 structure.

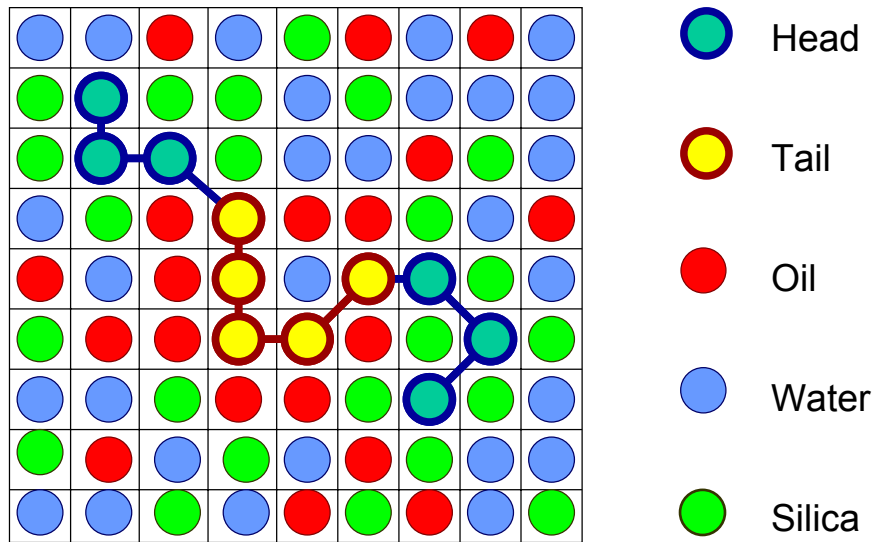


Fig. 3.2. Schematic of the simulation box. The color codes are the follows: Yellow-head, sea green-tail, red-oil, blue-water, green-silica.

3.2.2. Atomistic Modeling

Once the mesoscale structure is obtained, geometrical interpolations are used to convert the structure into an atomistic model. The mesoscale model consists of silica particles separated from each other by a distance of about 4 nm. From the mesoscale configuration, the silica particles that are located on the mesopore surface are first identified. The pore surfaces are then modeled as b-splines [35], where the control points are given by the coordinates of the silica particles that make up the mesopore surfaces. Fig. 3.3a shows the mesoscale model obtained through Lattice Monte Carlo simulations and fig. 3.3b shows a single pore and the surface points. Fig. 3.3c shows the pore surface modeled as a b-spline using the surface points as control vertices.

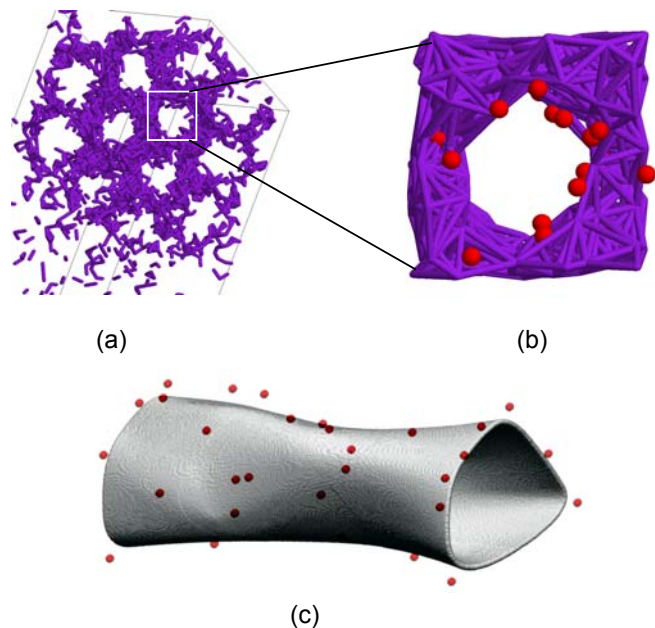


Fig. 3.3. (a) mesoscale structure; (b) single pore with surface points shown in red; (c) pore surface modeled as b-spline with surface points shown in red

In the next stage, the pore surfaces are carved out of a solid silica block where the Si, O and H atoms are arranged in a cristobalite lattice. The methodology followed here was originally proposed by Pellenq and Levitz to model Vycor glasses [36]. The atomistic model consists of four pores at four corners of the simulation box with a fifth pore at the center. This constitutes a unit cell for the hexagonally ordered SBA-15, which can then be replicated to form a repetitive structure. The resulting structure is shown in fig. 3.4a. where the violet regions represents the pore surfaces. Next, the micropores are carved out using the coordinates of the surfactant chains. From experiments, we know that the micropores have a wide size variation ranging from 0.5 to 1.5 nm. Therefore in our model, the micropore sizes are randomly selected from a Gaussian distribution with a

mean of 0.8 nm and are allowed to vary between 0.6 and 1 nm. Since the statistics of many random natural processes follow Gaussian distributions, our choice of the micropore diameters should be close to the experimental micropore size distribution. The structure obtained after carving out the micropores is shown in fig. 3.4b. After carving out the meso- and micro-pores, the silicon atoms which are in an incomplete tetrahedral environment are first removed. The oxygen atoms with two dangling bonds are next removed and those with one dangling bond are saturated with hydrogen atoms. This procedure ensures that the simulation box is electroneutral and that none of the silicon and oxygen atoms have dangling bonds. Finally, the pore surface was relaxed by randomly displacing all the atoms in the system by a small distance in order to create an amorphous structure. This procedure ensures that the model is consistent with the amorphous wall structure of SBA-15 reported in the experiments. The final structure is shown in fig. 3.4c and the repetitive structure by replicating the unit cell is shown in fig. 3.4d.

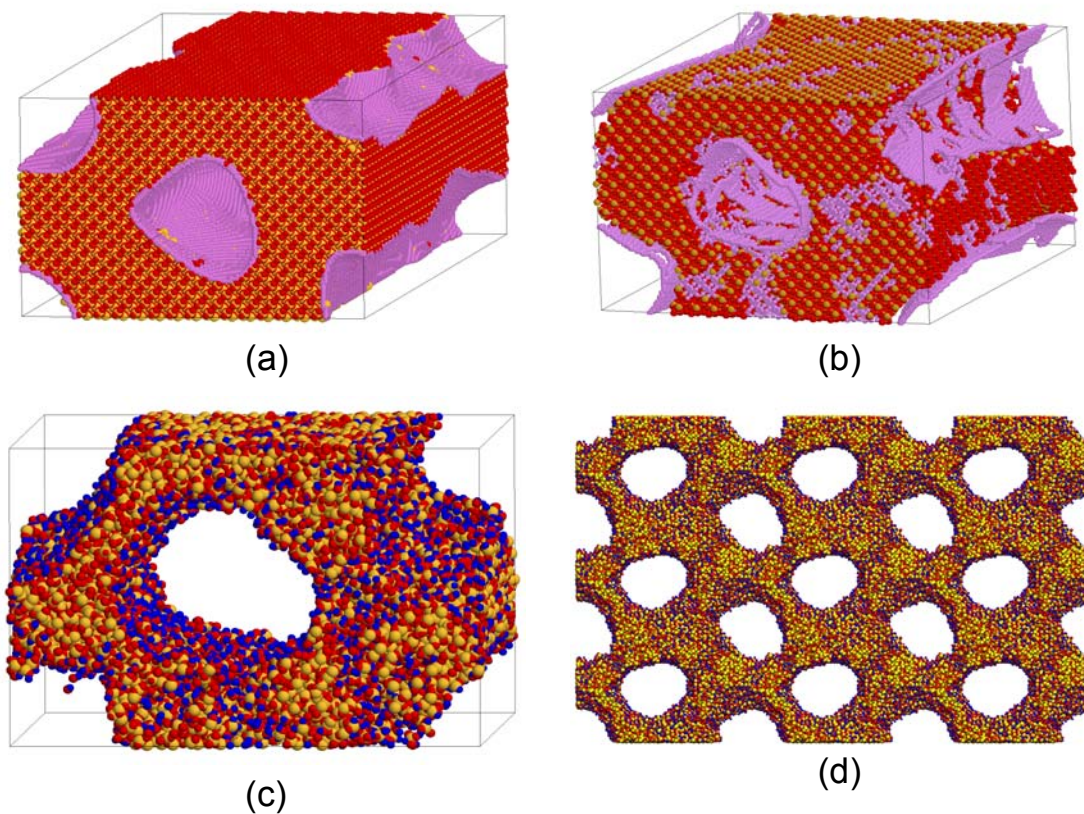


Fig. 3.4. (a) Structure obtained by carving out the mesopores; (b) Structure after carving out the micropores; (c) The final structure after removing the unbonded atoms, saturating the dangling bonds with hydrogen and randomizing; (d) The repetitive structure obtained by replicating the unit cell. Color code: Yellow-Silicon, Red-Oxygen, Blue-Hydrogen, Violet-Pore surface

3.2.3. Characterization Methods

This section describes the techniques used in characterizing the atomistic SBA-15 model.

3.2.3.1. Pore Size Distribution

The pore size distribution is obtained from the atomic coordinates in the model structure. The definition of geometrical pore size is given in [37] and [38]. The geometrical pore size at a given point is defined as the largest sphere that can be constructed encompassing the given point. We have developed a new technique based on nonlinear optimization that allows us to find the pore size in a fast and efficient way. The details of the method including the mathematical formulation is given in [38]. In order to find the pore size distribution, points are selected randomly inside the simulation box and the pore sizes are calculated at these points. Then a cumulative histogram $H(D)$ is constructed, where $H(D)$ represents the probability of finding a point in the model space with a pore size greater than or equal to D . The pore size distribution $P(D)$ is the negative of the differential coefficient of $H(D)$ with respect to D ; i.e.

$$P(D) = -\frac{dH(D)}{dD} \quad (3.1)$$

In order to get an accurate estimate of the PSD, the trial points should be uniformly distributed throughout the simulation box. Also in order to achieve a statistically representative distribution, the final PSD should be an average of the PSDs from several

unit cells. In our calculations, we have used five unit cells with a total mesopore length of 75 nm. While calculating the PSD, the porosity may be obtained as the ratio of the number of points with a non-zero pore size to that of the total number of trial points.

3.2.3.2. Pore Surface Area

The pore surface area can be obtained by rolling an adsorbate molecule over the pore surface and calculating the resulting surface area. This interpretation of the pore surface comes from the definition of the molecular surface. Several definitions of the molecular surface are given in the literature [37,39] and are obtained by rolling a test probe along the outer edges of a large molecule such as a DNA or a polymer. The surface traced by the center of the test probe is called the solvent accessible surface, while the surface traced by the inward-facing part of the probe sphere (the part that is in contact with one or more atoms of the molecule) is called the Connolly surface [39,40] as demonstrated in fig. 3.5. In our work, we have used the definition of Connolly surface in calculating the pore surface area. The surface area has been calculated using stereological analysis where randomly oriented straight lines are constructed inside the simulation box. The points of intersection of these straight lines with the pore surface are then counted. Let $l_1, l_2, l_3, \dots, l_n$ be the lengths of the line segments and $p_1, p_2, p_3, \dots, p_n$ be the number of intersections for each segment. The surface area per unit volume is given by

$$S_V = 2 \frac{\sum_{i=1}^n p_i}{\sum_{i=1}^n l_i} \quad (3.2)$$

The proof of this expression is given in ref. 41. A large number of line segments need to be sampled in order to get an accurate surface area estimate. This technique has been used by Gelb and Gubbins [37] in computing the surface areas of controlled pore glasses.

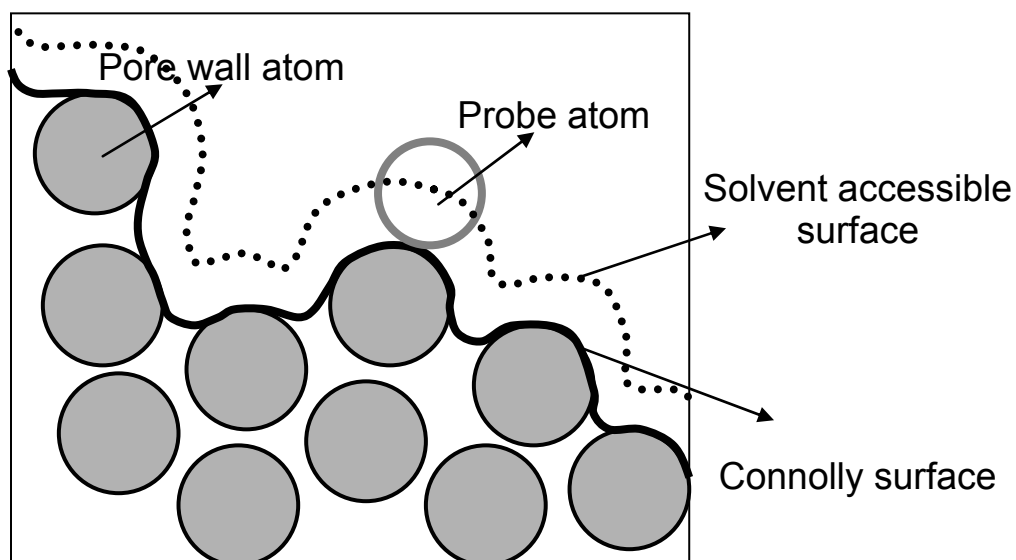


Fig. 3.5. Definitions of molecular surface. The continuous curve represents the Connolly surface while the dotted curve represents the solvent accessible surface.

3.2.3.3. Simulated Transmission Electron Micrograph

High Resolution TEM (HRTEM) of the model SBA-15 structure has been simulated following the multi-slice approach by Cowley and Moodie [42]. In this approach, the sample is divided into several thin slices perpendicular to the direction of the electron

beam. Then a thickness averaged electrostatic potential is calculated for each slice. Next the electron beam is propagated through each of the slices in sequence, so that the wave function calculated from a previous slice becomes the input for the next slice. Finally an image histogram is constructed from the amplitude distribution obtained at the end of the last slice. The image histogram plotted in greyscale represents the micrograph. There are very few assumptions or approximations in this technique. Given a sufficiently small slice thickness (0.2-0.3 nm), this method gives an accurate TEM of the model structure. As an example, for the TEM in the axial direction, the sample thickness is 15 nm and the number of slices used is 60. An accelerating voltage of 200 KV has been used for all the simulations. The TEM simulations have been carried out using the CERIIUSII® software.

3.2.3.4. Simulated Atomic Force Micrograph

In order to get an estimate of the surface roughness, we have simulated atomic force micrographs [43,44] of the inner mesopore surfaces in the model SBA-15. The AFM tip is scanned along the pore surface and the movement of the tip in the radial direction is recorded. Fig. 3.6 shows the schematic for the AFM calculation, where d is the perpendicular distance of the AFM tip from the pore axis and θ is the angle between the tip and the vertical. The AFM tip is spherical in shape with a radius r_p . To calculate the AFM, the tip is translated along the pore axis and then rotated through different angles (θ). For each position of the tip, the distance d is measured where the tip exactly touches

the pore surface. The mean deviations of d are then plotted in a surface plot, where the x axis represents the angle θ and the y axis represents the distance along the pore axis.

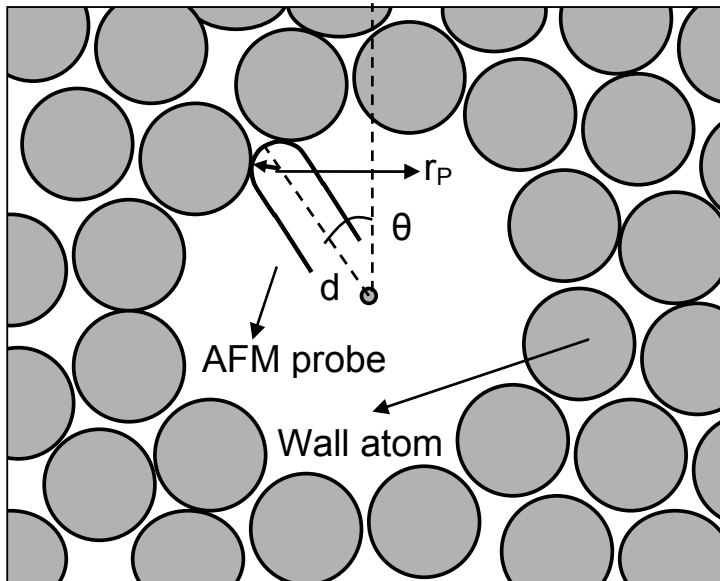


Fig. 3.6. Schematic for the simulation of AFM. The AFM probe is shown inside the pore touching the pore surface. r_P is the AFM tip radius, θ is the angle between the tip and the vertical, d is the perpendicular distance of the tip end from the pore axis.

3.2.4. Simulation of Argon Adsorption at 77K

Grand Canonical Monte Carlo (GCMC) simulation is used to simulate the adsorption of argon inside the model SBA-15 pores. In our system, argon-argon interaction is modeled as a Lennard-Jones potential with parameters, $\sigma=0.34$ nm and $\epsilon=121$ K. The interaction between Argon and the pore wall is modeled according to the PN-TrAZ potential (Transferable Potential for Adsorption in Zeolites) developed by Pellenq and Nicholson [45]. The potential is made up of the following terms: (1) interaction due to induced dipole, (2) dispersion interaction, which includes both two and three body terms and (3)

repulsive interaction. Both the dipole interaction and the dispersion interaction are obtained from electronic structure calculations, whereas the repulsive interaction is obtained from experimental data on isosteric heat of adsorption and the Henry's law constant in silicalite. This potential was originally developed for studying adsorption in zeolites, but can be easily extended to cover mesoporous silica materials, since the potential energy terms are calculated based on interactions with individual atoms of Si, O and H, and are therefore free of any inherent assumption regarding the silicalite structure. We now place the model SBA-15 structure in a simulation box with dimensions $13.55 \times 8.566 \times 14.97$ nm with periodic boundary conditions maintained in all directions. The system is then equilibrated at 77K using Monte Carlo simulations in the Grand Canonical Ensemble, where the chemical potential (μ), volume (V) and temperature (T) are kept constant. Starting from very low coverage, the chemical potential is increased in steps and the system is equilibrated at each step. The relation between the chemical potential and the system pressure is obtained from the equation of state for Lennard-Jones fluids by Kofke [46]. In the simulations, the chemical potential is increased until the pressure is equal to the saturation vapour pressure of Argon at 77K. While calculating the desorption branch, a similar procedure is followed. Starting from a maximum coverage, the chemical potential is decreased in steps until a sharp decrease in the adsorbed amount is observed. The isosteric heats of adsorption are calculated from the fluctuations in the internal energies of the adsorbate [47,48].

3.3. Results and Discussion

In this section, we first discuss the results for the mimetic Lattice Monte Carlo simulations. Then we show the results obtained by characterizing the model material and compare these results with the experiments. Finally we discuss the results for the simulation of argon adsorption inside the model pores. Again, comparisons have been made with the experiments whenever possible.

3.3.1. Mimetic Simulations

Here we discuss the results obtained by simulating the synthesis of SBA-15 using Lattice Monte Carlo simulations. By equilibrating mixtures of surfactant, oil, water and silica at different component concentrations, we are able to produce complete phase diagrams of the surfactant systems. In fig. 3.7 we show the aqueous phase diagram of the model surfactant $H_3T_5H_3$. The x axis represents the volumetric concentration of surfactant and the y axis represents the dimensionless temperature T^* , where

$$T^* = \frac{k_B T}{w_{HT}} \quad (3.3)$$

with k_B as the Boltzmann constant and w_{HT} as the coarse grained potential between a head and a tail bead of the surfactant. The ordered phases we observe depend on the surfactant concentration and the temperature. With increasing surfactant concentration, the sequence of the ordered structures (along with the range of surfactant concentration) is as

follows: spherical micelles (1%-25%) → elongated micelles (25%-55%) → hexagonally ordered cylindrical structures (55%-85%) → lamellar structures (>85%). At higher temperatures, the ordered phases disappear resulting in a homogeneous mixture. The approximate phase boundaries representing transitions from the ordered to the disordered phases are shown in the diagram.

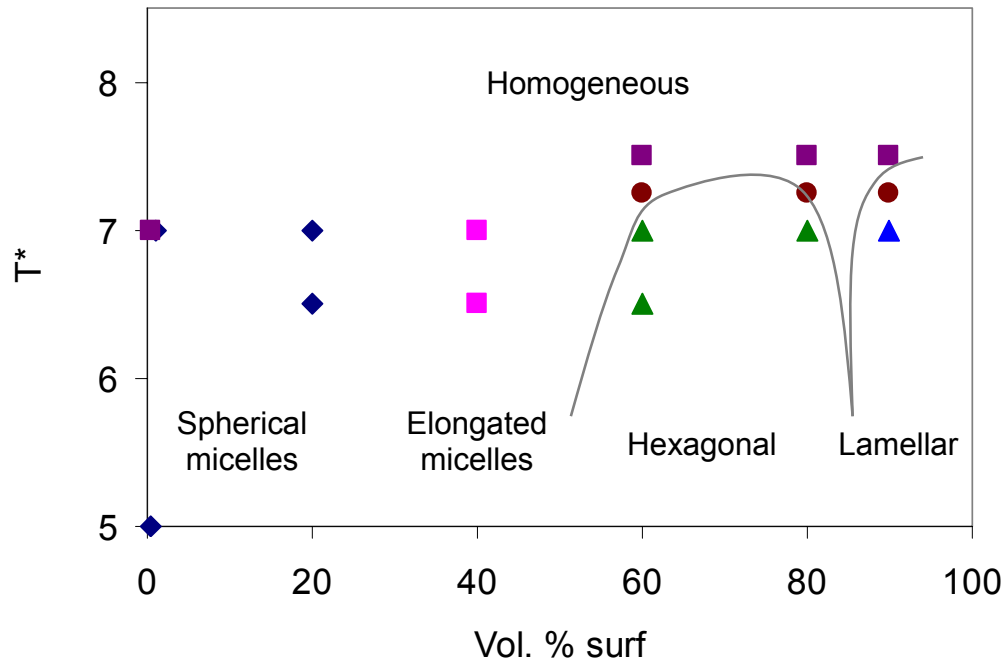


Fig. 3.7. Aqueous phase diagram of the surfactant $H_3T_5H_3$. The symbols represent the different ordered phases and the phase boundaries are marked by the continuous curves. (◆) spherical micelles, (■) elongated micelles, (▲) hexagonal phase, (▲) lamellar phase, (■) disordered, (●) phase boundary.

We now move on to the ternary surfactant-water-silica phase diagram. Fig. 3.8 shows the ternary phase diagram at $T^*=7.0$ where each vertex represents one pure component. We find a two phase region near the water side at low surfactant concentrations. Although the surfactant is completely miscible in water, adding a small amount of silica to the system

results in a phase separation between a surfactant rich, silica rich phase and a water rich phase. This is due to the strong affinity of the silica for the head-groups. Fig. 3.8 also shows the various ordered phases that appear at different component concentrations. Near the water side, the sequence of the phases with increasing surfactant concentration is already discussed in relation to fig. 3.7. Near the silica side, the sequence is as follows: spherical micelles → bicontinuous phase. It is unclear whether a lamellar phase appears at very high surfactant concentrations. We have not seen any lamellar phase for the points that were simulated at high surfactant concentrations near the silica side. We do not observe any hexagonal phase near the silica side. This is due to the strong head-silica attraction that increases the volume of the micellar coronas by introducing large amounts of silica in between the head-groups. The result is an increase in the curvature of the head-tail interface leading to highly convex structures such as spheres and bicontinuous phases.

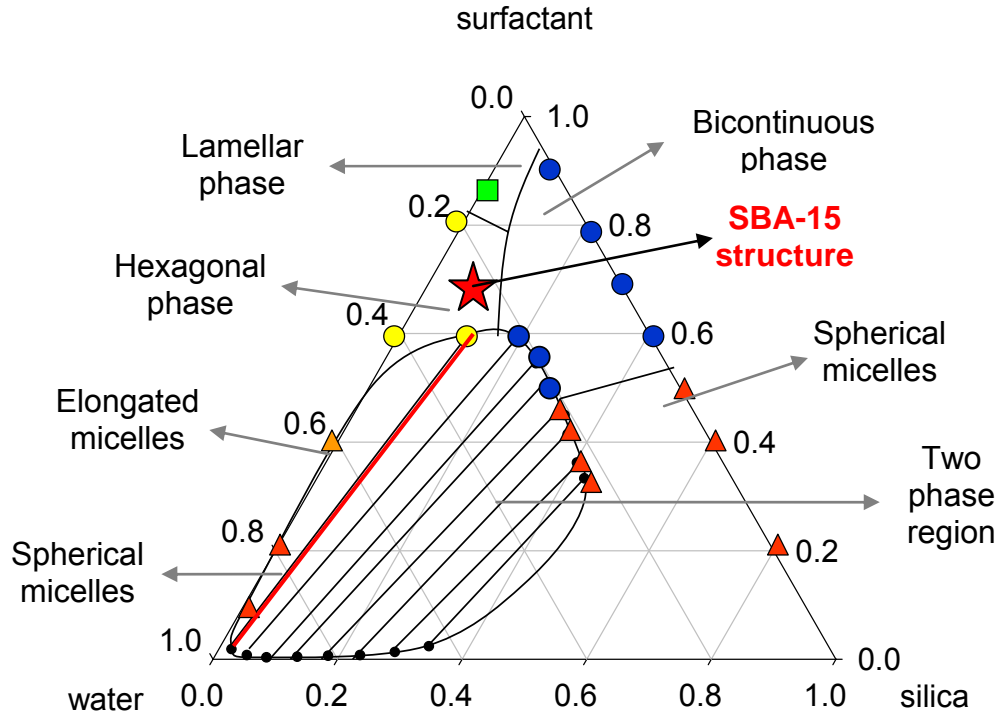


Fig. 3.8. Surfactant-water-silica phase diagram at $T^*=7.0$; simulation points are shown as follows: (\blacktriangle) spherical micelles, (\triangle) elongated micelles, (\circ) cylindrical micelles, (\bullet) bicontinuous phase, (\blacksquare) lamellar phase. Phase boundary lines are provided as a guide to the eye. The tie line marked in red represents the equilibrium between a surfactant rich and a water rich phase, where the surfactant rich phase forms the SBA-15 structures. The SBA-15 structures can be obtained at all points in the region marked by the red star

From the phase diagram in fig. 3.8, we are able to identify the region responsible for the formation of the SBA-15 structure. This is the region where a water rich phase is in equilibrium with a surfactant rich phase consisting of hexagonally ordered cylindrical structures. The tie line along which these structures appear is marked in red in fig. 3.8. The corresponding surfactant rich phase is marked by the red star. We now add oil to the system and study the effect of oil concentration on the SBA-15 structures. Starting from a point on the red tie line, the oil concentration is increased in steps and the resulting ordered structures are identified. We observe that the cylindrical geometry remains

unchanged at low oil concentrations, but transforms into lamellar and then to spherical structures as the oil concentration is increased. A detailed study of the effect of oil concentration on the self assembly has been discussed elsewhere [13]. We have also computed the surfactant-oil-water phase diagram. These results are omitted here for the sake of brevity but are discussed in [13] as well as in chapter 2.

The results of our mimetic simulations are qualitatively comparable to the phase behavior of the experimental surfactants. Both the order-disorder transition as well as the change in ordered structures with increasing surfactant concentration (as observed in fig. 3.7) have been experimentally observed in the aqueous surfactant phase diagrams. Experimentally, the surfactant-water-silica phase diagrams are not available. However we can compare the effects of oil concentration observed in the simulations to that of the experiments. On increasing the oil concentration during SBA-15 synthesis, Lettow *et al* [49] report a transition from cylinder to undulating cylinder to spherical structures, which is in partial agreement with the simulation results. We do not observe any undulating cylinders as reported in the experiments. On the other hand, the experiments do not report any lamellar structure, which is observed in our simulations.

3.3.2. Characterization of model SBA-15

In this section, we characterize the model SBA-15 structures, i.e. we calculate their physical properties such as the pore size distributions, internal surface areas, TEM and AFM.

3.3.2.1. Pore Size Distribution

Measuring pore size distribution is an important tool for characterizing porous materials. Experimentally, the pore size distribution is calculated from adsorption experiments. However, depending on the model / theory used in analyzing the adsorption data, such pore size distributions may be inaccurate [50]. Recently, accuracies in PSD calculation have improved through the use of Nonlocal Density Functional Theory (NLDFE). On the other hand, PSDs of model structures are exact because they are calculated using the atomic locations in the model. In Fig. 3.9 we compare the pore size distribution of the model SBA-15 to that of an experimental SBA-15 material. The x and the y axis are respectively the pore diameter in nanometers and the normalized probability density. Both the model and the experimental PSDs are qualitatively similar with bimodal distributions, where the rightmost peak represents the mesopores and the leftmost peak the micropores. The PSD for the model SBA-15 is shown in fig. 3.9a. The mean mesopore size in our model is 5.4 nm whereas the mean micropore size is 1.2 nm. Fig. 3.9b shows the PSD from an experimental SBA-15 with a comparable pore size. The

results for the experimental material are obtained from Ryoo *et al* [15]. The mean mesopore size in the experimental material is 6 nm and the micropore size is 1.06 nm, which are close to those of the model. Also the width of the mesopore peak is 2 nm in both the model and the experiments. Comparing figures 3.9a and 3.9b, it may be observed that the model has a higher micropore volume compared to the experimental material. We have calculated the relative micropore volume in our model. The percentage micropore volume is given by the area under the microporous part of the PSD, divided by the total area and multiplied by 100. Defining the micropores as pore sizes below 2 nm, the microporous volume in our model is calculated to be 28% of the total porosity. From experiments, we know that on an average the percentage microporosity in experimental SBA-15 is 30% of the total porosity [51]. Therefore, the experimental material to which the model was compared has lower microporosity than the usual SBA-15 materials. The model PSD also shows a secondary porosity between 2 and 4 nm. This is a characteristic of experimental SBA-15 materials which are heated to high temperatures after synthesis [51]. The experimental material from Ryoo *et al* [15] also shows some secondary porosity, although the amount is less compared to the model. The total pore volume in our model is 0.77 cc/gm, which is in agreement with the values obtained from the experiments (0.7-1.2 cc/gm).

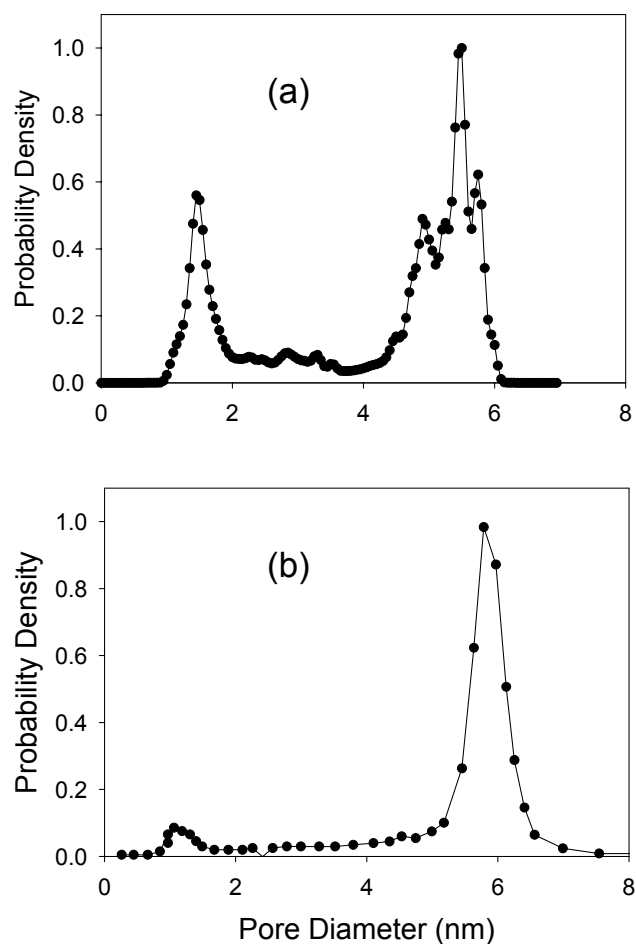


Fig. 3.9. Pore size distributions; (a) Model SBA-15, (b) Experimental SBA-15¹⁵

3.3.2.2. Surface Area

In the previous section, we characterized the SBA-15 model by measuring the PSD and the pore volume. However the most important parameter that controls the catalytic and adsorption properties of a porous substance is the internal surface area. It is defined as the area of the inner surfaces of the pore walls which are accessible to the external

(adsorbate/reactant) molecules. The net surface area available for adsorption depends on the size of the test particle (adsorbate molecule). We have calculated the internal surface area of the model SBA-15 as a function of the test particle radius and the results are shown in fig. 3.10a. The x axis denotes the test particle radius in nm (r_p) and the y axis denotes the surface area in m^2/gm , which is the common unit used in experiments for reporting surface area. Analyzing fig. 3.10a, we find that for $r_p=0$ nm, the surface area is approximately $3300 m^2/gm$. The surface area decreases rapidly with test particle radius until $r_p=0.1$ nm. Between $r_p=0.1$ and 1.0 nm, the surface area varies nonlinearly with test particle radius. Thereafter, the surface area exhibits a linear decay decreasing to zero around $r_p=2.5$ nm. We may now separate the surface area plot into three zones as shown in fig. 3.10a. Below $r_p=0.1$ nm, the surface area includes the regions in between the wall atoms (the intermolecular space) in addition to the micropores and the mesopores (zone 1). No molecule is small enough to fit into the intermolecular spaces (e.g. the van der Waals (vdW) radius of hydrogen is 0.12 nm). Therefore, the surface area contributed by the intermolecular spaces is not accessible to any adsorbate molecule. Above $r_p=0.1$ nm and below 1.25 nm, the surface area is contributed by the mesopores and the micropores and is accessible to the adsorbate molecules (zone 2). From the pore size distribution, we know that the majority of the micropores in the model SBA-15 have pore sizes below 1.25 nm. Therefore for $r_p>1.25$ nm, the surface area is contributed by the mesopores only (zone 3). The surface area decreases to zero at $r_p=2.5$ nm which corresponds to the average mesopore radius (2.7 nm). Zone 3 corresponds to the surface areas accessible to metallic nanoparticles (radius $\sim 1-2$ nm), which are experimentally deposited onto the

pore surfaces to impart special catalytic properties to the material [52]. From fig. 3.10a, it is possible to predict the accessible surface area from a knowledge of the adsorbate size. We now tabulate the radii of several common adsorbate molecules and the corresponding surface areas in table 1. For the SBA-15 model, the surface area for argon adsorption is found to be 931.21 m²/gm and is in agreement with the results obtained from adsorption experiments.

Table 3.1. Accessible surface area of the model SBA-15 as a function of adsorbate size

Adsorbate – vdW Radius (nm)	Accessible Surface Area (m²/gm)
Hydrogen – 0.12	1177.74
Nitrogen – 0.155	1035.4
Argon – 0.188	931.211
Krypton – 0.202	897.928
Xenon – 0.216	864.651
Metallic nanoparticles – between 1.0 and 2.0	between 279.44 and 76.6151

In order to study the effect of micropores on the internal surface area, we now compare the surface areas of the model SBA-15 to that of a model without the micropores. Fig. 3.10b shows the variation of surface area with test particle radius for two different models, model A consisting of both the micropores and the mesopores and model B consisting of only the mesopores. Only the zones 2 and 3 are considered here. Since the two models have different densities, surface areas per unit volume are compared instead of the surface areas per unit mass. Model B shows less surface area compared to model A for $r_p < 1.0$ nm. For higher values of r_p , the surface areas of both models are almost identical indicating that the micropores have negligible effect on the surface areas for $r_p > 1.0$ nm. We also plot the surface area contribution due to the micropores as the

difference between the areas from models A and B. The micropore contribution is initially high, decreasing rapidly with the test particle radius and becoming negligible for $r_p > 1.0$ nm. It may be observed that, between $r_p = 0.1$ and 0.25 nm, the micropores contribute up to 50% of the total surface area in the model SBA-15. In contrast, the total micropore volume is only 30% of the total porosity. The highly curved and tortuous nature of the micropores contribute towards the increased surface area to volume ratio as observed here. Therefore the micropores should have more influence on the confinement phenomena than is evident from the pore volume measurements. This result cannot be verified through experiments because, experimentally it is not possible to separate the surface area into micropore and mesopore contributions.

We now summarize the characterization results obtained so far. Table 3.2 lists the important parameters for the SBA-15 model and compares them to the experiments [53]. All the parameters listed here correspond to the adsorption of argon. It may be observed that, all the model parameters are in quantitative agreement with the experiments.

Table 3.2. Parameters for the model and the experimental SBA-15 [15]. Results correspond to Argon adsorption.

Parameter	Model SBA-15	Experimental SBA-15 [53]
Pore Volume	0.77 cc/gm	0.7-1.2 cc/gm
Mesopore volume as % of total porosity	72 %	70 %
Specific Surface Area	931.211 m ² /gm	600-1000 m ² /gm

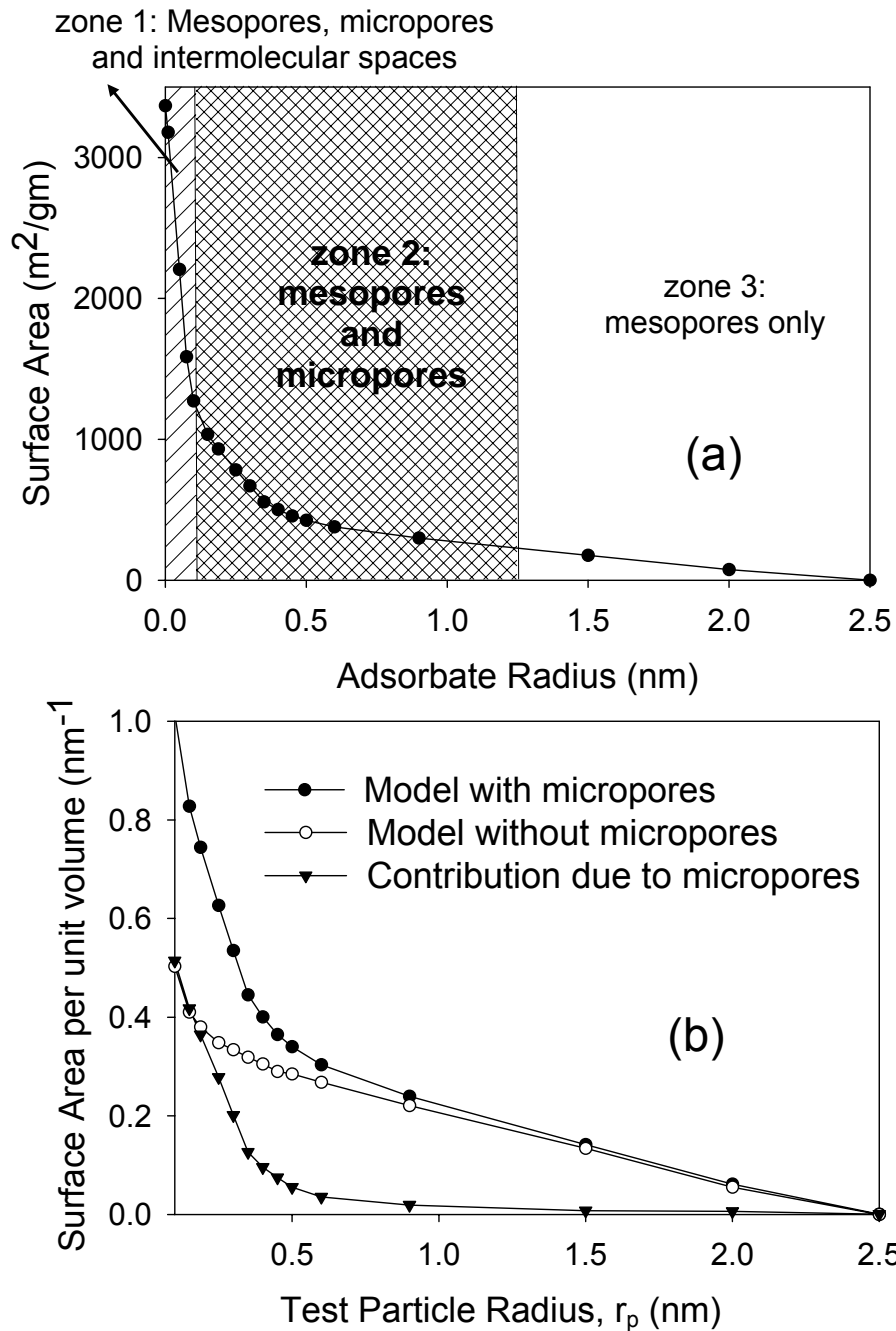


Fig. 3.10. (a) Variation of internal surface area per unit mass with test particle radius for the model SBA-15. The significances of the three zones are marked in the figure. (b) Comparison between the surface areas per unit volume of the model SBA-15 and the model removing the micropores. ● - Model with micropores; ○ - Model without micropores; ▼ - Contribution of the micropores towards the surface area.

3.3.2.3. Simulated TEM

In this section, we show the simulated TEMs of the model SBA-15 structures and compare them to the experimental TEMs. While the PSDs and the internal surface areas characterize the catalytic activities of porous substances, TEM images allow us to directly visualize the pore structures and identify the pore geometries. Experimentally, the normal resolution TEMs of SBA-15 samples reveal the hexagonal arrangement of cylindrical pores. However, the detailed structure of the microporous pore walls may only be studied using high resolution TEMs with magnifications greater than 100,000. In order to study the effect of the micropores on the TEM contrast, we have considered two different models: model A, including the micropores; and model B, with micropores removed. Fig. 3.11 compares the simulated TEMs of the two models, A and B. Two mutually perpendicular directions have been selected for the propagation of the electron beam, one of which is parallel to the pore axis (the axial direction), and the other one perpendicular to the pore axis (the transverse direction). These two directions are shown in the schematic of the simulation box at the end of fig. 3.11. Fig. 3.11a represents the TEM for model A taken in the axial direction, whereas fig. 3.11b represents the TEM taken in the transverse direction. In fig. 3.11a, the darker areas represent the pore walls and the brighter areas the pores. In fig. 3.11b, the darker areas represent the regions between the adjacent pores, where the electron beams traverse through a larger wall thickness compared to the lighter areas (see the schematic). We now show the simulated TEMs of model B, where fig. 3.11c represents the TEM in the axial direction and fig.

3.11d represents the TEM in the transverse direction. Next, we compare between the TEMs of the models A and B. Comparing the TEMs in the axial direction, it may be observed that the wall density in fig. 3.11a (the microporous model) is less compared to that in fig. 3.11c (model without micropores). The reduced wall density can be directly related to the presence of micropores in the pore walls. We also observe spatial variations in the wall density in fig. 3.11a, which indicates the local aggregations of micropores in model A. In comparison, fig. 3.11c (model B) shows a uniform wall density. The effect of the micropores is also observed in the TEMs taken in the transverse direction. There is no appreciable difference in the overall wall densities between figures 3.11b and d. However, spatial contrast variations are visible in fig. 3.11b, similar to fig. 3.11a.

We have also studied the effect of microscope parameters on the TEMs of the model structures. In high resolution TEMs, the image contrast is a result of two different phenomena. One is the amplitude contrast, which arises due to the scattering of electrons by the wall atoms and depends on factors such as the wall thickness and density. Second is the phase contrast, which arises due to interference between the scattered and unscattered electronic waves as a result of phase differences between the two. Phase contrast increases image contrast near the sharp edges such as the mesopore boundaries, whereas amplitude contrast is important in order to show the inner structures of the pore walls, such as the micropores. Usually, a slight under-focusing helps to improve image contrast by increasing the phase contrast, whereas high levels of under-focusing over-emphasize the phase contrast at the same time decreasing the amplitude contrast.

Therefore, the best image quality may be achieved by optimizing the degree of underfocusing, also termed defocus (expressed in angstrom). While calculating the TEMs, we have selected the defocus values which give sufficient edge contrasts while maintaining significant amplitude contrast in the pore walls. TEMs (axial direction) of the microporous SBA-15 model for several defocus values, d are shown in fig. 3.12. Above $d=-400$, spurious details in the TEM images in the form of bright fringes overshadow the micropore contrast in the pore walls. On the other hand, decreasing the defocus below $d=-550$ does not affect the image contrast. Therefore, we select $d=-550 \text{ \AA}$ as the optimum defocus. Similar procedures have been followed for all the other TEMs shown in fig. 3.11. The individual defocus values of the different images are listed at the bottom right corner of fig. 3.11.

In fig. 3.13, we compare the TEMs of the model SBA-15 with the high resolution TEMs of an experimental SBA-15. The experimental results have been reported by Liu *et al* [18]. An accelerating voltage of 200 KV was used for the experimental TEMs similar to the model TEMs. Fig. 3.13a and b show respectively the TEMs of the model SBA-15 structure in the axial and the transverse directions. In fig. 3.13a, the unit cell has been replicated in order to show the repetitive ordering. Fig. 3.13c and d represent the TEMs for the experimental structure. Fig. 3.13e represents the TEM for the non-microporous model (model B). On comparing the figures 3.13a and c, we find similar granular features in the pore walls of both the structures as shown by the white boxes in the figures. These granular features were interpreted by the authors (Liu *et al*) as direct evidence of the

micropores. We note that the pore walls of the non-microporous model also show granularities to some extent (fig. 3.13e). However, the size of the grains in fig. 3.13e are smaller compared to that of the grains in fig. 3.13a and are thus presumed to be due to the atomic contrast. On the other hand, both figures 3.13a and 3.13c show similar sized grains in the pore walls. Therefore, these grains are likely to be contributed by the micropores. However, we feel that it is still difficult to predict the sizes of the micropores by observing the TEMs, as attempted by the authors in ref. 18. The same arguments hold true for the images 3.13b and d. The overall contrast in each of the model TEMs is less compared to that of the experiments. This is probably due to the large thicknesses of the experimental samples. On the other hand, computational constraints restrict us from using larger samples in the TEM simulations. Finally we conclude that among the figures 3.13a, c and e, fig. 3.13a and c are more similar to one another compared to fig. 3.13e. In future, TEM technology will improve further allowing higher resolution imaging. We hope that our simulated TEMs serve as reference images for analyzing experimental TEMs of microporous structures.

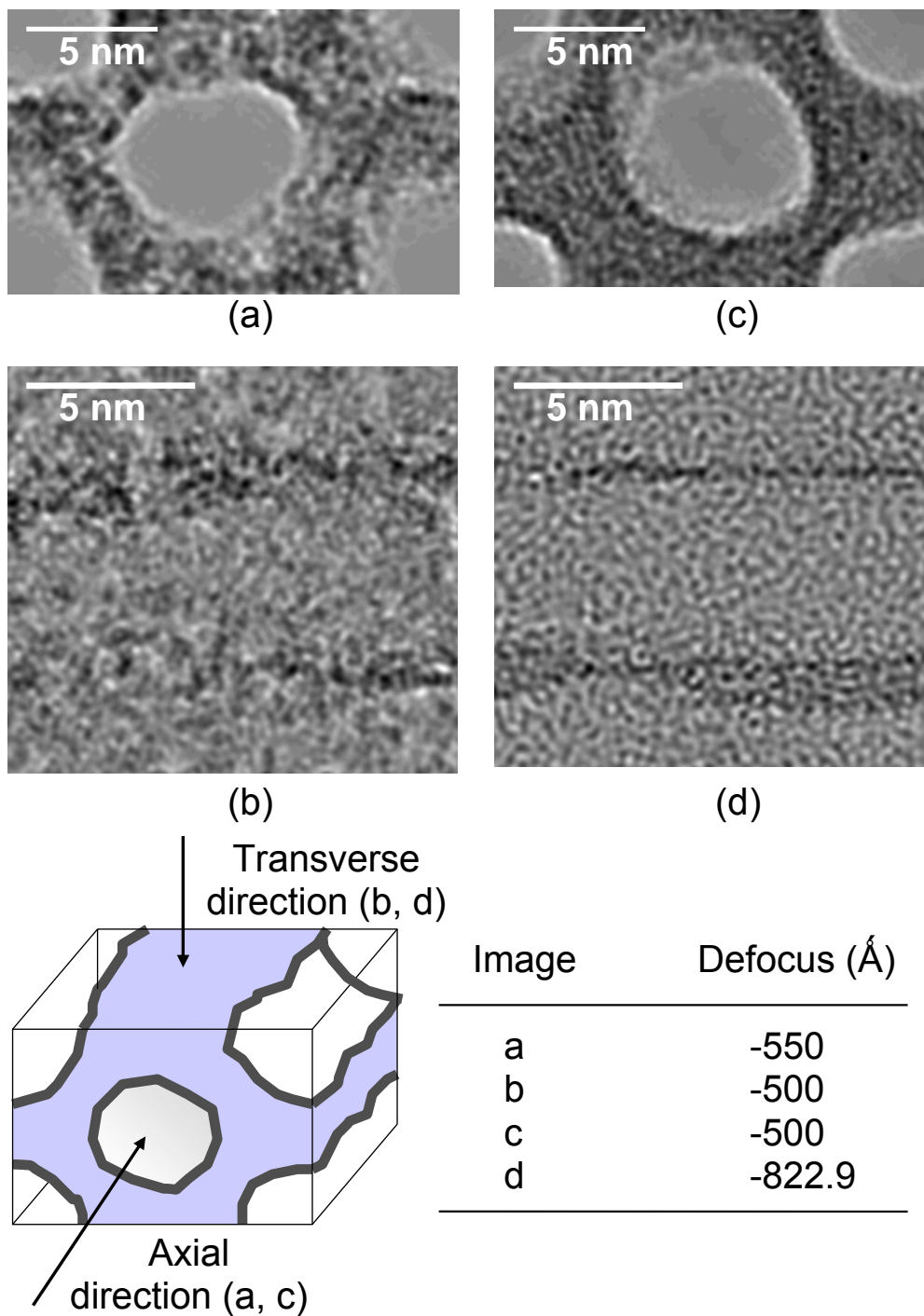


Fig. 3.11. Simulated TEMs of model structures. Model A represents the microporous structure and model B the non-microporous structure. (a) Axial view of model A; (b) transverse view of model A; (c) axial view of model B; (d) transverse view of model B. The axial and the transverse views are explained in the schematic. The defocus values for the individual images are tabulated.

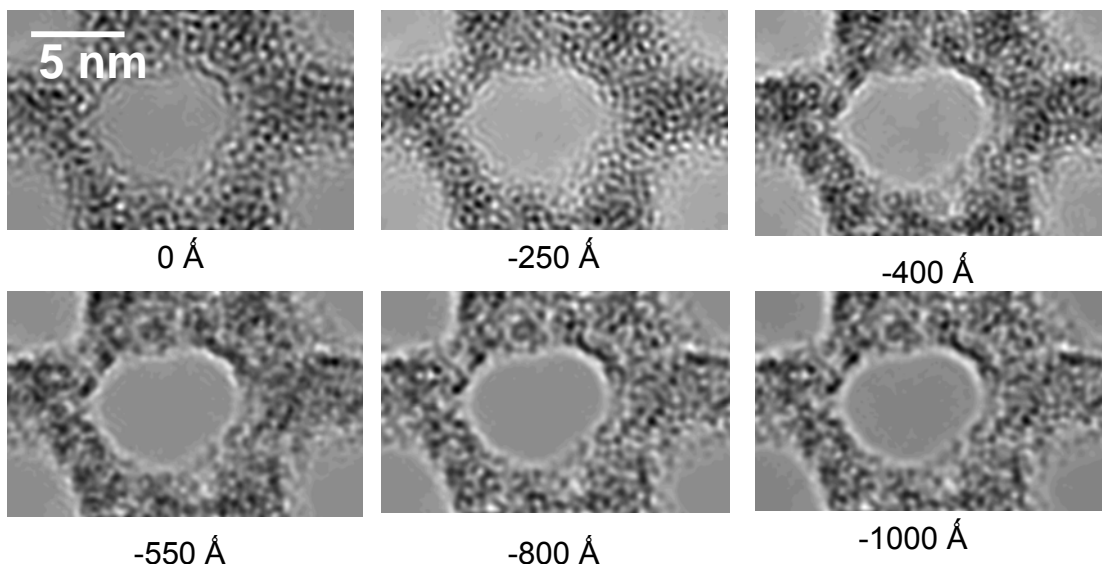


Fig. 3.12. Effect of defocus on the image contrast in the simulated TEMs of SBA-15. The defocus values are listed below the individual images.

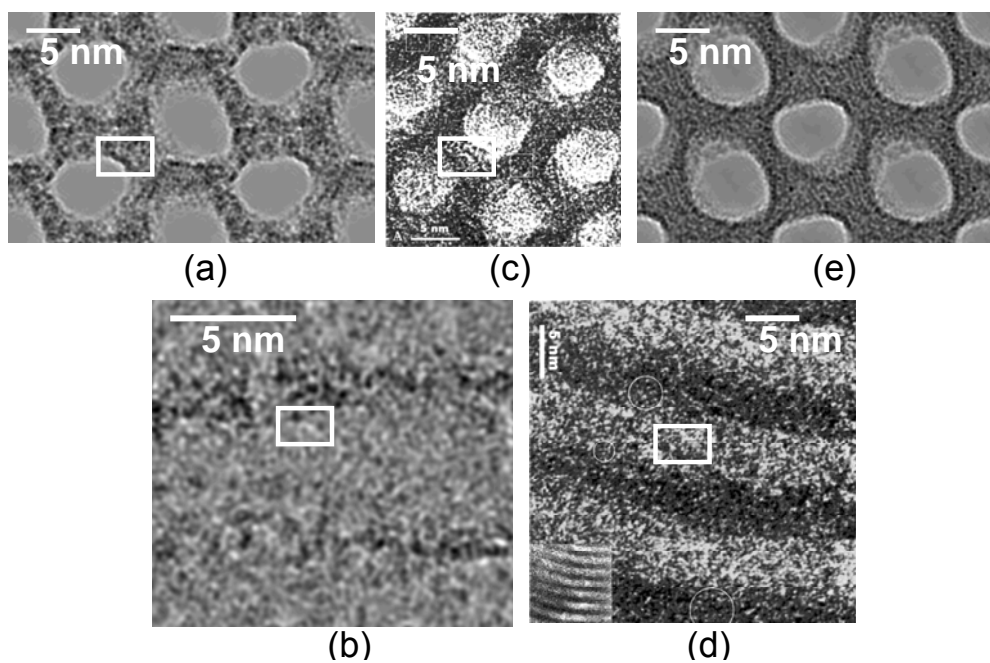


Fig. 3.13. Comparison between experimental [18] and model TEMs. (a) model SBA-15 (axial direction); (b) model SBA-15 (transverse direction); (c) experimental SBA-15 (axial direction); (d) experimental SBA-15 (transverse direction; (e) model without the micropores (axial direction). The white boxes represent regions showing similar contrast patterns.

3.3.2.4. Simulated AFM

In order to study the pore surface roughness, we have simulated the Atomic Force Micrographs of the mesopore surfaces in our model materials. Experimentally, AFMs are used not only to visualize rough surfaces, but also to quantitatively estimate the surface roughness. For quantifying the surface roughness, root mean square roughness (SR_{RMS}) of a heterogeneous surface is defined as follows:

$$SR_{RMS} = \sqrt{\frac{1}{N} \sum_{i=1}^N d_i^2} \quad (3.4)$$

where N is the number of sample points on the surface and d_i represents the deviation of the AFM tip at point i . Higher values of SR_{RMS} characterize highly rough surfaces whereas lower values indicate relatively smooth surfaces. We have calculated the RMS roughness of the mesopore surfaces in our models from the simulated AFM data. In our simulations, the radius of the AFM tip is equal to the size of an Argon molecule. As a result, the AFM micrographs represent the pore surface roughness experienced by Argon molecules during adsorption and are therefore relevant to the simulations of Argon adsorption discussed later. However, Our AFM results cannot be directly verified using experiments because it is physically impossible to place an AFM probe inside a mesopore. Fig. 3.14 shows AFMs of the two different models, A and B, defined in the previous section. The x and y axes represent respectively the angular position of the AFM probe expressed in degrees (please refer to fig. 3.6) and the distance along the pore axis (in nm). The z axis represents the deviation of the AFM tip measured in nm. In the

figures, positive deviations indicate depressions/holes in the pore surface whereas, negative deviations indicate the highlands and the peaks. This is exactly opposite to the regular convention. However, we found this representation more convenient for visualizing the pore surface compared to the regular convention. The surfaces are plotted in grey-scale with the shades of grey proportional to the deviations as shown in the color-bars. The values shown on the color-bars are in nm. In the AFM of model A (fig. 3.14a), pointed peaks are visible all over the surface representing the micropores. These are the attractive sites on the pore surface which are favorable for the adsorption of argon and other gases. Besides the micropores, periodic undulations are observed on the surface of the mesopore, which are contributed by the undulations in the micellar template and are related to the thermodynamics of the surfactant system. The periodicity of the undulations calculated from the AFM figure is approximately 7 nm. Apart from the undulations and the micropores, the mesopore surface consists of circular impressions caused by the wall atoms. Next, fig. 3.14b shows the AFM for the non-microporous model (model B). Here we observe all the features present in model A except the microporous peaks. We believe that by removing the micropores, this surface resembles the mesopore surfaces of non-microporous solids such as MCM-41. We have also calculated the RMS roughness in both models. For model A, the RMS roughness is 0.653 nm, whereas for model B the roughness is 0.578 nm. Due to the presence of the microporous ‘potholes’ on the pore surface, model A shows a higher roughness compared to model B. However, the two roughness values are close to one another showing that the micropores may not have a very significant influence on the RMS roughness. The reason

is that the total area covered by the micropores is less compared to the area covered by the micellar undulations, which is the controlling factor for the roughness in both models.

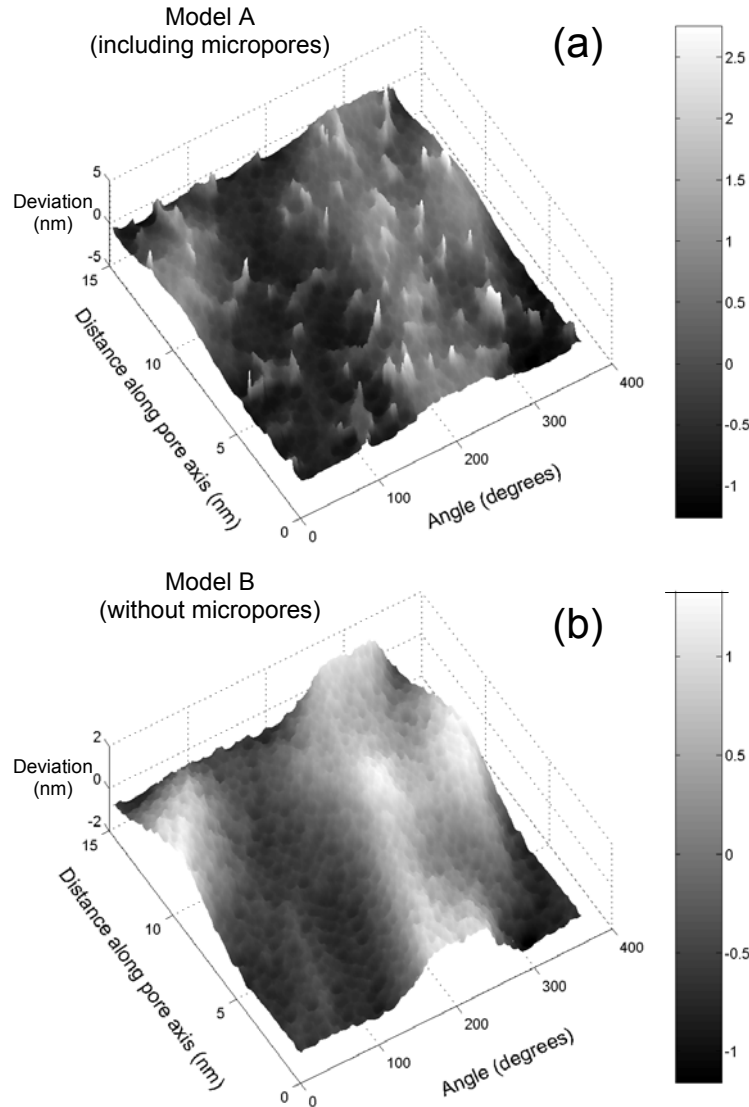


Fig. 3.14. Simulated AFMs for (a) Model A (with micropores; (b) Model B (without micropores). The x axis measures the radial inclination of the AFM tip with the vertical (degrees). The y axis measures the distance along the pore axis (nm). The z axis represents the mean deviation of the AFM tip (nm). In both figures, a positive deviation indicates a hole or a depression, while a negative deviation indicates an elevated region on the surface. The grey shades are proportional to the deviations according to the color-bars on the right.

3.3.3. Simulation of Argon Adsorption at 77K

In this section, we discuss the results for the simulations of argon adsorption inside the model pores. In order to investigate the effects of the micropores, argon has been selected as the adsorbate. Due to the small molecular radius, argon molecules are able to explore the interior of the micropores in a more efficient way compared to larger molecules. We have selected a simulation temperature of 77K so that the results can be compared to the adsorption experiments, which are often carried out at 77K. The adsorption behavior has been compared between three different pore models. Fig. 3.15 shows the axial and transverse cross sections of the three models by cutting through the middle of the simulation boxes. Both models A and B consist of cylindrical mesopores having surface roughness. The model A however incorporates the micropores in the pore walls, whereas in model B there are no micropores. Model C consists of regular cylindrical pores (no surface roughness) with no micropores in the pore walls. Therefore, model A represents SBA-15 and model B represents non-microporous substances such as MCM-41. Finally, the results from model C will be used to analyze how the adsorption properties of SBA-15 differ from those in an ideal geometrical model. First we report the adsorption isotherm for model SBA-15 (model A) in fig. 3.16a. The x axis represents the relative pressure (P/P_0 : pressure, P_0 : saturation vapor pressure of Argon at 77K, arbitrary units) and y axis represents the adsorbed amounts in cc/gm. At low pressures, the adsorption curve shows a steep slope which decreases at higher pressures. The steep slope is due to the high energy sites on the microporous walls which result in increased rates of adsorption. Around $P/P_0=0.2$, the micropores get completely filled and a monolayer builds up on the

surface of the main mesopores. Between $P/P_0=0.2$ and 0.5 , adsorption proceeds via the monolayer-multilayer mechanism resulting in the linear slope of the adsorption curve. The first sign of capillary condensation is observed at a relative pressure of 0.5 indicated by a sudden jump in the adsorption curve. Then the adsorption curve temporarily flattens out around $P/P_0=0.6$. This behavior is due to the formation of intermediate phases and has been previously observed in the adsorption simulations [25]. Finally, at a relative pressure of 0.67 , the pores become completely saturated with the adsorbate and henceforth, there is very little increase in the adsorbed amount with increasing pressure. The desorption branch is indicated by the filled circles. Starting from a set of completely filled pores, as the pressure is decreased there is negligible change in the adsorbed amounts until a relative pressure of 0.2 . At $P/P_0=0.1$, there is a sudden decrease in the adsorbed amount and thereafter, the adsorption and desorption follow the same curve. Therefore we find a wide hysteresis in the isotherm for the model SBA-15 which is different from the experiments, where the hysteresis is much narrower. This difference arises from the separate mechanisms for desorption followed in the experiments and the simulations and has been discussed elsewhere [19]. In the experimental desorption, the adsorbed phase is in equilibrium with a bulk gas phase, whereas in the simulations, the bulk gas phase does not exist. Here desorption proceeds via the nucleation of gas bubbles leading to a different behavior compared to the experiments. We now analyze the results in fig. 3.16b, which display the adsorption branches from the three models, A, B and C as well as the experimental isotherm from a SBA-15 sample with a pore diameter of 5.4 nm (similar to the models). Among the three models, the amounts adsorbed by model C are

the lowest followed by model B. The increased adsorption in model B is due to the presence of surface roughness. However, the adsorption isotherms for models B and C are close to one another. Compared to both models B and C, the adsorbed amounts for model A are much higher due to the presence of the micropores. In model A, the micropores increase the adsorbed amounts by (a) increasing the mesopores surface roughness, (2) offering additional adsorption surfaces in the form of channels in the pore walls. The effect of the micropores is best observed at very low pressures (below $P/P_0=0.01$), where the amounts adsorbed in model A are significantly higher compared to models B and C. The average pressure for capillary condensation is similar for all the three models. This is consistent with the fact that the capillary condensation pressure is mainly dependent on factors such as the pore size, adsorbate and temperature and is relatively less influenced by the presence of the micropores. However, differences exist among the isotherms of the three models near the capillary condensation pressures. While model C shows a vertical jump in the adsorption curve, models A and B show a gradual increase in the adsorbed amounts with the formation of intermediate phases. Comparing models A and B, we observe that the capillary condensation in model B takes place at slightly lower pressures compared to model A (P/P_0 : 0.5-0.67 in model A vs 0.45-0.63 in model B). This may be due to the undulations in the mesopore surface acting as constrictions. Coasne *et al* [26-28] reported that the constrictions in the pore cavity can decrease the capillary condensation pressure. Here, undulations are clearly observed in the cross-section of model B as shown in fig. 3.15, while they are less prominent in model A. In model A, carving out the micropores reduced the undulations in the wall

geometry, leading to an almost straight cylindrical mesopore. Therefore, the effects of the surface undulations are partially negated by the presence of the micropores. In fig. 3.16b, the desorption branches are not shown for clarity. All three models have very similar desorption curves, suggesting that the desorption properties are not influenced by the presence of the micropores. We now compare the model isotherms with that of an experimental SBA-15 with similar pore size. The experimental results were reported by Galarneau *et al* [17]. The adsorbed values in the experimental isotherm are close to those predicted by model A and are higher than those predicted by models B and C. Comparing between model A and the experiment, model A over-predicts the adsorbed amounts below $P/P_0=0.7$. However, the adsorbed amounts at 100% loading are almost identical in both the experiment and the model. In experiment, the capillary condensation takes place between relative pressures of 0.55 and 0.74, which is comparable to that of model A (0.6-0.67). The reason for the increased adsorption amounts in model A may be because of a higher micropore volume compared to the experimental sample. However, the micropore volume in experimental SBA-15 depends on factors such as the anneal temperature. On the other hand, the micropore volume in our model can be controlled by changing the modeling parameters, such as the mean of the Gaussian distribution (see section 3.2.2).

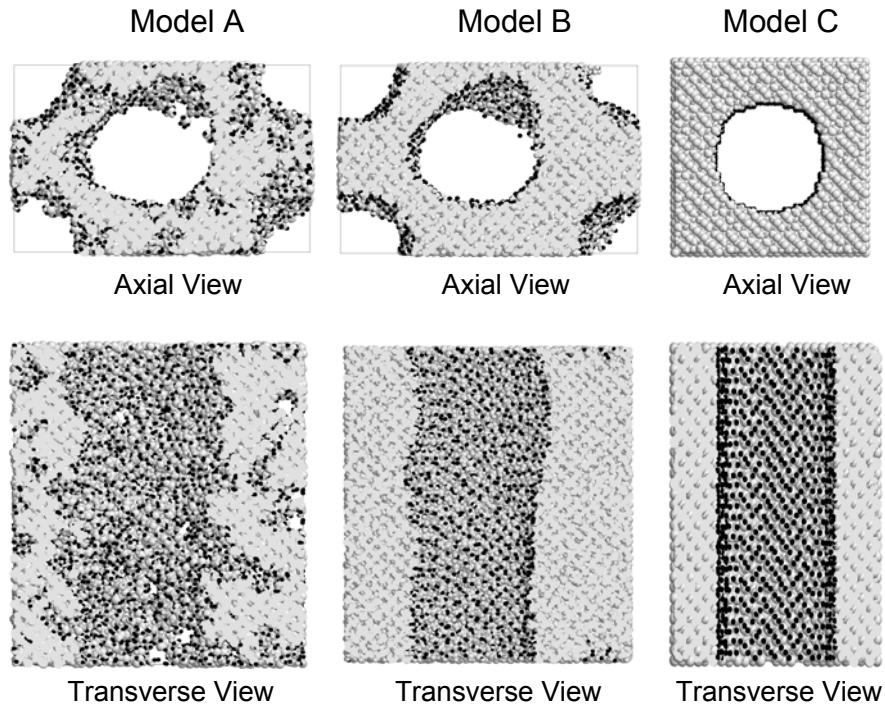


Fig. 3.15. Cross sections of the different models used in studying adsorption. Silicon and Oxygen are represented in grey while Hydrogen is represented in black. Model A incorporates both surface roughness and micropores. Model B incorporates surface roughness without any micropores. Model C is the regular cylindrical model with the same pore diameter as models A and B.

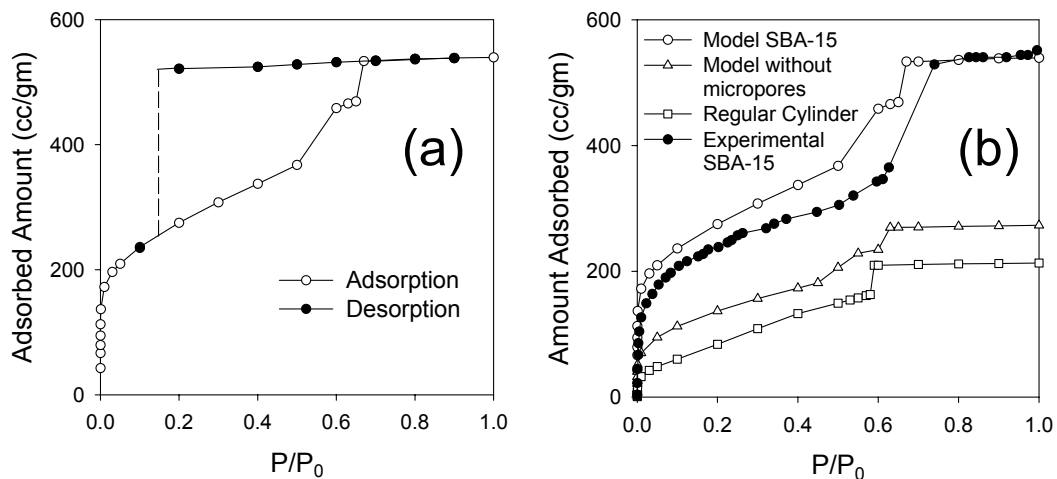


Fig. 3.16. Adsorption isotherms for (a) Model A -○-: Adsorption, -●-: Desorption; (b) Comparison among the various pore models. -○-: Model A, -△-: Model B, -□-: Model C, -●-: Experimental SBA-15 (Galarneau *et al* [17]). The x axis represents the relative pressure and y axis the adsorbed amount in cc/gm.

We now analyze in detail the adsorption isotherm for model A. Fig. 3.17 shows the adsorption isotherms along with the simulation box snapshots. For clarity, the isotherm has been split into low pressure and high pressure regimes. At very low pressures, the argon molecules are mainly adsorbed inside the micropores whereas the mesopore surface shows very little or no adsorption ($P/P_0=10^{-10}$). As the pressure increases, adsorption takes place on both the mesopore and the micropore surfaces ($P/P_0=0.001$), and at $P/P_0=0.1$ a monolayer is formed on the mesopore surface. At this point, the micropores are almost completely saturated with adsorbate. Next, we see several layers formed on the mesopore surface at $P/P_0=0.5$, which is also the onset of capillary condensation. The snapshot at $P/P_0=0.6$ represents an intermediate phase formed within the condensation regime and $P/P_0=0.67$ represents the completely filled pore. Although the adsorbate concentrations are different in the two phases, it is difficult to understand by seeing the snapshots. Next we analyze the influence of the micropores on the adsorption properties. One way to do this is by measuring the adsorbate distribution with pore size. Fig. 3.18 shows the distribution of argon molecules with pore size at two different pressures along with the simulation box snapshots. The pore size distribution is also shown as reference. The adsorbate distribution at a relative pressure of $P/P_0=10^{-10}$ is plotted in fig. 3.18a. At such a low pressure, the Argon molecules are preferentially adsorbed onto the micropores while the mesopores remain almost empty. This is indicated by the peak in the adsorbate distribution at a pore size of 0.8 nm. Here most of the adsorbate remains confined in pores having sizes between 0.3 and 1.3 nm. Next, fig. 3.18b shows the adsorbate distribution $P/P_0=0.1$. Now, the micropores are completely

filled while the mesopores have started to fill up. Also, the adsorbate distribution closely follows the PSD. Now by defining the micropores as pore sizes below 2 nm, we can separate the total adsorbed amounts into micropore and mesopore contributions. Fig. 3.19 plots the adsorbed amounts as a function of the relative pressure. In order to highlight the low pressure regime, the x axis has been plotted in the logarithmic scale. As expected, initially the micropore contributions dominate the total adsorption and the mesopore contribution is small. As the pressure increases, the micropore adsorption reaches a plateau around $P/P_0=0.01$. Therefore, this is the point where the micropores get completely filled with adsorbate. Also at higher pressures, we see an increase in the slope of the mesopore contribution curve which indicates the onset of layered adsorption on the mesopore surface. All these effects (i.e. microporous adsorption at low pressures, monolayer-multilayer adsorption at higher pressures) are long associated with the experimental adsorption behavior of SBA-15, and are widely discussed in the literature. They can be indirectly inferred from the adsorption properties of real SBA-15. Our model not only corroborates the experimentally accepted facts, but allows us to directly visualize the micropore filling mechanism at a molecular level.

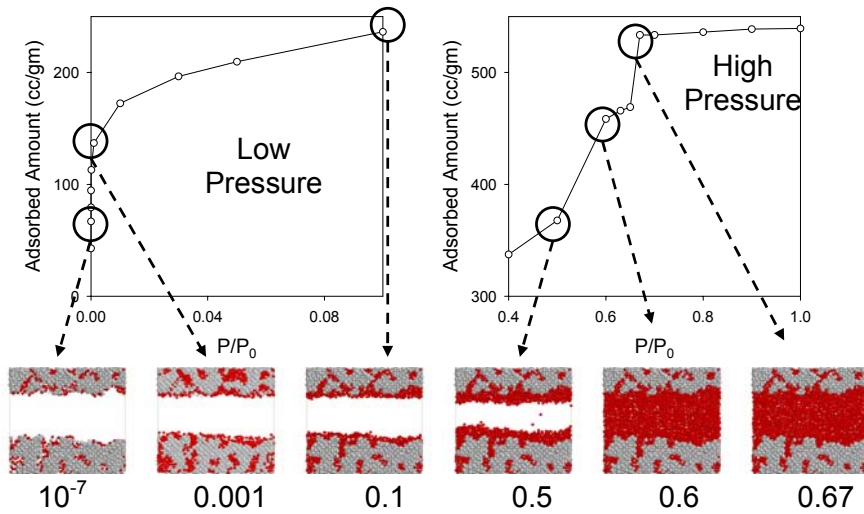


Fig. 3.17. Snapshots of simulation box with increasing pressure for model A. The values below the snapshots indicate the relative pressures. In the snapshots, grey represents silica and red Argon. The low and high pressure sections of the isotherm are shown as reference. The isotherm points corresponding to the individual snapshots are circled.

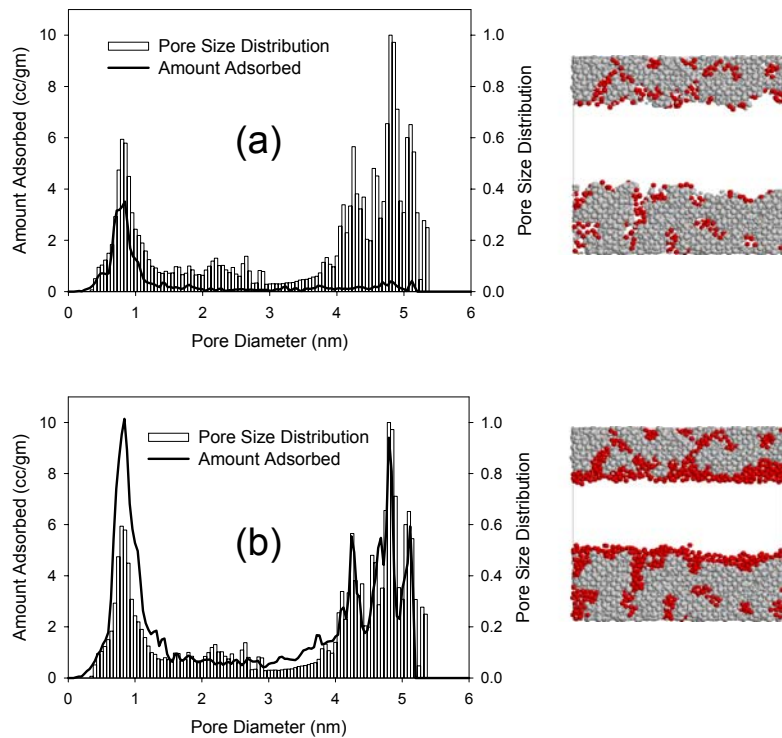


Fig. 3.18. Distribution of adsorbate with pore size for (a) $P/P_0=10^{-10}$ and (b) $P/P_0=0.1$. The dark curves represent the adsorbate distribution. The PSD is shown by the histogram. The simulation box snapshots are displayed on the right.

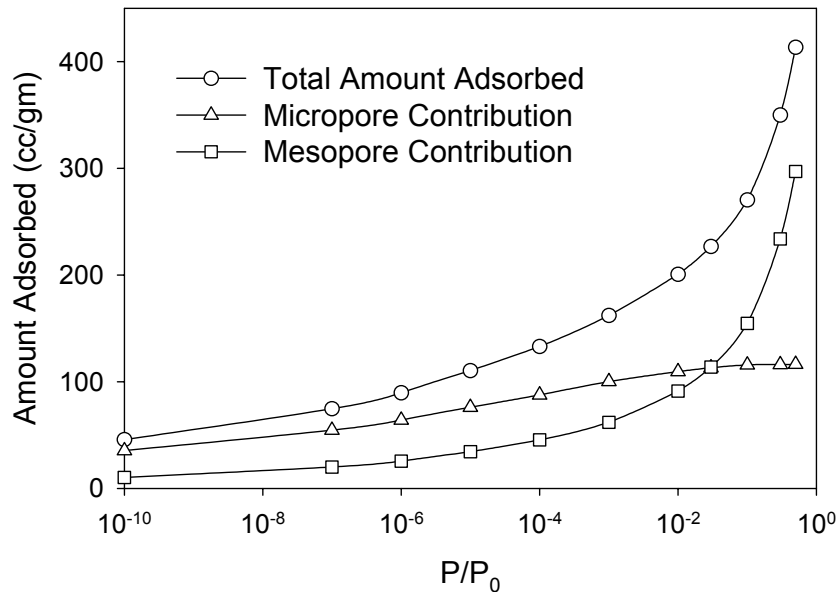


Fig. 3.19. Adsorption isotherm for model A at low pressures showing the micropore and the mesopore contributions. The x axis is plotted in logarithmic scale.

We now discuss the results for the isosteric heats of adsorption from the three models. In fig. 3.20, we report the heats of adsorption as a function of the relative loading, along with the fluid-fluid and the fluid-wall contributions. Figures 3.20a, b and c describe the heats of adsorption for the models A, B and C respectively. The x axis represents the relative loading and y axis the molar heat in kJ/mole. As expected, for all three models the heat of adsorption starts with a high value at low adsorption, then decreasing rapidly with loading and finally reaching a plateau at higher loadings. At low relative loadings, the heat of adsorption is mainly contributed by the fluid-wall interaction. As the monolayers start to build up on the pore surface, the fluid-fluid interaction becomes dominant. In all three models, the fluid-fluid interaction curves are almost identical, starting from a zero value and gradually increasing with relative loading. At 100%

loading, the fluid-fluid contributions to the isosteric heats are very similar to the molar heat of condensation for bulk Argon (6.5 KJ/Mole). The fluid-fluid contributions are therefore not influenced by the pore geometry or the surface roughness. The fluid-wall contribution for the three models are however different from one another. Model C has the lowest fluid-wall contribution followed by model B and then model A. This is understandable from the fact that model C is a regular cylinder without surface roughness, while the other two models have surface roughness. Among the models A and B, the fluid-wall contribution for A is more than that of B due to the presence of the micropores. As discussed before, the micropores function as high energy sites for adsorption and increase the attractive potential between the pore walls and the adsorbate, which is the reason for the increased fluid-wall contribution. Finally we plot the isosteric heats of the three models in fig. 3.20d along with the isosteric heat of an experimental MCM-41 sample as a reference. The MCM-41 has a pore diameter of 4.5 nm while our models have a pore diameter of 5.4 nm. We did not get any experimental data for MCM-41 with similar pore diameters. Moreover, the isosteric heat for experimental SBA-15 is not reported in the literature. We find the results for model C close to MCM-41, whereas the results for the other two models depart considerably. This may be attributed to the difference in pore diameters between the models and the experimental material. Also, MCM-41 does not have micropores, which is the reason for its lower heat of adsorption in comparison to the models.

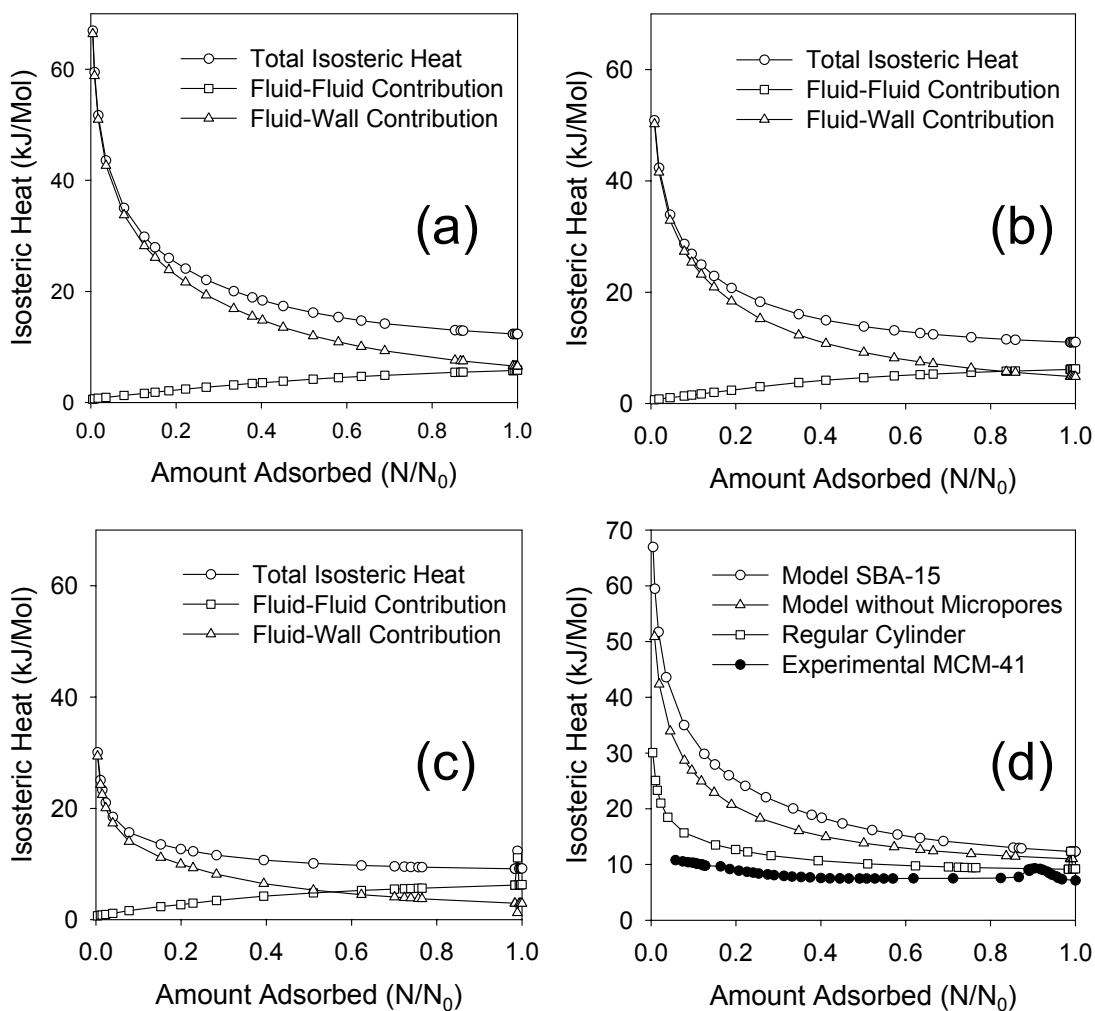


Fig. 3.20. Isosteric heats of adsorption for the different pore models. Figures (a), (b) and (c) represent the isosteric heats for models A, B and C respectively. Figure (d) compares the heats of adsorption from the three pore models and an experimental MCM-41 (Neimark *et al* [54]). -○-: Model A, -△-: Model B, -□-: Model C, -●-: Experimental MCM-41. The x axis represents the relative surface loading, while the y axis represents the heat of adsorption in kJ/mole. The mean pore diameter of the models is 5.4 nm, whereas that of the experimental MCM-41 is 4.5 nm.

3.4. Conclusion

We have developed a molecular model for a mesoporous silica material, the SBA-15 and studied its adsorption properties. In our model, we incorporated the important properties of SBA-15, namely the surface roughness and the micropores by simulating the synthesis of the material. This allowed us to present a realistic replica of the experimental SBA-15 and study the synthesis mechanism. From the mimetic simulations, we have gained knowledge regarding the phase equilibrium and self-assembly of the surfactant system. The atomistic model was characterized by computing the pore size distribution, porosity, surface area, TEM and AFM. All of the results were in qualitative agreement with the experiments and in some cases, quantitative agreements were obtained, for example the surface area and the porosity. We also studied the pore model at the molecular level by directly visualizing the micropores and calculating the RMS roughness of the mesopore surface. These results are almost impossible to obtain in experiments, but at the same time they provide useful information regarding the structure of the real material. Finally we studied the adsorption of argon inside the model pores. Using three different pore models (microporous rough pore: model A, non-microporous rough pore: model B and regular cylinder: model C), we investigated the influence of surface roughness and the micropores on the adsorption properties. Both the micropores and the surface roughness in the rough pores increased the adsorbed amounts in comparison to the regular cylindrical pore. Also due to the presence of the micropores, we observed a higher rate of adsorption at low pressures in model A compared to the other two models. The

adsorption isotherm of the microporous model was compared to the experimental isotherm from a similar sized SBA-15. For low pressures, the model was in quite good agreement with the experiment, whereas at higher pressures quantitative agreement was achieved. We analyzed the influence of the micropores in the SBA-15 model by measuring the adsorbate distribution with pore size and separating the isotherm into micropore and mesopore contributions. At low pressures, the micropore contribution was the dominant factor whereas at higher pressures, the mesopore contribution played the major role in determining the total adsorbed amounts. The isosteric heats of adsorption were computed for the three models and compared to that of an experimental MCM-41. The heat of adsorption was found to increase in the following order: MCM-41 → model C → model B → model A and was in agreement with the presence of surface roughness and micropores in the pore models. To summarize, our model showed many of the important properties of the real SBA-15 and allowed us to investigate the adsorption phenomenon at a deeper level than is possible in the experiments.

3.5. References

-
- [1] V. Chiola, J. E. Ritsko and C. D. Vanderpool, US Patent **3**, 556, 725 (1971).
 - [2] T. Yanagisawa, T. Shimizu, K. Kuroda and C. Kato, *Bull. Chem. Soc. Jpn.* **62**, 1535 (1990).
 - [3] C. T. Kresge, M. E. Leonowicz, W. J. Roth, J. C. Vartuli and J. S. Beck, *Nature* **359**, 710 (1992).
 - [4] J. S. Beck, J. C. Vartuli, W. J. Roth, M. E. Leonowicz, C. T. Kresge, K. D. Schmitt, C. T.-W. Chu, D. H. Olson, E. W. Sheppard, S. B. McCullen, J. B. Higgins and J. L. Schlenker, *J. Am. Chem. Soc.* **114**, 10834 (1992).
 - [5] V. Dufaud and M. E. Davis, *J. Am. Chem. Soc.* **125**, 9403 (2003).
 - [6] B. L. Newalkar, N. V. Choudary, P. Kumar, S. Komarneni and T. S. G. Bhat, *Chem. Mater.* **14**, 301 (2004).

-
- [7] T. Yamada, H.-S. Zhou, H. Uchida, M. Tomita, Y. Ueno, I. Honma, K. Asai and T. Katsube, *Stud. Surf. Sci. Catal.* **146**, 783 (2003).
- [8] G. Cavallaro, P. Pierro, F. S. Palumbo, F. Testa, L. Pasqua and R. Aiello, *Drug Delivery* **11**, 41 (2004).
- [9] P. V. Braun and P. Wiltzius, *Nature [London]* **402**, 603 (1999).
- [10] Z. Li and M. Jaroniec, *J. Phys. Chem. B* **108**, 824 (2004).
- [11] F. R. Siperstein and K. E. Gubbins, *Mol. Simul.* **27**, 339 (2001).
- [12] F. R. Siperstein and K. E. Gubbins, *Langmuir* **19**, 2049 (2003).
- [13] S. Bhattacharya and K. E. Gubbins, *J. Chem. Phys.* **123**, 134907 (2005).
- [14] D. Zhao, J. Feng, Q. Huo, N. Melosh, G. H. Fredrickson, B. F. Chmelka, and G. D. Stucky, *Science* **279**, 548 (1998).
- [15] R. Ryoo, C. H. Ko, M. Kruk, V. Antochshuk and M. Jaroniec, *J. Phys. Chem. B* **104**, 11465 (2000).
- [16] S. H. Joo, R. Ryoo, M. Kruk and M. Jaroniec, *J. Phys. Chem. B* **106**, 4640 (2002).
- [17] A. Galarneau, H. Cambon, F. D. Renzo, R. Ryoo, M. Choi and F. Fajula, *New J. Chem.* **27**, 73 (2003).
- [18] J. Liu, X. Zhang, Y. Han and F.-S. Xiao, *Chem. Mater.* **14**, 2536 (2002).
- [19] F. R. Hung, B. Coasne, K. E. Gubbins, F. R. Siperstein and M. Sliwinski-Bartkowiak, *Stud. Surf. Sci. Catal.* in press 2005.
- [20] B. Coasne, F. R. Hung, R. J.-M. Pellenq, F. R. Siperstein and K. E. Gubbins, *Langmuir* in press 2005.
- [21] C. G. Sonwane, C. W. Jones and P. J. Ludovice, *J. Phys. Chem. B* **109**, ASAP (2005).
- [22] B. P. Feuston and J. B. Higgins, *J. Phys. Chem.* **98**, 4459 (1994).
- [23] K. J. Edler, P. A. Raynolds, J. W. White and D. Cockson, *J. Chem. Soc., Faraday Trans.* **93**, 199 (1997).
- [24] L. A. Solovyov, S. D. Kirik, A. N. Shmakov and V. N. Romannikov, *Microporous Mesoporous Mater.* **44**, 17 (2001).
- [25] J. Puibasset, *J. Phys. Chem. B.* **109**, 480 (2005).
- [26] B. Coasne, A. Grosman, C. Ortega and R. J.-M. Pellenq, *Stud. Surf. Sci. Catal.* **144**, 35 (2002).
- [27] B. Coasne and R. J.-M. Pellenq, *J. Chem. Phys.* **88**, 2913 (2004).
- [28] B. Coasne, K. E. Gubbins and R. J.-M. Pellenq, *Part. Part. Syst. Char.* **21**, 149 (2004).
- [29] A. V. Neimark, P. I. Ravikovitch and A. Vishnyakov, *J. Phys. Condens. Matter.* **15**, 347 (2003).
- [30] B. Kuchta, L. Firllej and G. Maurin, *J. Chem. Phys.* **123**, 174711 (2005).
- [31] R. G. Larson, L. E. Scriven and H. T. Davis, *J. Chem. Phys.* **83**, 2411 (1985).
- [32] R. G. Larson, *J. Phys. II France* **6**, 1441 (1996).
- [33] A. Z. Panagiotopoulos, M. A. Floriano and S. K. Kumar, *Langmuir* **18**, 2940 (2002).
- [34] D. Frenkel and B. Smit, *Understanding Molecular Simulation*, Academic Press 2nd edition, (2002).
- [35] L. Piegl and W. Tiller, *The NURBS Book*, Springer 1995.

-
- [36] R. J.-M. Pellenq and P. E. Levitz, *Mol. Phys.* **100**, 2059 (2002).
- [37] L. D. Gelb and K. E. Gubbins, *Langmuir* **15**, 305 (1999).
- [38] S. Bhattacharya and K. E. Gubbins, *Langmuir* submitted.
- [39] M. L. Connolly, *Science* **221**, 709 (1983).
- [40] M. L. Connolly, *J. Appl. Cryst.* **16**, 548 (1983).
- [41] E. E. Underwood, Quantitative Stereology, *Addison-Wesley Publishing Company* 1970.
- [42] J. M. Cowley and A. F. Moodie, *Acta Cryst.* **10**, 609 (1957).
- [43] M. Bogana, D. Donadio, G. Benedek and L. Colombo, *Europhys. Lett.* **54**, 72 (2001).
- [44] Y. Chen and W. Huang, *Meas. Sci. Technol.* **15**, 2005 (2004).
- [45] R. J.-M. Pellenq and D. Nicholson, *J. Phys. Chem.* **98**, 13339 (1994).
- [46] D. A. Kofke, *J. Chem. Phys.* **98**, 4149 (1993).
- [47] Y. He and N. A. Seaton, *Langmuir* **21**, 8297 (2005).
- [48] D. Nicholson and N. G. Parsonage, Computer Simulation and the Statistical Mechanics of Adsorption, *Acad. Press* London, U. K. 1982.
- [49] J. S. Lettow, Y. J. Han, P. Schmidt-Winkel, P. Yang, D. Zhao, G. D. Stucky and J. Y. Ying, *Langmuir* **16**, 8291 (2000).
- [50] L. D. Gelb and K. E. Gubbins, *Langmuir* **14**, 2097 (1998).
- [51] A. Galarneau, H. Cambon, F. Di Renzo and F. Fajula, *Langmuir* **17**, 8328 (2001).
- [52] C.-M. Yang, M. Kalwei, F. Schüth and K.-J. Chao, *Appl. Catal. A* **254**, 289 (2003).
- [53] A. Galarneau, H. Cambon, F. Di Renzo, R. Ryoo, M. Choi and F. Fajula, *New J. Chem.* **27**, 73 (2003).
- [54] A. V. Neimark, P. I. Ravikovitch, M. Grün, F. Schüth and K. K. Unger, *J. Colloid. Int. Sci.* **207**, 159 (1998).

Chapter 4

Fast Method for Computing Pore Size Distributions of Model Materials

In this chapter, we report a new technique for fast computation of pore size distributions of model materials from a knowledge of the molecular coordinates*. The pore size distribution (PSD) is defined as the statistical distribution of the radius of the largest sphere that can be fitted inside a pore at a given point. Using constrained nonlinear optimization, we calculate the maximum radii of test particles at random points inside the pore cavity. The final pore size distribution is then obtained by sampling the test particle radii using Monte Carlo integration. The computation time depends on factors such as the number of atoms, the sampling resolution and the desired accuracy. However, even for large systems, PSDs with very high accuracy (>99.9%) are obtained in less than 24 hours on a 3 GHz Pentium IV processor. The technique is validated by applying it to model structures, whose pore size distributions are already known. We then apply this method to investigate the pore structures of several mesoporous silica models such as SBA-15 and Mesoporous Cellular Foams.

* Submitted to Langmuir

4.1. Introduction

Measuring pore size distribution is an important tool for characterizing porous materials. Pore size distributions are of importance in fields such as adsorption in porous media and studying microstructures of amorphous solids [1]. In adsorption related phenomena, it provides an estimate for the fraction of pore volume accessible to an adsorbed molecule. In materials modeling studies, pore size distributions of model structures can be compared to those of the real structures as a test of model accuracy. Experimentally, the pore size distribution can be calculated from adsorption measurements [2] and tomographic image analysis [1]. Measuring the pore size distributions of model structures requires statistical and geometrical analysis [3,4]. For a model structure, the pore size at a given point can be defined as the largest sphere that encompasses the given point without overlapping the neighboring wall atoms. A schematic in two dimensions is shown in fig. 4.1. The dotted circles are the various spheres that can be constructed through point P without overlapping the wall atoms. The circle in bold represents the largest one among them. Diameter D of this sphere is defined as the pore size at point P.

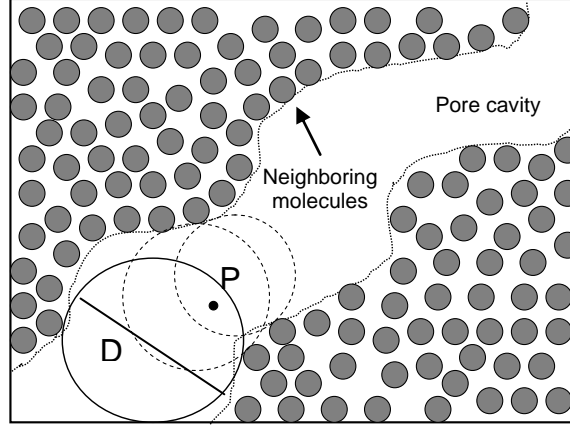


Fig. 4.1. Definition of pore size used in this work. The middle channel is the pore cavity and the grey spheres are the wall atoms. P represents the point at which the pore size is measured. D is the diameter of the circle in bold.

Thus, the pore size distribution can be estimated by dividing the model space into a finite grid and computing the largest sphere diameter D at each grid point. A cumulative histogram $H(D)$ is then constructed, where $H(D)$ represents the probability of finding a point in the model space with a pore size greater than or equal to D . The pore size distribution $P(D)$ is the negative of the differential coefficient of $H(D)$ with respect to D ; i.e.

$$P(D) = -\frac{dH(D)}{dD} \quad (4.1)$$

The only question concerning the above approach is: given a point P, how to find the largest sphere diameter D encompassing P. A suggested approach is to first create a database of spheres with the biggest possible diameter not overlapping the wall atoms, centered at each grid point. In order to find the pore size at P, one has to search through the database in the neighboring grid points of P and select the largest sphere that also overlaps P. In computing the cumulative pore size distribution $H(D)$, the histogram bin

width is equal to the distance between two adjacent grid points. The histogram bin width is inversely related to the number of grid points per unit length, also called the grid resolution. Every molecular system is associated with an optimum grid resolution which represents the tradeoff between accuracy and computational speed. Resolutions lower than the optimum lead to decreased detail in the distribution curve, whereas higher resolutions lead to enhanced accuracy along with an increase in computation time. The importance of grid resolution will be discussed in section 4.2. In computer implementations of the above method [3,4], both the memory to store the database as well as the computation time are functions of the grid resolution. As a result, the method works well at low grid resolutions, but becomes computationally expensive at higher resolution. Fig. 4.2 shows the variation of computation time with grid resolution for a mesoporous silica model.

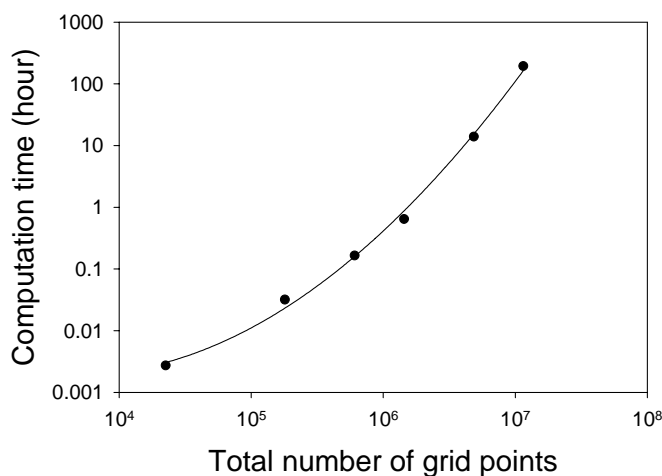


Fig. 4.2. Variation of computational time with grid size (on a 3 GHz Pentium IV processor).

In this chapter, we propose a technique for fast calculation of the pore size distributions of model materials. In order to find the largest sphere that can be fitted at a certain point inside the pore, we treat the problem as a constrained nonlinear optimization one, and solve it using one of the several nonlinear programming (NLP) algorithms proposed in the literature [5-7]. The sphere diameters are calculated at arbitrary points inside the pore and the diameters are sampled at regular intervals to generate a distribution. The method has several advantages over the previously discussed method. First of all, there is no need to create a database of sphere diameters over a finite grid, because the method searches through the continuum instead of a grid. Secondly, fast convergence is achieved through the use of efficient searching schemes instead of probing through each and every grid point. Combining these two factors, it is possible to achieve very high degree of accuracy using minimal computing time. Moreover, since the program reports the pore size distribution at regular time intervals, it is possible to observe the evolution of the distribution over time.

The method relies on a constrained optimization approach in solving a geometrical problem. Linear and nonlinear programming models have been successfully used in solving related problems in computational geometry [8,9]. Welzl [8] proposed an algorithm for computing the smallest enclosing disk of a finite set of points in a plane. Gärtner and Schönherr [9] extended Welzl's algorithm to 3 dimensions for computing ellipsoids and spheres. Our problem is different from the one presented in [8] and [9], because instead of the smallest enclosing sphere of a set of points, we are interested in the

largest sphere enclosed by a set of points. For the first problem, Welzl employed a Linear Programming technique combined with an iterative approach. In our case, we have applied nonlinear programming models. The problem presented here can be solved using any suitable NLP scheme, which can handle discontinuous objective functions. We have used the SOLVOPT program written by Kuntsevich and Kappel [7], because it is well suited for optimizing non-smooth objective functions. More information about this program can be found at their website [7].

4.2. The Problem

Fig. 4.3 depicts the 2-D representation of the problem. Imagine a set of n spherical atoms in space with radius r . For simplicity, all the atoms here are assumed to have the same radius, but this treatment can easily be extended to cover atoms with variable radii. Let $P(P_x, P_y, P_z)$ be the point where the pore size is to be measured. Let $C(C_x, C_y, C_z)$ be the center of the biggest sphere enclosed by the n atoms which also overlaps P . Let R be the radius of the enclosed sphere, s_i the distance between C and the center of the i^{th} atom, d_P the distance between C and P . Clearly, R is a function of C . Therefore we can write,

$$R(C) = \text{MIN}(s_i) - r, \quad i=1 \dots n \quad (4.2)$$

In order to find the biggest possible sphere radius, we need to find the location of C for which R is the maximum. However, there is an additional criterion that, P should be inside the sphere, i.e.

$$d_P \leq R(C) \quad (4.3)$$

Therefore, we set up the nonlinear optimization problem as:

$$\begin{aligned} & \text{MAXIMIZE } \{ R(C) = \text{MIN}(s_i) - r \} \text{ subject to} \\ & \text{constraint: } d_p - R(C) \leq 0 \end{aligned} \quad (4.4)$$

The above problem may be solved using any appropriate NLP routine. In our case, we have used the SOLVOPT [7] program for reasons explained in the previous section.

The basic algorithm is described in fig. 4.4. We select random points P and compute the pore sizes at these points. After each sampling interval, we update the cumulative histogram $H(D)$ and calculate the PSD as the negative of the derivative of $H(D)$. The pore size distribution of the accessible volume also depends on the size of the test particle. Ref. 4 gives the definition of accessible volume. Pores which are smaller than the diameter of the test particle are not accessible by the test particle. In our calculations, we have used a test particle diameter of 3.409 Å, which corresponds to the Lennard-Jones σ parameter for argon-argon interaction. The average error err is calculated as the mean of the relative errors between the old and the new probability values. Therefore,

$$err = \left\langle \frac{PSD_{new}(D) - PSD_{old}(D)}{PSD_{new}(D)} \right\rangle \quad (4.5)$$

where $PSD(D)$ is the probability for the pore size D. The average error is an estimate of how different a new PSD is compared to the old one. The computation may be terminated when the value of err , averaged over several Monte Carlo blocks, falls below the specified error limit TOL. We have used an error limit of 0.01% for all our computations.

The efficiency of this technique depends on the selection of an appropriate grid resolution. The grid resolution should be large enough not to smooth out the minute details / undulations in the distribution curve. On the other hand, setting the resolution too high will increase the computation time without adding extra information to the distribution. As a rule of thumb, the grid resolution should be smaller than the minimum bandwidth of all the peaks and undulations in the PSD. Initially a very low resolution can be used to get a quick idea about the nature of the distribution curve (e.g. the mean and standard deviation). Then the resolution can be increased in small steps until a small change in grid resolution does not lead to any significant change in the shape of the distribution.

The accuracy of the PSD is highly dependent on the efficiency of the random number generator used in selecting the random points. The values generated by the random number generator must be uniform; i.e. they should have the same probability everywhere within the set. If the generator is biased, i.e. the probability for a certain range of numbers is higher than the rest, the generated PSD will be inaccurate. We have used one of the random number generators from ref. 6, which is found to have a uniform probability distribution.

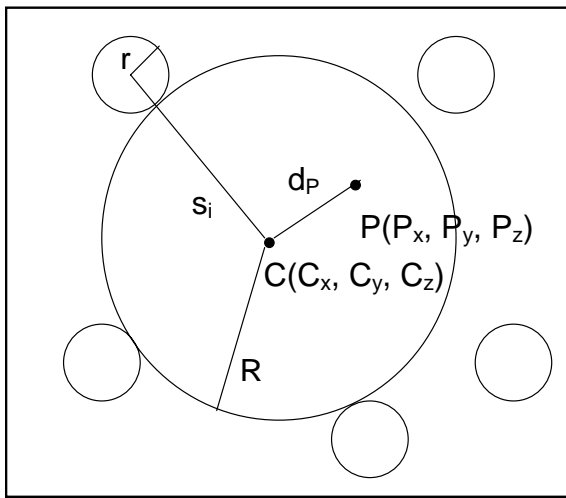


Fig. 4.3. Largest sphere enclosed by n atoms; r : radius of the enclosing atoms; R : radius of the largest enclosed sphere; C : center of the enclosed sphere; P : the point at which, the pore size is measured; s_i : distance from C to the center of the i^{th} atom; d_P : distance between C and P .

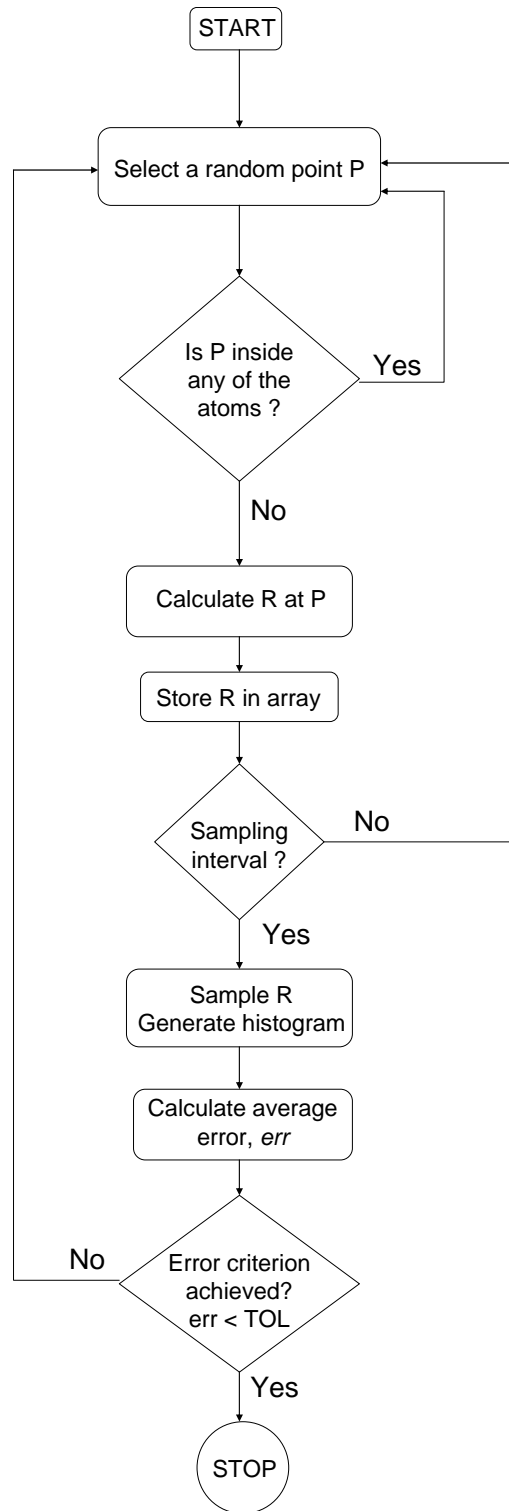


Fig. 4.4. Flow chart for PSD calculation

4.3. Results and Discussion

This section is divided into several subsections depending on the topic of interest. First, we show that our method samples the correct pore size distribution by applying in a model, where the PSD is known in advance. Then we discuss the PSDs of several model structures generated by mimetic simulations. Finally, we analyze the performance of our model and compare it with one of the existing methods of calculating pore size distributions. All probability distributions are normalized to unity for clarity. The graphs show both the cumulative histogram H and the PSD obtained by differentiating H .

4.3.1. Test Model

Usually, the validity of a numerical method can be tested by applying it to cases where the final result is already known from other sources. In order to verify our method, we generated a model structure having box dimensions $120 \times 120 \times 120 \text{ \AA}$, with spherical pores placed at random positions within the box. The diameters of these pores were randomly selected from a Gaussian distribution with a mean of 20 \AA and a standard deviation of 3.33 \AA . The snapshot of this structure is shown in fig. 4.5a. We can predict that the pore size distribution of this structure should be very similar to the Gaussian distribution used in generating the pore diameters. Fig. 4.5b shows the cumulative and differential pore size distributions of the model structure as generated by our method. The Gaussian distribution is also shown for comparison. We find that the calculated pore size

distribution follows the predicted PSD (Gaussian distribution). However, the calculated distribution shows a bias towards the higher values of pore diameter with a mean at 20.51 Å and a standard deviation of 5.42 Å. The bias arises due to the fact that, while generating the pore cavities, some of the smaller pores were partly or completely engulfed by the larger pores. The reason for the increased standard deviation is that the smaller pores which were partly engulfed by the larger pores appeared as blemishes on the surface of the larger pores contributing to the very small pore diameters. For a system with completely unconnected pores, these differences should be negligible. Additionally, if the system is infinitely large, the calculated PSD should exactly match the Gaussian distribution.

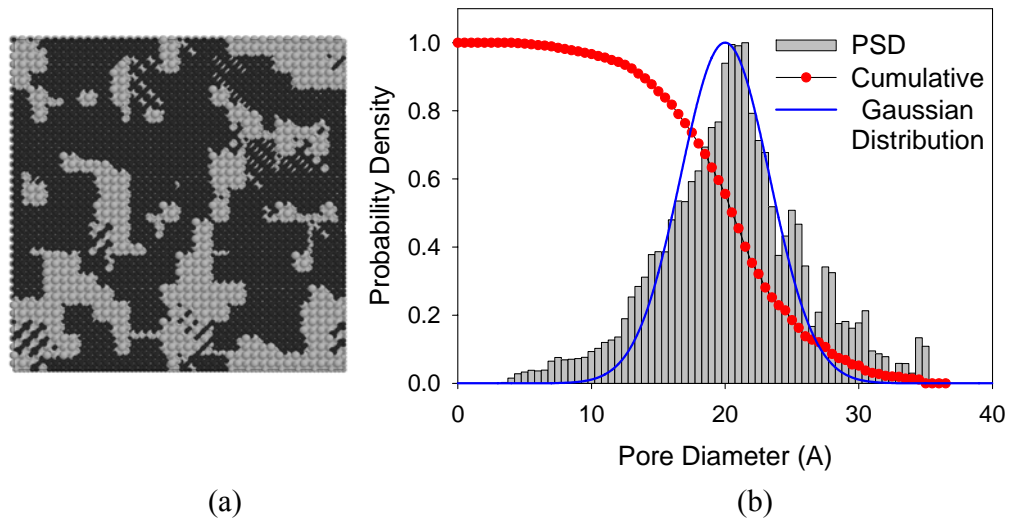


Fig. 4.5. The test model structure. (a) Cross sectional view. Dark regions represent the void spaces and the light regions represent the pore walls; (b) Pore size distribution

4.3.2. Mimetic Models

In this section, we will discuss the pore size distributions of some of the model structures developed as part of our ongoing project [10-13]. All of these are templated mesoporous silica models created by mimicking the synthesis process using Lattice Monte Carlo simulations [14-15]. In practice, these materials are synthesized by polymerizing silica around a surfactant-silica mesophase and then extracting the silica structures from the surfactant solution. First, we will describe the PSD of the model SBA-15 [16] structure. The pores of the SBA-15 are cylindrical in shape and ordered hexagonally. In practice, the pore size of SBA-15 varies from 50 to 300 Å. Fig. 4.6a shows the simulation box snapshot of the model SBA-15 in the direction of the cylinder axis and fig. 4.6b shows the pore size distribution. The pore size of the model SBA-15 varies between 35 Å and 62 Å with a mean at 51.65 Å. The PSD shows a single peak at 54 Å, which corresponds to the cylindrical mesopore diameter. On either side of this peak, the distribution decays to zero. However, on the left side, towards the smaller pore sizes, the decay is more gradual compared to the right side. The reason is the following. In a lattice model, the individual lattice points are spaced approximately 35 Å apart. To construct the pore wall from such a configuration, we decorated the lattice points with silica spheres having a radius of 17.5 Å. The space where the adjacent spheres touched each other contributed to the smaller pore diameters.

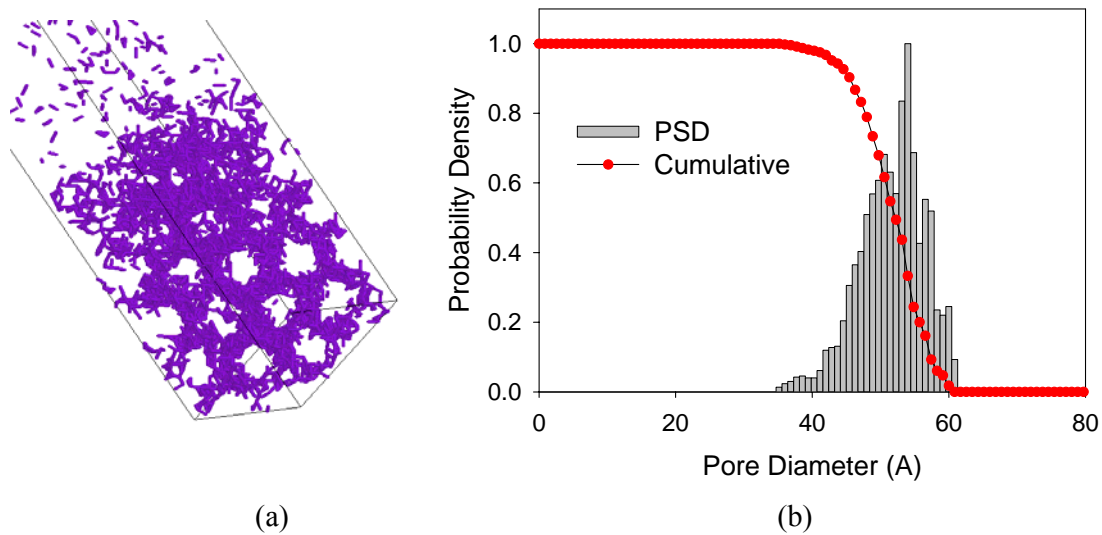


Fig. 4.6. The SBA-15 structure. (a) Simulation box snapshot; (b) Pore size distribution

Next consider the pore structure of the mesostructured cellular foams (MCF). Ref. 17 gives the details of MCF synthesis. The pore structure of MCF is made up of spherical cells with diameter between 200 and 500 Å, which are connected to each other via windows of smaller diameters (~ 100 Å). Fig. 4.7a shows a schematic of the MCF structure and fig. 4.7b shows the simulation box snapshot. Fig. 4.7c shows the pore size distributions for the model MCF structure. Due to the presence of the larger cells and the relatively smaller windows, the pore size distribution of MCF shows two peaks, one at 150 Å (windows) and the other at 450 Å (cell). This is in sharp contrast with the PSD for SBA-15, which consists of only one peak. In the pore size distribution of the model MCF, the windows have a smaller size variation compared to the cells. The MCF cells are produced during synthesis by polymerizing silica around closely packed surfactant micelles and the points where these spheres touch each other form the windows. While

the exact mechanism of window formation is not fully understood, it is clear that the size distribution of these cells is closely related to the cluster size distribution of the surfactant micelles. Following the same logic, the window size distribution is related to the packing behavior of the micelles. A detailed analysis of the cluster size and the packing behavior involves the thermodynamic properties of the simulation system and is beyond the scope of the present discussion.

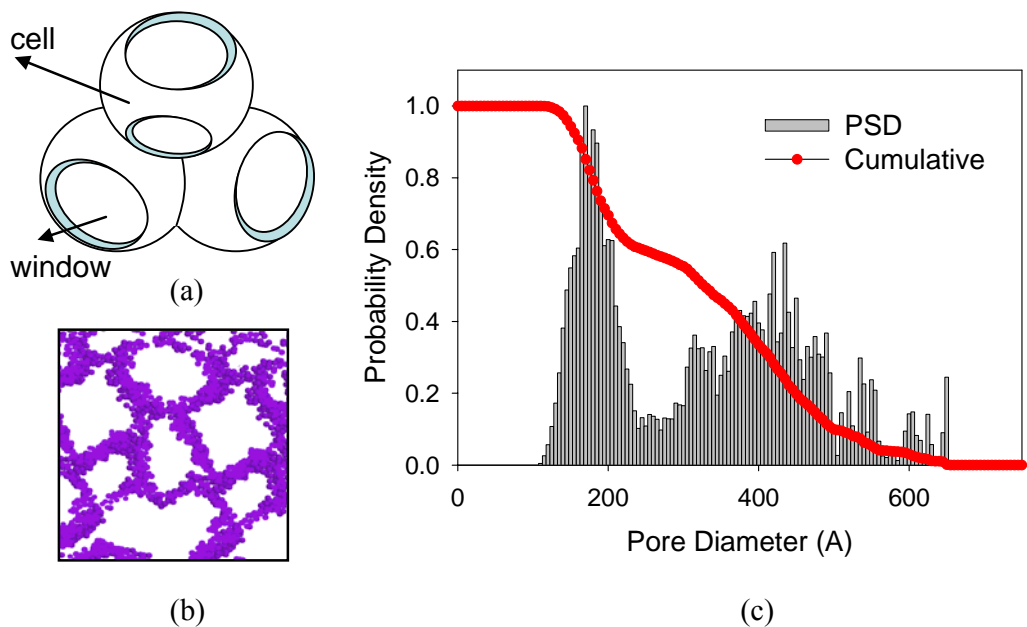


Fig. 4.7. The MCF structure. (a) Schematic of MCF pores; (b) Simulation box snapshot; (c) Pore size distribution.

So far, we have discussed the pore structures of lattice models. We now describe a fully atomistic structure derived from the lattice models. Based on previous works by Pellenq and Levitz [18] and Coasne et al [19,20], we have developed an atomistic model of SBA-15 from the lattice structure shown in fig. 4.6. The details of the atomistic modeling can be found in ref. 10. Fig. 4.8a shows the schematic of an atomistic SBA-15 pore assembly.

The results shown here are averaged over five atomistic SBA-15 pores. The hollow cylinders are the mesopores and the dark wirings are the micropores connecting the mesopores. Both the micropores, which are less than 10 Å in diameter, and the main mesopores constitute the porosity of SBA-15. Fig 4.8b presents a snapshot of the model SBA-15 structure. The silicon and the oxygen atoms are bonded in an amorphous tetrahedral network with the hydrogen atoms saturating the dangling bonds at the pore surface. In fig. 4.8b, the locations of the mesopores and the micropores are marked by the white color coded hydrogen atoms. Fig. 4.8c shows the pore size distribution. The PSD consists of one small peak at lower pore diameters (around 15 Å) and a larger peak at 54 Å. The smaller peak at 15 Å represents the micropore diameters and the larger peak at higher pore sizes represents the mesopores.

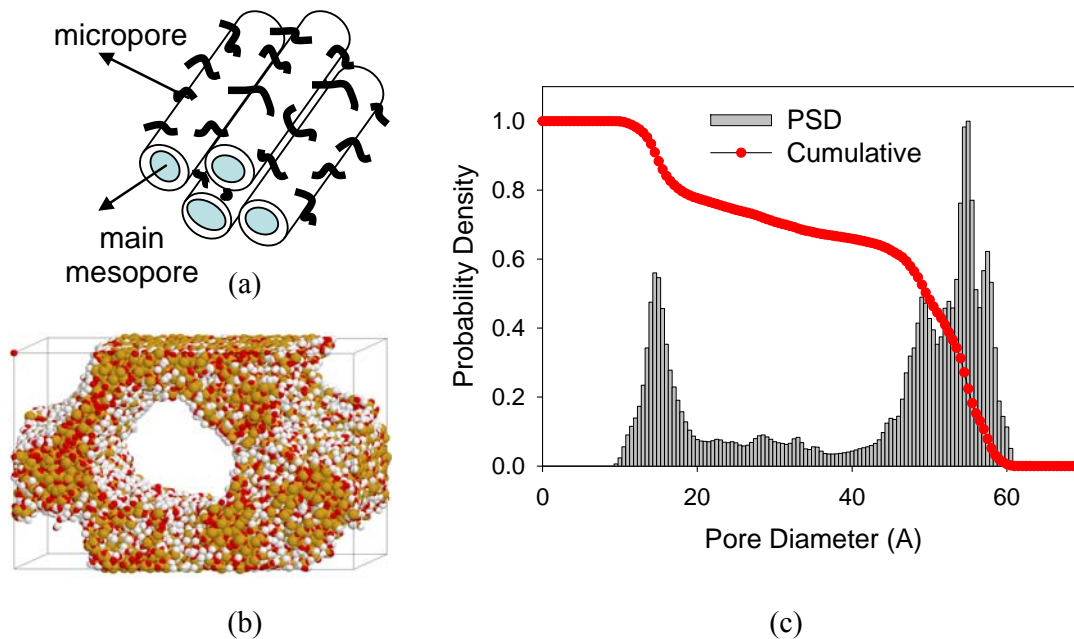


Fig. 4.8. The atomistic SBA-15 structure. (a) Schematic showing the meso and the micropores; (b) Simulation box snapshot. yellow- silicon, red- oxygen, white- hydrogen; (c) Pore size distribution

4.3.3. Performance Analysis

We will now analyze the performance of the procedure and compare it with one of the existing methods discussed in section 1. All the computations were performed on 3 GHz, Pentium IV processors with 1 GB RAM running RedHat Linux 7.3. The code for calculating the PSDs was compiled using GNU C++. Fig. 4.9 shows the variation of average error with computation time for the lattice model of SBA-15. The definition of average error is given in section 4.2. The error is initially high, but decreases rapidly with time. The rate of decrease of error is also high towards the beginning of the computations, but slows down as time progresses. The figure also shows the evolution of the pore size distribution with computation time. Initially, only a small part of the PSD is sampled, which is shown in the snapshot at $t=0.00633$ hrs. As expected, regions with higher probabilities are sampled first, for example the mesopore peak at $D=54$ Å. With time, more points are sampled and the distribution slowly evolves into its final form.

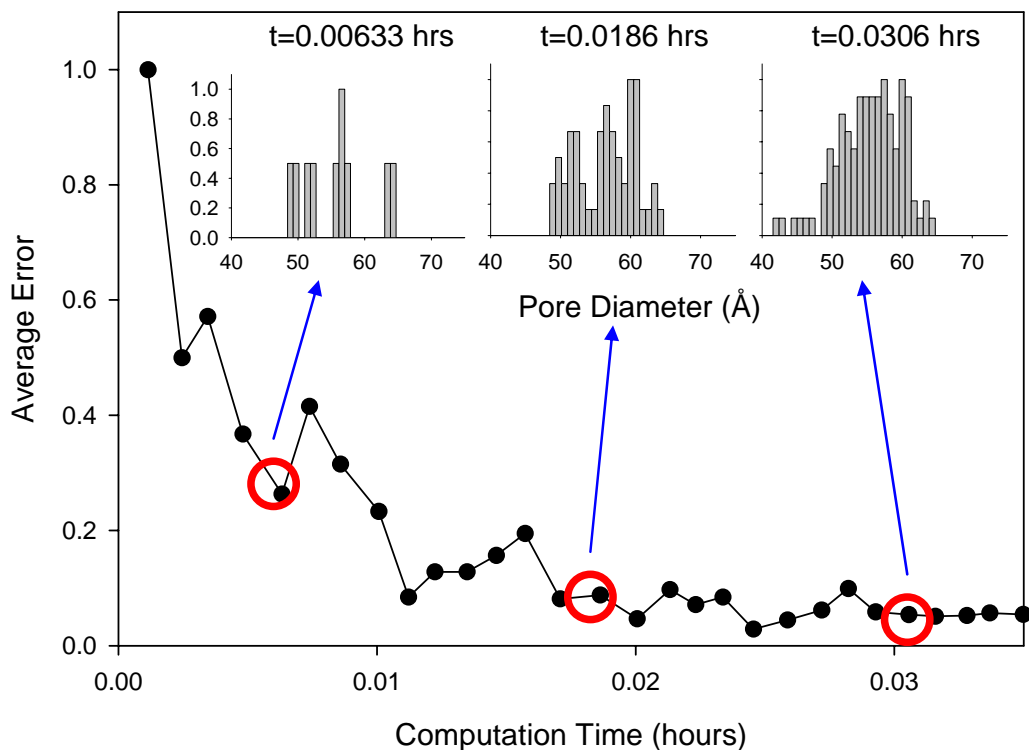


Fig. 4.9. Average error with computation time. The insets depict the evolution of the PSD over time. Each snapshot corresponds to a different time interval.

Fig. 4.10 shows the computation time as a function of grid resolution, both for our method and the existing method discussed in section 1. Resolution is defined as the number of points per unit Angstrom, where the pore size distributions are computed. For example, if the resolution is 20, then the PSD is calculated at 0 Å, 0.05 Å, 0.1 Å etc. Both the axes are plotted in the logarithmic scale. For the existing method, the computation time shows a non-linear variation with grid resolution. A quadratic regression curve fitted to the data-points (shown in Fig. 4.10) indicates that the increase in computation time with grid resolution is initially small for very low resolutions. However, the curve

becomes increasingly steeper at higher resolutions, when a small increase in the grid resolution can lead to a very large increase in the computation time. Therefore, it is computationally expensive to calculate PSDs at high resolutions using the existing method. In contrast, for our method, the logarithmic variation of computation time with grid resolution shows a linear trend. The computation time t (hours) has the functional form $t = a x^b$, where a and b are constants and x denotes the resolution (points / unit length). The values of a and b can be obtained through regression analysis and are shown in fig. 10. The value of exponent b determines the relative increase in computational time with increase in resolution. For our method, the value of b is 0.615676. Comparing the two trends (one for the existing method, the other one for our method), it is observed that at high resolution, the computation times for our method are orders of magnitude less compared to the existing scheme. However, for very low resolutions (<2.63), the existing method is found to be faster compared to the current method. For our method, the computational cost does not increase significantly with grid resolution, as it did for the existing method. Moreover, the method proposed here is ideal for implementing in a parallel architecture, where multiple processors can compute more number of points in less time and speed up the computation.

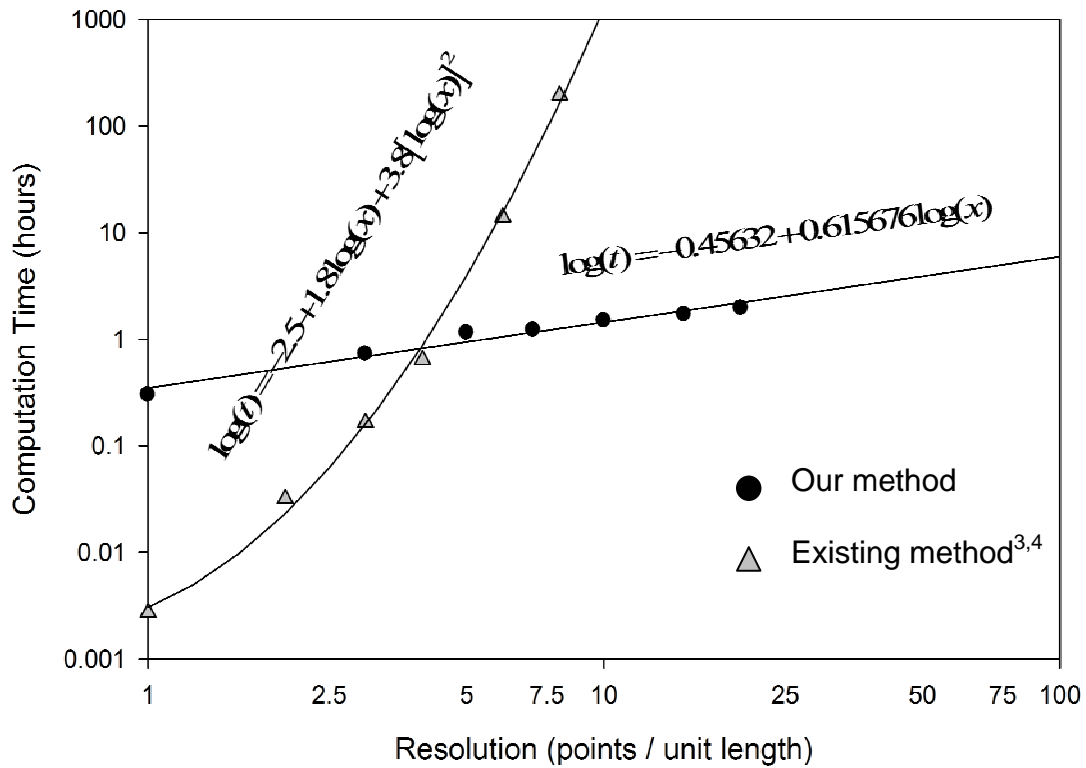


Fig. 4.10. Comparison between our method and the existing method discussed in section 1. Resolution is defined as number of points per unit length, where the pore sizes are calculated.

4.4. Conclusion

We have presented a computationally efficient way of computing the pore size distributions of model structures from a knowledge of the molecular coordinates. The method uses constrained nonlinear programming techniques for calculating pore sizes at different points within the porous structure. A large number of these points are then sampled to obtain the final pore size distribution. The accuracy of this method has been verified by calculating the pore size distribution of a model structure, whose PSD is

known in advance. We then demonstrate the practical applicability of the discussed technique by using it to calculate the pore size distributions of several porous models. Finally, performance evaluation shows that, the computation time is proportional to x^b , where x is the resolution and b is a constant. Comparing with established techniques, we show that the present method is significantly faster, particularly for high resolutions.

4.5. References

-
- [1] C. R. Appoloni, C. P. Fernandes, M. D. de Mello Innocentini and A. Macedo, A. *Mat. Res.* **7**, 557 (2004).
- [2] (a) J. Rouquerol, F. Rouquerol and K. S. W. Sing, *Adsorption by Powders and Porous Solids: Principles, Methodology and Applications*, Feb. 1999, Acad Press. (b) F. Schuth F, K. S. W. Sing and J. Weitkamp, *Handbook of Porous Solids, Vol. 1* 2002, Wiley.
- [3] L. D. Gelb and K. E. Gubbins *Langmuir* **15**, 305 (1999).
- [4] K. T. Thomson and K. E. Gubbins, *Langmuir* **16**, 5761 (2000).
- [5] J. T. Betts, *ACM T Math Software* **6**, 432 (1980).
- [6] W. H. Press, W. T. Vetterling, S. A. Teukolsky and B. P. Flannery, *Numerical Recipes in C++ 2nd Edition*, Cambridge Univ. Press. 2002.
- [7] F. Kappel and A. V. Kuntsevich, *Comput. Optim. Appl.* **15**, 193 (2000).
<http://www.uni-graz.at/imawww/kuntsevich/solvopt/>.
- [8] E. Welzl, *Notes Comput. Sc.* **555**, 359 (1991).
- [9] B. Gärtner and S. Schönherr, *Inform. Process. Lett.* **68**, 33 (1998).
- [10] S. Bhattacharya, B. Coasne, F. R. Hung and K. E. Gubbins, *Stud. Surf. Sci. Catal.* in press.
- [11] S. Bhattacharya and K. E. Gubbins, *J. Chem. Phys.* **123**, 134907 (2005).
- [12] F. R. Siperstein and K. E. Gubbins, *Mol. Simul.* **27**, 339 (2001).
- [13] F. R. Siperstein and K. E. Gubbins, *Langmuir* **19**, 2049 (2003).
- [14] R. G. Larson, L. E. Scriven and H. T. Davis, *J. Chem. Phys.* **83**, 2411 (1985).
- [15] R. G. Larson, *J. Phys. II France* **6**, 1441 (1996).
- [16] D. Zhao, J. Feng, Q. Huo, N. Melosh, G. H. Fredrickson, B. F. Chmelka and G. D. Stucky, *Science* **279**, 548 (1998).
- [17] J. S. Lettow, Y. J. Han, P. Schmidt-Winkel, P. Yang, D. Zhao, G. D. Stucky and J. Y. Ying, *Langmuir* **16**, 8291 (2000).
- [18] R. J.-M. Pellenq and P. E. Levitz, *Mol. Phys.* **100**, 2059 (2002).
- [19] B. Coasne and R. J.-M. Pellenq, *J. Chem. Phys.* **121**, 3767 (2004).
- [20] B. Coasne, K. E. Gubbins and R. J.-M. Pellenq, *Part. Part. Syst. Character.* **21**, 149 (2004).

Chapter 5

Conclusions and Future Directions

We have used molecular simulations to develop realistic molecular models for surfactant templated mesoporous materials and applied these models to study the adsorption of rare gases inside the model pores. Three different TMMs are considered: Mesoporous Cellular Foams (MCF) [1] with interconnected spherical pores, MCM-41 [2,3] with hexagonally ordered cylindrical pores and SBA-15 [4] with microporous pore walls. In preparing the models, molecular simulations are used to mimic the synthesis of the materials and the structures evolve following similar mechanisms as in the experiments. Therefore the resulting structures are free from any underlying assumptions or artificial parameters. The physical properties of the model structures such as the PSD, surface area, TEM images etc. are in agreement with the experimental results. Finally, the adsorption properties of the models have been studied using GCMC simulations with special emphasis on the effects of the micropores and surface roughness. The adsorption isotherm for the model SBA-15 is in semi-quantitative agreement with the experimental SBA-15 isotherm.

In Chapter 2, we presented the results for the modeling of MCF. In order to develop a mesoscale model of the MCF structure, we have mimicked the synthesis using Lattice Monte Carlo simulations. Besides preparing the MCF model, we explore the phase diagrams of several model triblock surfactants. First we compare the aqueous phase

diagrams of two triblock surfactants, $H_2T_7H_2$ and $H_3T_5H_3$, which have the same overall chain length but different head to tail ratios. In aqueous solution, the surfactant $H_2T_7H_2$ shows an affinity towards the lamellar phase whereas the surfactant $H_3T_5H_3$ shows an affinity towards cylindrical structures. Therefore we infer that the lower head to tail ratios lead to the formation of structures where the head-tail interface has low curvatures, such as the lamellar phase. On the other hand, high head to tail ratios favor the formation of structures with high interfacial curvatures, such as the cylinder. This result can be explained from the chain packing mechanisms [5] and is in qualitative agreement with the experiments [6]. Next we investigate the ternary surfactant-oil-water and surfactant-silica-water phase diagrams of the model triblock surfactant $H_3T_5H_3$. Depending on the component concentrations, different structures are observed at different regions of the phase diagrams, e.g. spherical micelles at low surfactant concentrations, cylindrical micelles at medium surfactant concentrations towards the water side and lamellar phase at high surfactant concentrations. The results from the surfactant-oil-water phase diagram are in qualitative agreement with the experiments, whereas those from the surfactant-silica-water phase diagram are in agreement with the previous simulation studies [7]. Then we add oil to the surfactant-silica-water system and study the influence of oil on the ordered structures. In the simulations, the sequence of ordered structures with increasing oil concentration is as follows: cylinder \rightarrow lamellae \rightarrow mesocells. Experimentally [1] the sequence observed is: cylinder \rightarrow undulating cylinder \rightarrow mesocell. Therefore, the simulations are in qualitative agreement with the experiments at low and high oil concentrations, but differ from each other at medium oil concentrations. Finally we

calculate the pore size distributions of the model structures. The PSDs of the cylindrical structures show a single peak, whereas those of the mesocellular structures show two peaks (window and cell) and are qualitatively similar to the experimental observations.

In chapter 3, we discuss the molecular modeling of MCM-41 and SBA-15. The mesoscale models of the MCM-41 and SBA-15 are prepared from the cylindrical structures obtained in conjunction with the MCF simulations. We characterize the model structures using a variety of techniques such as the pore size distribution, surface area, TEM and AFM imaging. The pore size distribution of the model SBA-15 qualitatively agrees with the experiments, while the internal surface area and the porosity are in quantitative agreement with the experimental results [8]. Next we study the variation of internal surface area of the model SBA-15 with adsorbate radius. Due to the contribution from the micropores, the high surface area is observed for low adsorbate radii (r_p). The surface area then decreases with increasing adsorbate radius finally going to zero for $r_p >$ mesopore radius. Comparing with the surface areas from the non-microporous model, we have estimated the relative contribution of the micropores to the total surface area. For Argon adsorption, the micropores contribute 50% of the total surface area, although they constitute only 30% of the total porosity. Since adsorption is a surface driven phenomenon, this result emphasizes the influence of the micropores on the adsorption properties of SBA-15. We then calculate the high resolution TEM (HRTEM) images of the model structures. The TEM for the model SBA-15 shows a lower electron density in the pore walls compared to that in the non-microporous model. This difference in

electron density can be directly related to the presence of the micropores in the SBA-15 model. The model TEMs are qualitatively comparable to the experimental TEMs [9] and both contain similar micropore patterns in the pore walls. We also show how the contrast in the model TEMs are affected by the amount of defocus and emphasize the need for proper focusing in obtaining the experimental TEMs. The mesopore surfaces of the models can be directly visualized from the simulated AFMs. As a result of the micropores, the RMS roughness of the SBA-15 model is higher compared to that of the non-microporous model.

The simulations of Argon adsorption inside the model pores are performed using GCMC simulations. We have compared the adsorption properties of three different pore models with the same pore diameter, the SBA-15 pore, the non-microporous (MCM-41) pore and a regular cylindrical pore. The adsorption isotherms from all three models are then compared to the isotherm from an experimental SBA-15 with similar pore size. Due to the presence of the micropores, the SBA-15 model adsorbs higher amounts of adsorbate in comparison to both the non-microporous and the regular cylindrical models. Among the non-microporous and regular cylindrical models, the former is found to adsorb more Argon compared to the latter due to surface roughness. The experimental SBA-15 isotherm is closer to the SBA-15 model compared to the other two models. The range of pressures for the capillary condensation is similar for all the three models as well as the experiments. However, the adsorbed amounts are different among the three models. Therefore we conclude that the micropores and surface roughness lead to an increase in

the adsorbed amounts. On the other hand, it is known from the experiments that the capillary condensation pressure is mainly dependent on the mesopore diameter, temperature and the adsorbate size. However, a small decrease in the capillary condensation pressure is observed in the non-microporous model in comparison to the SBA-15 model, which may be due to the undulations in the pore surface of the former. We have also calculated the isosteric heats of adsorption of the three models as functions of the relative loading. The model isosteric heat curves follow the trends observed experimentally for cylindrical pores, gradually decreasing with relative loading and reaching a plateau at high adsorbate concentrations. We have also compared among the different pore models the contributions from the fluid-fluid and the fluid-wall interactions. For the three models, the fluid-fluid contributions are similar. However the fluid-wall contribution increases in the following order: regular cylinder \rightarrow non-microporous pore \rightarrow model SBA-15. Therefore, the surface roughness and the micropores lead to an increase in the isosteric heat of adsorption. This increase is mainly due to the fluid-wall contribution whereas the fluid-fluid contribution is almost unaffected by the surface roughness or the microporosity. The heat of adsorption for the model SBA-15 is also found to be higher compared to that of an experimental MCM-41 [10] due to the micropores present in the former.

We have also developed new methods for characterizing the model structures. Chapter 4 describes a fast method for computing the pore size distributions of model materials. Based on nonlinear optimization, the method has been found to be many orders of

magnitude faster compared to the existing technique [11]. In both the existing as well as the new methods, PSD computation proceeds by dividing the model space into a finite grid. Increasing the grid resolution (finer grid) results in improved accuracies at the same time increasing the computational time. We have compared between the computation times for the two methods as functions of the grid resolution. For the existing method, the computation time increases nonlinearly with grid resolution, so that a small increase in grid resolution leads to a large increase in computation time. The existing method is therefore inefficient in handling large systems, which require high grid resolutions. In comparison, the new method shows a linear increase in computation time with grid resolution, which implies that this technique is more efficient compared to the old method, especially for the larger systems. Finally, applying this technique we have discussed the pore size distributions of several model structures.

The current work can be extended to cover several future research areas. One of the important applications of pore models is in studying the various confinement phenomena such as adsorption, phase transitions, diffusion and chemical reactions. Simulations of adsorption inside the model pores can yield valuable information regarding the adsorption mechanisms. In chapter 3, we studied the adsorption of Argon inside the model SBA-15 at 77K. This work may now be extended to cover other adsorbates such as Nitrogen [12], Krypton [13], Xenon as well as hydrocarbons and water [14]. Also the simulations may be carried out at several different temperatures in order to study the effect of temperature on adsorption properties. Confinement also affects the phases

transitions in the adsorbed substances and new phases may be formed that are not observed in the bulk. For example, Hung *et al* [15] studied the freezing of Krypton inside model MCM-41. Similar studies may be performed using the model SBA-15. Diffusion of various adsorbates in these materials is known to be very sensitive to pore morphology and topology, including wall roughness. Diffusion studies in these materials would be particularly interesting, and a strong test of realism of these structures.

There is yet another interesting area where the pore models from the current work may be applied. TMMs are synthesized by polymerizing silica around surfactant micellar templates. However the TMMs themselves can be used as templates for synthesizing new materials such as the mesoporous carbons [16-22]. The electrical properties of carbon make these materials useful in manufacturing electrodes, while the nanopores allow the adsorption of chemical substances inside them. In the last four years, numerous publications have appeared in the literature proposing several synthesis routes for fabricating the mesoporous carbons. In general the synthesis starts from a silica based mesoporous material which acts as the template. The pores of the template are then impregnated by carbonaceous precursors (e.g. sucrose, furfuryl alcohol, phenolic resins) either from the liquid phase or by chemical vapor deposition. Then the impregnated precursor is carbonized by heating at high temperatures when the amorphous carbon structures are formed on the silica pore walls. Finally the silica is removed by dissolving in HF leaving behind the carbonaceous residue. The material formed in this way represents an inverse replica of the original template having a much larger surface area

and porosity. SBA-15 acts as a very good template because it contains both mesopores as well as the micropores. In the resulting carbon materials, the inverse replicas of the micropores act as supports for the mesopores leading to highly stabilized structures. As part of the current work, we have developed models for SBA-15 which may be used to simulate the synthesis of the mesoporous carbons. A possible route is to simulate the adsorption of carbonaceous compounds inside the model SBA-15 using GCMC simulations. In the experimental synthesis, the adsorption usually takes place in the liquid phase. However assuming a gas phase adsorption is also a reasonable approximation in creating a realistic wall structure. Moreover, the synthesis of mesoporous carbons has been reported to be performed using gas phase adsorption [22]. The silica and other non-carbon substances are then removed and the remaining carbon atoms rearranged to form graphitic networks. In this step, the bond formation and deletion may be simulated following a Monte Carlo scheme. Recently, a similar Monte Carlo technique was used in developing models for disordered porous carbons [23]. Finally, the structure is relaxed using energy minimization techniques.

References

-
- [1] J. S. Lettow, Y. J. Han, P. Schmidt-Winkel, P. Yang, D. Zhao, G. D. Stucky and J. Y. Ying, *Langmuir* **16**, 8291 (2000).
 - [2] C. T. Kresge, W. J. Roth, J. C. Vartuli, J. S. Beck and M. E. Leonowicz, *Nature* **359**, 710 (1992).
 - [3] J. S. Beck, J. C. Vartuli, W. J. Roth, M. E. Leonowicz, C. T. Kresge, K. D. Schmitt, C. T.-W. Chu, D. H. Olsen, E. W. Sheppard, S. B. McCullen, J. B. Higgins, J. L. Schlenker, *J. Am. Chem. Soc.* **114**, 835 (1992).
 - [4] D. Zhao, J. Feng, Q. Huo, N. Melosh, G. H. Fredrickson, B. F. Chmelka and G. D. Stucky, *Science* **279**, 548 (1998).

-
- [5] J. Israelachvili, *Intermolecular and Surface Forces*, Academic Press 2nd edition.
- [6] G. Wanka and W. Ulbricht, *Macromolecules* **27**, 4145 (1994).
- [7] F. R. Siperstein and K. E. Gubbins, *Langmuir* **19**, 2049 (2003).
- [8] R. Ryoo, C. H. Ko, M. Kruk, V. Antochshuk and M. J. Jaroniec, *Phys. Chem. B* **104**, 11465 (2000).
- [9] J. Liu, X. Zhang, Y. Han and F.-S. Xiao, *Chem. Mater.* **14**, 2536 (2002).
- [10] A. V. Neimark, P. I. Ravikovitch, M. Grün, F. Schüth and K. K. Unger *J. Colloid. Int. Sci.* **207**, 159 (1998).
- [11] L. D. Gelb and K. E. Gubbins *Langmuir* **15**, 305 (1999).
- [12] A. Galarneau, H. Cambon, F. D. Renzo, R. Ryoo, M. Choi and F. Fajula, *New J. Chem.* **27**, 73 (2003).
- [13] K. Morishige, K. Kawano and T. Hayashigi, *J. Phys. Chem. B.* **104**, 10298 (2000).
- [14] E. V. Bavel, V. Meynen, P. Cool, K. Lebeau and E. F. Vansant, *Langmuir* **21**, 2447 (2005).
- [15] F. R. Hung, Ph. D. Thesis, N C State University.
- [16] R. Ryoo, S. H. Joo and M. Kruk and M. Jaroniec, *Adv. Mater.* **13**, 677 (2001).
- [17] H. Darmstadt, C. Roy, S. Kaliaguine, T.-W. Kim and R. Ryoo, *Chem. Mater.* **15**, 3300 (2003).
- [18] M. Choi and R. Ryoo, *Nature* **2**, 473 (2003).
- [19] S. H. Joo, S. Jun and R. Ryoo, *Micro. Meso. Mat.* **44**, 153 (2001).
- [20] J. Parmentier, S. Saadhallah, M. Reda, P. Gibot, M. Roux, L. Vidal, C. Vix-Guterl and J. Patarin, *J. Phys. Chem. Solids* **65**, 139 (2004).
- [21] C. Yu, J. Fan, B. Tian, D. Zhao and G. D. Stucky, *Adv. Mater.* **14**, 1742 (2002).
- [22] A. V. Fuertes and D. M. Nevskaja, *J. Mater. Chem.* **13**, 1843 (2003).
- [23] A. Kumar, R. F. Lobo and N. J. Wagner, *Carbon* **43**, 3099 (2005).